Electrochemical pressure impedance spectroscopy for studying mass transport processes in polymer electrolyte membrane fuel cells: A model-based analysis

Zur Erlangung des akademischen Grades eines
DOKTORS DER INGENIEURWISSENSCHAFTEN (DR.-ING.)

von der KIT-Fakultät für Chemieingenieurwesen und Verfahrenstechnik des
Karlsruher Instituts für Technologie (KIT)
genehmigte

DISSERTATION

von
M.Sc. Lutz Schiffer
aus Duisburg

Tag der mündlichen Prüfung: 05.05.2023

Erstgutachter: Prof. Dr. Wolfgang G. Bessler
Zweitgutachter: Prof. Dr. Francois Lapicque

Kurzfassung

Die elektrochemische Druckimpedanzspektroskopie (EPIS) ist ein neues Verfahren, das aktuell zur Untersuchung von Stofftransportprozessen in Polymerelektrolytbrennstoffzellen (PEMFC) erforscht wird. Es basiert auf der spektralen Analyse der Zellspannungsantwort auf eine harmonische Anregung des Gasdrucks. Verschiedene Experimente mit Einzelzell-Brennstoffzellen haben gezeigt, dass die Spektren grundsätzlich Informationen in dem für Stofftransportprozesse typischen Frequenzbereich enthalten und sensitiv auf geänderte Betriebsbedingungen und strukturelle Veränderung der Brennstoffzelle reagieren. Um weiter von diesen Merkmalen der Spektren zu profitieren, ist es notwendig, ihre Ursache zu identifizieren, was bis jetzt noch nicht erreicht wurde. Das Ziel der vorliegenden Dissertation ist es, Kausalzusammenhänge zwischen internen Prozessen und ihren zugehörigen Merkmalen im EPIS-Spektrum herzustellen.

Hierzu wird ein modellgestützter Ansatz gewählt, der den Vorteil hat, interne Zustände analysieren zu können, die experimentell schwer zugänglich sind. Das verwendete PEMFC-Modell ist ein pseudo-2D-Modell, das den Transport entlang des Gaskanals und den Transport durch die Membran-Elektroden-Einheit (MEA) abbildet und miteinander verknüpft. Eine Neuheit gegenüber anderen in der Literatur verwendeten Modellen ist die Berücksichtigung des Gasvolumens in dem der Brennstoffzelle vorgeschalteten Gasbefeuchter, welche sich als essenziell für die Reproduktion der EPIS-Experimente erweist. Das Brennstoffzellenmodell wird mithilfe der experimentellen Daten des französischen Projektpartner parametrisiert, welcher EPIS-Experimente mit einer 100 cm^2 Einzelzell-Brennstoffzelle durchgeführt hat. Die besagten Daten wurden als Interpretationsgrundlage in der vorliegenden Arbeit verwendet.

Die EPIS-Simulationen weisen eine gute Übereinstimmung mit den Experimenten für Stromstärken ≤ 0.4 A cm^{-2} auf, wo sie eine weitere Analyse der EPIS-Merkmale ermöglichen. Bei der niedrigsten Anregungsfrequenz von 1 mHz nähert sich die dynamische Zellspannungsantwort dem statischen Verhalten an. In dem übrigen Frequenzbereich zwischen 1 mHz – 100 Hz korreliert die Oszillation der Zellspannung stark mit der des Sauerstoffpartialdrucks, während der Einfluss des Wasserdrucks nur im niederfrequenten Bereich sichtbar ist.

Die zwei auffälligsten EPIS-Merkmale, die Verstärkung der Zellspannungsoszillationen und die Zunahme der Phasenverschiebung mit der Frequenz, können über den Sauerstoffpartialdruck auf die Oszillation des Eingangsmassenstroms zurückgeführt werden. Das Phänomen des oszillierenden Eingangsmassenstroms wird durch die Druckänderung der Gasphase im Befeuchter erzeugt und verstärkt sich mit zunehmender Frequenz. Diese wichtige Erkenntnis ermöglicht die Interpretation von experimentell beobachteten Veränderungen des EPIS-Signals für geänderte Betriebsbedingungen und strukturelle Veränderungen der Brennstoffzelle.

Die separate Simulation der zeitabhängigen Brennstoffzellenprozesse anhand von Modellreduktionen zeigt ihren individuellen Einfluss auf das EPIS-Signal. Der träge Prozess der Wasseraufnahme der Membran ist nur in dem Frequenzbereich unterhalb von 0.1 Hz sichtbar, während die Ladung und Entladung der elektrischen Doppelladungsschicht erst oberhalb von 1 Hz sichtbar wird. Der Gastransport durch die Gasdiffusionsschicht ist sogar erst oberhalb von 100 Hz sichtbar. Ohne die Berücksichtigung des Befeuchters ist der Gastransport durch den Gaskanal oberhalb von 1 Hz sichtbar. Mit Berücksichtigung des Befeuchters hingegen ist der Prozess des Gastransportes durch den Gaskanal im gesamten Frequenzbereich zu sehen. Die starke Ähnlichkeit des Spektrums unter Berücksichtigung des Befeuchters mit dem Spektrum des vollständigen Brennstoffzellenmodells zeigt den dominanten Einfluss des Befeuchters auf das EPIS-Signal.

Eine vielversprechende Beobachtung ist die Änderung des Amplitudenverhältnis zwischen der Oszillation der Zellspannung und des Sauerstoffpartialdrucks in Abhängigkeit der Sauerstoffkonzentration in der Katalysatorschicht. In dem Frequenzbereich, in dem der Einfluss des Sauerstoffpartialdrucks auf die Zellspannungsoszillation dominiert, z.B. bei 1 Hz, könnte die Amplitude der Zellspannungsoszillation indirekt zur Messung der Sauerstoffkonzentration in der Katalysatorschicht genutzt werden.

Abstract

Electrochemical pressure impedance spectroscopy (EPIS) has received the attention of researchers as a method to study mass transport processes in polymer electrolyte membrane fuel cells (PEMFC). It is based on analyzing the cell voltage response to a harmonic excitation of the gas phase pressure in the frequency domain. Several experiments with a single-cell fuel cell have shown that the spectra contain information in the frequency range typical for mass transport processes and are sensitive to specific operating conditions and structural fuel cell parameters. To further benefit from the observed features, it is essential to identify why they occur, which to date has not yet been accomplished. The aim of the present work, therefore, is to identify causal links between internal processes and the corresponding EPIS features.

To this end, the study follows a model-based approach, which allows the analysis of internal states that are not experimentally accessible. The PEMFC model is a pseudo-2D model, which connects the mass transport along the gas channel with the mass transport through the membrane electrode assembly. A modeling novelty is the consideration of the gas volume inside the humidifier upstream the fuel cell inlet, which proves to be crucial for the reproduction of EPIS. The PEMFC model is parametrized to a 100 cm^2 single cell of the French project partner, who provided the experimental EPIS results reproduced and interpreted in the present study.

The simulated EPIS results show a good agreement with the experiments at current densities ≤ 0.4 A cm^{-2}, where they allow a further analysis of the observed features. At the lowest excitation frequency of 1 mHz, the dynamic cell voltage response approaches the static pressure-voltage response. In the simulated frequency range between 1 mHz – 100 Hz, the cell voltage oscillation is found to strongly correlate with the partial pressure oscillation of oxygen, whereas the influence of the water pressure is limited to the low frequency region.

The two prominent EPIS features, namely the strong increase of the cell voltage oscillation and the increase of phase shift with frequency, can be traced back via the oxygen pressure to the oscillation of the inlet flow rate. The phenomenon of the oscillating inlet flow rate is a consequence of the pressure change of the gas phase inside the humidifier and increases with frequency. This important finding enables the interpretation of experimentally observed EPIS trends for a variation of operational and structural fuel cell parameters by tracing them back to the influence of the oscillating inlet flow rate.

The separate simulation of the time-dependent processes of the PEMFC model through model reduction shows their individual influence on EPIS. The sluggish process of the water uptake by the membrane is visible below 0.1 Hz, while the charge and discharge of the double layer becomes visible above 1 Hz. The gas transport through the gas diffusion layer is only visible above 100 Hz. The simulation of the gas transport through the gas channel

without consideration of the humidifier becomes visible above 1 Hz. With consideration of the humidifier the gas transport through the gas channel is visible throughout the frequency range. The strong similarity of the spectra considering the humidifier with the spectra of the full model setup shows the dominant influence of the humidifier on EPIS.
A promising observation is the change in the amplitude relationship between the cell voltage and the oxygen partial pressure oscillation as a function of the oxygen concentration in the catalyst layer. At a frequency where the influence of oxygen pressure on the cell voltage is dominant, for example at 1 Hz, the amplitude of the cell voltage oscillation could be used to indirectly measure the oxygen concentration in the catalyst layer.

Table of contents

List of abbreviations i
List of symbols i
List of subscripts and superscripts iv
1 Introduction 1
2 State of the art 5
2.1 Pioneering works of EPIS 5
2.2 EPIS in PEMFCs 6
2.2.1 Excitation with loudspeaker by Engebretsen et al. 7
2.2.2 Excitation with pressure controller by Shirsath et al. 9
2.2.3 Excitation with pressure controller by Zhang et al. 16
2.3 CFRA in PEMFCs by Sorrentino et al. 19
2.4 Continuum modeling of PEMFCs 23
2.5 Research gaps 26
3 Methodology 28
3.1 PEMFC model 28
3.1.1 Modeling domain 28
3.1.2 Governing equations 30
3.1.3 Parametrization 39
3.1.4 Numerical implementation 44
3.2 Impedance spectroscopy simulations 45
3.2.1 EIS 45
3.2.2 EPIS 46
3.3 Analytical pressure derivative of the cell voltage 47
3.3.1 Cathode equilibrium potential 48
3.3.2 Cathode overpotential 48
3.3.3 Electrolyte potential 49
4 Model performance 51
4.1 I-V Curve 51

4.2 EIS 52
4.3 Pressure loss along the gas channel 56
4.4 Water transfer through the PEM 56
4.5 Static pressure-voltage response 58
5 EPIS (1): Analysis of pressure dynamics 62
5.1 Pressure response 62
5.1.1 Total pressure 65
5.1.2 Molar fraction 70
5.1.3 Partial pressure 77
5.2 Voltage response 81
5.3 Conclusion 84
6 EPIS (2): Influence of parameters 86
6.1 Operational parameters 86
6.1.1 Current density 86
6.1.2 Stoichiometry 88
6.1.3 Gas composition 91
6.2 Structural parameters 95
6.2.1 Gas channel length 95
6.2.2 Gas humidifier volume 98
6.3 Conclusion 100
7 EPIS (3): Influence of time-dependent processes 102
7.1 DL charge and discharge 103
7.2 Water uptake of the PEM 105
7.3 Gas transport in the GDL 107
7.4 Gas transport in the gas channel 108
7.4.1 Without humidifier 109
7.4.2 With humidifier 110
7.5 Conclusion 112
8 Summary and outlook 113
References 116
Acknowledgements 124

List of abbreviations

BV	Butler-Volmer
CFRA	Concentration frequency response analysis
CL	Catalyst layer
DL	Double layer
DENIS	Detailed electrochemistry and numerical impedance simulations
EIS	Electrochemical impedance spectroscopy
EPIS	Electrochemical pressure impedance spectroscopy
FRA	Frequency response analysis
GDL	Gas diffusion layer
HOR	Hydrogen oxidation reaction
IPCC	Intergovernmental Panel on Climate Change
MEA	Membrane electrode assembly
MPL	Microporous layer
OCV	Open-circuit voltage
ORR	Oxygen reduction reaction
PEM	Polymer electrolyte membrane
PEMFC	Polymer electrolyte membrane fuel cell

List of symbols

Latin

A_{ch}	Cross-sectional area of gas channel, m^2
A_{FC}	Active fuel cell area, m^2
a	Water activity, –
$a_{\mathrm{a,d}}$	Water absorption/desorption rate coefficient, $\mathrm{m\ s^{-1}}$
C	Humidifier volume acting as a capacitor, $\mathrm{l\ bar^{-1}}$
$C_{\mathrm{DL}}^{\mathrm{V}}$	Volume-specific double-layer capacitance, $\mathrm{F\ m^{-3}}$
c_i	Concentration of species i, $\mathrm{mol\ m^{-3}}$
D_{ij}	Binary diffusion coefficient of species i and j, $\mathrm{m^2\ s^{-1}}$
D_{ij}^{eff}	Effective binary diffusion coefficient of species i and j, $\mathrm{m^2\ s^{-1}}$
D_i^{K}	Knudsen diffusion coefficient of species i, $\mathrm{m^2\ s^{-1}}$
D_λ	Diffusion coefficient of water in electrolyte, $\mathrm{m^2\ s^{-1}}$
d_{particle}	Diameter of particle in porous electrode, m
EW	Equivalent weight of the dry electrolyte, $\mathrm{kg\ mol^{-1}}$

F	Faraday's constant, 96 485 C mol^{-1}
f	Frequency, s^{-1}
f	Volume fraction of water in electrolyte, –
f_1, f_2	Friction factors of gas channel, –
ΔH	Reaction enthalpy, J mol^{-1}
I	Absolute electric current, A
i_{cell}	Cell current density, A m^{-2}
i_{elyt}	Ionic current density, A m^{-2}
$i_{\mathrm{F}}^{\mathrm{V}}$	Volume-specific Faradaic current density, A m^{-3}
i_{0}^{V}	Volume-specific exchange current density, A m^{-3}
$i_{\mathrm{DL}}^{\mathrm{V}}$	Volume-specific current density due to DL charge/discharge, A m^{-3}
J^{conv}	Convective molar flux, mol m^{-2} s^{-1}
J_i^{diff}	Diffusive molar flux of species i, mol m^{-2} s^{-1}
$J_{\lambda}^{\mathrm{diff}}$	Diffusive molar flux of water in the electrolyte, mol m^{-2} s^{-1}
$J_{\lambda}^{\mathrm{drag}}$	Molar flux of water dragged in the electrolyte, mol m^{-2} s^{-1}
j_i^{diff}	Diffusive mass flux of species i, kg m^{-2} s^{-1}
$k_{\mathrm{a,d}}$	Water absorption/desorption rate constant, m s^{-1}
L_{CH}	Length of the gas channel, m
L_{CL}	Thickness of the catalyst layers, m
M_i	Molar mass of species i, kg mol^{-1}
$\dot{m}$	Mass flow rate, kg s^{-1}
n_{CH}	Number of gas channels, –
$\dot{n}$	Molar flow rate, mol s^{-1}
p	(Total) pressure, Pa
P_{ch}	Perimeter of gas channel, m
p_i	Partial pressure of species i, Pa
$p_{\mathrm{H_2O}}^{\mathrm{sat}}$	Saturation pressure of water, Pa
p_{N}	Standard pressure, 101 325 Pa
p_{ref}	Reference pressure, in Nernst equation 101 325 Pa
$\hat{p}$	Pressure amplitude, Pa, bar
Q	Electric charge, C
Q	Volumetric flow rate, l s^{-1}
r	Pressure drop along gas channel per flow rate, bar s l^{-1}
R	Ideal gas constant, 8.314 J mol^{-1} K^{-1}
R_{contact}	Specific contact resistance, Ω m^2
r_{pore}	Pore radius of porous electrode, m
ΔS	Reaction entropy, J mol^{-1} K^{-1}

$\dot{S}_i$	Molar source term of species i, mol m^{-3} s^{-1}
$\dot{S}_\lambda$	Molar source term of water in electrolyte, mol m^{-3} s^{-1}
$\dot{s}_i$	Mass source term of species i, kg m^{-3} s^{-1}
T	Time period, s
T	Temperature, K
T_N	Standard temperature, 273.15 K
T_ref	Reference temperature, in kinetic expressions 353.15 K
t	Time, s
V_cell	Cell voltage, V
V_hum	Gas phase volume of humidifier, m^3
V_m	Specific volume per sulfonic acid sides of electrolyte, m^3 mol^{-1}
v	Flow velocity, m s^{-1}
w_CH	Width of gas channel, m
w_rib	Width of gas channel rib, m
x_i	Molar fraction of species i, –
$Z_{p/p}$	Transfer function between oscillation of inlet pressure and outlet pressure, –
$Z_{p(\mathrm{avg})/p}$	Transfer function between oscillation of average total pressure along catalyst layer or gas channel and outlet pressure, –
$Z_{p(i,\mathrm{avg})/p}$	Transfer function between oscillation of average partial pressure of species i along catalyst layer or gas channel and outlet pressure, –
$Z_{Q/p}$	Transfer function between oscillation of inlet flow rate and outlet pressure, l Pa^{-1} s^{-1}
$Z_{V/i}$	Transfer function between oscillation of cell voltage and cell current density, Ω m^2
$Z_{V/p}$	Transfer function between oscillation of cell voltage and outlet pressure, V Pa^{-1}
$Z_{x(i,\mathrm{avg})/p}$	Transfer function between oscillation of average molar fraction of species i along catalyst layer or gas channel and outlet pressure, Pa^{-1}

Greek

α	Water transfer coefficient, –
$\alpha_\mathrm{A}, \alpha_\mathrm{C}$	Anodic and cathodic transfer coefficient of half-cell reactions, –
ε	Porosity of porous electrode, –
ϵ_elyt	Volume fraction of electrolyte, –
η	Overpotential, V
κ	Permeability of porous electrode, m^2
λ	Water content of electrolyte, –

λ^{eq}	Water content of electrolyte at equilibrium, –
λ_i	Stoichiometric factor of species i, –
μ	Viscosity of gas, kg m^{-1} s^{-1}
ξ	Electro-osmotic drag coefficient, –
ρ_i	Density of species i, kg m^{-3}
$\rho_{\mathrm{elyt,dry}}$	Density of dry electrolyte, kg m^{-3}
σ_{elyt}	Proton conductivity of electrolyte, S m^{-1}
τ	Tortuosity of porous electrode, –
τ_{w}	Wall shear stress, Pa
ϕ	Electric potential, V
$\phi(Z)$	Phase shift of transfer function Z, °
$\Delta\phi$	Galvani potential, V
$\Delta\phi^{\mathrm{eq}}$	Galvani potential at equilibrium, V
φ	Relative humidity, –
ω	Angular frequency, rad s^{-1}

List of subscripts and superscripts

a	Absorption
A	Anode
ACH	Anode gas channel
ACL	Anode catalyst layer
AGDL	Anode gas diffusion layer
avg	Average
C	Cathode
CCH	Cathode gas channel
CCL	Cathode catalyst layer
CGDL	Cathode gas diffusion layer
CH	Gas channel
CL	Catalyst layer
d	Desorption
DL	Double layer
elde	Electrode
elyt	Electrolyte
feed	Gas feed
FC	Fuel cell
GDL	Gas diffusion layer

hum	Humidifier
in	Inlet
out	Outlet
PEM	Polymer electrolyte membrane (layer)
Pt	Platinum

1 Introduction

According to the Intergovernmental Panel on Climate Change (IPCC) [1], human activities, in particular the emission of greenhouse gases, are responsible for the global warming of 1.0 °C above pre-industrial levels, with an ongoing increase of 0.2 °C per decade. The increase in global temperature is expected to have negative effects on the climate system such as sea level rise, local hot extremes, drought, and heavy precipitation, among others. To avert the loss of livelihood it is essential to prevent or at least limit the trend of global warming. In 2015, at the international climate conference COP 21 in Paris, 195 countries signed the Paris Agreement [2], a treaty with the goal of "Holding the increase in the global average temperature to well below 2 °C above pre-industrial levels and pursuing efforts to limit the temperature increase to 1.5 °C above pre-industrial levels". On a five-year cycle, the participating countries have to present plans on their reduction of greenhouse gas emissions to fulfill the defined goal. Based on the modeling of possible scenarios, the IPCC estimates that limiting warming to 1.5 °C requires global net zero carbon dioxide emissions by 2050, accompanied by substantial reductions of other greenhouse gases, in particular methane [3].

As a possible pathway to fulfill these goals, the IPCC proposes a rapid decarbonization of the energy supply, which implies a strong upscaling of renewable energy technologies [3]. The renewable energy sources comprise biomass, hydro, solar, wind, and geothermal power. Although renewable energy sources are sufficiently available to fully substitute the current use of fossil fuels, there are drawbacks which limit their realization. One problem is restricted temporal availability, due to the volatile nature of sun and wind in particular. The second problem is limited spatial accessibility, due to the immobility of energy conversion units or their low power density. These drawbacks can be overcome, however, by storing renewable energy chemically and converting it back into electricity in times of low availability or with a mobile energy converter with a sufficiently high power density. The chemical storage of renewable energy can be realized with the electrolysis of water and storage of the hydrogen produced. Subsequently, the hydrogen can be converted into electricity and heat by the use of fuel cells in times of low availability of sun and wind, or in mobile applications. Even though one has to pay a price in terms of additional energy conversion losses, the intermediate step of temporary storage of renewable energies in hydrogen enables the complete substitution of fossil energies by renewable energies.

Depending on the application, different types of fuel cells may be suitable for the reconversion of the chemically stored energy into electricity and heat. They differ mainly in the type of fuel and the temperature level, among other things. One of the most established type of fuel cells is the polymer electrolyte membrane fuel cell (PEMFC) [4]. It is operated on moderate temperatures between 30 °C and 100 °C [5] and requires relatively pure

hydrogen. It can be used in mobile applications, such as trains, ships, aircrafts and other motorized vehicles, or in stationary applications, such as combined heat and power systems.

The PEMFC is a complex system due to the diversity of mass transport processes in combination with electrochemical reactions. To optimize the fuel cell performance, whether in terms of structural development or prevention of faulty operation [6], it is crucial to make the subprocesses measurable to determine their contribution to the overall performance. The overall performance of the fuel cell can be rated relatively simply by analyzing the relationship between the cell current and voltage. However, quantifying the contributing subprocesses to the overall performance is more difficult. One way to tackle this problem and further characterize the fuel cell is via frequency response analysis (FRA). In FRA the system's response to a harmonic excitation is measured and then analyzed in the frequency domain, by means of the transfer function between cause and effect. Depending on the characteristic time scales of relevant subprocesses, the spectrum of the transfer function shows features in the respective frequency range. In the Bode representation the features of the transfer function are visible as a change of the magnitude, which is the amplitude ratio between the system's response and its excitation and visible as a change of the phase shift. If the time constants of the subprocesses do not overlap, subprocesses can be measured separately. A widely-used technique of FRA is electrochemical impedance spectroscopy (EIS) [7], which analyzes the relationship between cell current and voltage in the frequency domain. Typically, the electrochemical impedance spectra reveal two features, one at higher frequencies, related to the charge transfer processes [8–12], and one at lower frequencies, whose origin remains debatable [13].

To obtain additional information in the low-frequency region, which may improve characterization of mass transport processes, another FRA technique has started to gain interest, called electrochemical pressure impedance spectroscopy (EPIS). It is based on analyzing the relationship between the gas pressure and the cell voltage. Recent experimental studies have been conducted on EPIS in a single-cell PEMFC by applying a sinusoidal pressure excitation of the gas phase at the cathode channel outlet and measuring the resulting cell voltage response: Shirsath et al. [14–17] and Zhang et al. [18] both used a pressure controller for the pressure excitation and recorded spectra in the frequency range below 1 Hz; Engebretsen et al. [19] used a loudspeaker for the pressure excitation and recorded spectra in the frequency range below 100 Hz. Another approach of pressure excitation was applied by Sorrentino et al. [20–22], who excited the partial pressure of species at the cathode gas inlet by periodically changing specific reactant feeds. The spectra of the so-called concentration frequency response analysis (CFRA) were recorded for frequencies below 1 Hz.

The EPIS and CFRA spectra contain features, visible as changes in magnitude and phase of their respective transfer functions, in the analyzed frequency range. Principally, this shows the ability of these methods to characterize specific processes of the fuel cell with a corresponding time dependence. The authors relate the features of the measured spectra to mass transport processes, such as diffusion [16,17,21,22], convective transport along the channel [16,17,21,22] and sorption of water into the electrolyte [21,22]. However, in case of diffusion and convective transport, it is not explained how these processes would directly affect the transfer function in terms of magnitude and phase shift. Therefore, the origin of typically observed EPIS features is yet to be found. By changing numerous operational as well as structural parameters of the fuel cell, the authors were able to show the sensitivity of EPIS towards these parameters. To further understand and exploit these dependencies, it is crucial to identify their origin.

To increase the understanding of the obtained spectra and evaluate the potential of EPIS to characterize specific processes, further interpretation of the spectra is required. Therefore, the goal of the present work is to find out the origin of experimentally observed EPIS features and the reason for their sensitivity towards specific parameters. Modeling and simulation can be a powerful tool for this purpose. It makes it possible to change the fuel cell setup without being restricted to experimental limitations and to observe internal states which are difficult to access experimentally. So far, there has been no simulative study of EPIS in a PEMFC using a physical model that can reproduce the experimentally observed spectra. In the present dissertation, a physical model of a PEMFC is used which couples the dimension in through-plane direction of the membrane electrode assembly (MEA) and the dimension along the gas channel. The dimension along the gas channel is crucial to reproduce the EPIS spectra, as the pressure response has been observed to change with the excitation frequency along the gas channel [14,17,18].This results in a so-called pseudo-2D model or 1+1D model, which has been used in the literature in other contexts before [23–27]. A model novelty is the modeling of the gas volume in the humidifier upstream the fuel cell, which has a strong influence on the pressure dynamics and the inlet flow rate during pressure excitation [14,17,28]. The present work was carried out within the framework of a Franco-German partner project with the working group of Prof. Francois Lapicque at the Reactions and Chemical Engineering Laboratory, CNRS-University of Lorraine. Therefore, the model is parametrized to their experimental setup, which is described in Shirsath et al. [14–17].

The dissertation is structured as follows. After this introductive chapter, the state of the art of the characterization method EPIS is presented in Chapter 2. In Chapter 3, the PEMFC model and the simulative approach of EPIS is described. Additionally, the pressure derivative of the cell voltage is derived. Subsequently, in Chapter 4, the ability of the PEMFC model to reproduce other experiments than EPIS is shown. The EPIS study itself is divided

into three parts. In Chapter 5 the yet unknown origin of typical experimentally observed EPIS features is worked out by relating them to the dynamic pressure response of the fuel cell. Subsequently, the influence of operational and structural parameters on the EPIS results are simulated and compared to experiments in Chapter 6. In the third part of the EPIS study, in Chapter 7, the influence of the time-dependent fuel cell processes on the EPIS results are simulated separately by appropriate model configurations. The dissertation closes with a summary of the obtained insights and suggestions on further steps in this research field in Chapter 8.

2 State of the art

The present chapter focuses on the description of the state of the art of the characterization method EPIS. First, pioneering works of EPIS are presented, including the initial idea and applications to devices other than the PEMFC. Subsequently, published results of three different working groups are reviewed who applied EPIS to a PEMFC. Thereafter, the EPIS-related approach CFRA, also applied to a PEMFC, is reviewed. In addition to the state of the art of EPIS, a brief overview of different types of PEMFC models is presented. The chapter closes with a summary of the identified research gaps.

2.1 Pioneering works of EPIS

The general idea of applying new measurement techniques similar to EIS, by using nonelectrical quantities in addition to conventionally used electrical quantities, was already described in 1994 by Gabrielli and Tribollet [29]. In 2010, Niroumand et al. [30] revived this idea in the context of a PEMFC. They reported a communication paper on their experiment with a PEMFC in which they measured an increase in the amplitude of observed cell voltage oscillations by decreasing the cathode stoichiometry. They noticed that the cell voltage and the cathode outlet pressure oscillated with an identical frequency. At a frequency of 0.14 Hz the oscillation of both quantities was stated to be in antiphase. They described this observation as a counterintuitive result, as they would have expected an increase of cathode pressure to lead to a higher cell voltage, due to an improvement of the reaction kinetics. Based on this finding, they encouraged other researchers to further investigate pressure-induced voltage oscillations at low frequencies to develop a diagnostic tool with capabilities similar to EIS. The two described works gave rise to the idea of using pressure as a dynamic state variable in FRA experiments in addition to current and voltage.

The approach can be applied to different type of electrochemical cells having a gas phase [31]. It can be an open system in which gas is flowing in and out, such as fuel cells, or a closed system with a closed gas reservoir, such as specific batteries. The first publications of further research of the described approach were made in the context of battery-type cells. In 2014, Hartmann et al. [32] introduced the term EPIS for studying pressure dynamics in relation to an electric state variable in the frequency domain. In their combined experimental and simulative study of a metal-oxygen battery, they applied a sinusoidal current to the cell and measured the pressure response of the enclosed gas reservoir above the oxygen electrode. The transfer function was calculated as the relationship between the Fourier transform of the transferred charge Q, due to current excitation, and the Fourier transform of the pressure response p according to

$$Z_{p/Q}(\omega) = \frac{\mathcal{F}\{\Delta p(t)\}}{\mathcal{F}\{\Delta Q(t)\}} \,. \tag{1}$$

They conducted the experiments in the frequency range between 2–200 mHz. The spectrum of the transfer function shows a strictly monotonic decrease in magnitude and phase shift over the whole frequency range. They supported their experimental results by simulations, which reveal sigmoidal curves for the magnitude and phase with an inflection point of the magnitude around 20 mHz. By increasing the electrode thickness or by decreasing the oxygen diffusion coefficient, the simulated curves get shifted towards lower frequencies. With this parameter variation, they could show the sensitivity of the transfer function towards transport-related parameters.

In 2016, Grübl et al. [31] published a simulative study of EPIS in an electrochemical cell with a closed gas reservoir. They discussed possible transfer functions in which they related the pressure to the cell current, to the transferred electric charge (see Eq. 1), and to the cell voltage. In case of the first two transfer functions, they proposed to excite the current and measure the resulting pressure response. For the latter transfer function, they proposed to excite the pressure of the gas phase and measure the cell voltage response. In their application of an electrochemical cell with a closed gas reservoir, the transfer function $Z_{p/Q}$ was found to be most convenient, as used by Hartmann et al. [32].

Grübl et al. simulated different transport mechanisms and showed that the gas diffusion layer (GDL) in combination with a closed gas reservoir creates distinct features in the spectra. The magnitude shows a constant value at the lowest frequency and decreases in the range from 0.01–1 Hz down to zero revealing a sigmoidal shape. The phase shift decreases continuously from zero at the lowest frequency to below –360° above 1 Hz. They explained that the phase shift physically means that the dynamic pressure response of the gas reservoir is increasingly delayed compared to the current excitation for increasing frequencies.

Furthermore, the authors made a comparison between conventional EIS and EPIS by simulating a sodium-oxygen cell. It shows that the spectra of both methods reveal features in different frequency ranges, thus characterizing different processes. Additionally, they made a sensitivity analysis for both FRA techniques. EPIS revealed a higher sensitivity towards transport related parameters, while EIS was more sensitive to electrochemical parameters. This finding supported the previous hypothesis of both methods characterizing different processes and thus made EPIS a potentially complemental tool to EIS.

2.2 EPIS in PEMFCs

After the introduction of pioneering works of EPIS, the state of the art of EPIS in context of a PEMFC is presented in the following. To date, the existing literature comprises three different experimental approaches of EPIS in a single-cell PEMFC, published by

Engebretsen et al. [19], Shirsath et al. [14–17], and Zhang et al. [18]. All approaches performed a harmonic pressure excitation at the cathode outlet and measured the cell voltage response under galvanostatic control. The analyzed transfer function was then calculated as the relationship between the Fourier transform of the cell voltage response and the pressure excitation at the cathode channel outlet according to

$$Z_{V/p}(\omega) = \frac{\mathcal{F}\{\Delta V_{\mathrm{cell}}(t)\}}{\mathcal{F}\{\Delta p_{\mathrm{CCH}}^{\mathrm{out}}(t)\}} . \quad (2)$$

The major difference between the approaches is that Engebretsen et al. used a loudspeaker for the pressure excitation, whereas Shirsath et al. and Zhang et al. used a pressure controller. In the following, each approach and the published results are reviewed in detail.

2.2.1 Excitation with loudspeaker by Engebretsen et al.

This section about the experiments of Engebretsen et al. is divided into a description of the experimental setup and a review of the results of the measured cell voltage response to the pressure excitation.

Experimental setup

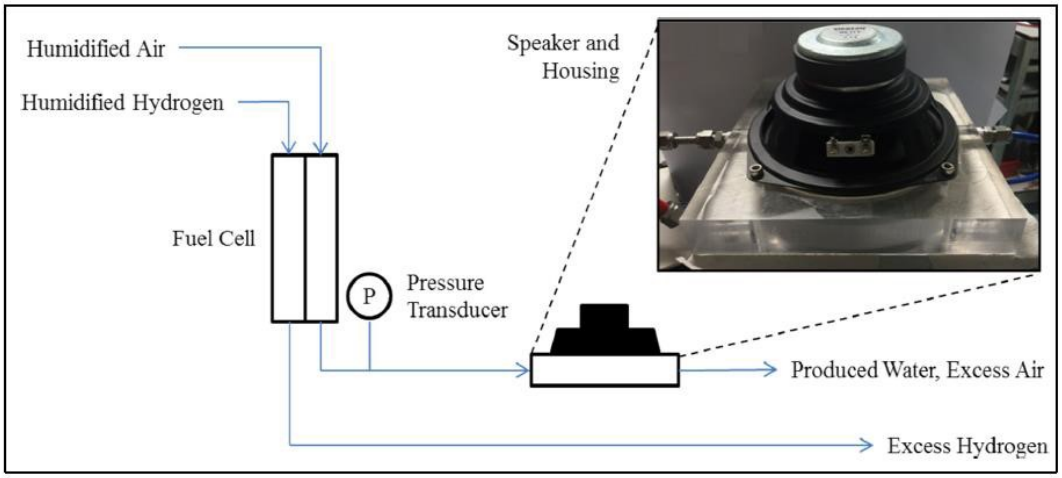

Figure 1: Experimental EPIS setup of Engebretsen et al. with pressure excitation of the PEMFC at the cathode outlet by the use of a loudspeaker. The figure is extracted from Engebretsen et al. [19].

In 2017, Engebretsen et al. [19] published the first article about EPIS applied to a PEMFC. They excited the cathode outlet pressure with a loudspeaker by applying a pressure amplitude of 60 Pa in the frequency range between 0.01–100 Hz. The lower frequency limit was determined by the limitations of the loudspeaker, whose amplitude starts to drop for frequencies below 10 mHz. The experimental setup is shown in Figure 1. The analyzed transfer function $Z_{V/p}$ is defined in Eq. 2; note that the authors did not make a Fourier transform of the measures, but rather used a manual sinusoidal fit to obtain the amplitude and phase of the oscillating cell voltage and outlet pressure.

The analyzed PEFMC had an active area of 5 cm^2 and a double serpentine flow-field operated in co-flow mode. Neither the type of GDL nor the gas volume of the humidifier used in the experiments were specified. The gas feed flow rates were fixed to 100 ml min^{-1} hydrogen at the anode and to 250 ml min^{-1} air at the cathode, both humidified with a relative humidity of 70%.

Cell voltage response

The EPIS results revealed a considerable noise, which may have been caused by the small excitation amplitude of 60 Pa or a superposition of other voltage or pressure fluctuations, as observed by Niroumand et al. [30]. The Fourier transform of the measured pressure and voltage signal could have led to a decrease in the scattering of the spectra, by considering only oscillations of the excitation frequency. Nevertheless, some trends of the magnitude and phase shift of the spectra can be observed.

The first EPIS study in their paper was a variation of different current densities, which is displayed in Figure 2. At open-circuit voltage (OCV) the magnitude $|Z_{V/p}|$ was stated to be insensitive to the excitation frequency. They mentioned the corresponding value of 0.15 µV Pa^{-1} to be consistent with the theoretic change of equilibrium potential with cathode pressure.

Under cell load, the spectra of the magnitude changed qualitatively. The magnitude shows a constant value in the low-frequency range between 0.01–1 Hz followed by a decrease down to zero above 70 Hz. The authors associated this characteristic decrease with processes having a time constant below one second, without naming a specific process.

Quantitatively, the magnitude at low frequencies substantially increased with increasing current density from 5 µV Pa^{-1} at 0.4 A cm^{-2} up to 40 µV Pa^{-1} at 1.2 A cm^{-2}. This trend was justified by the argument that pressure changes have an increased effect on cell performance at higher cell polarization and lower stoichiometries. In this context, it is interesting to mention the cell voltage change that the authors measured for a pressure increase at the cathode outlet at steady state. For an increase of gauge pressure from 0 kPa to 62.1 kPa, the voltage change was measured at OCV with 0.16 µV Pa^{-1}. A comparison of the voltage change at steady state with the quasi-static magnitude of the EPIS measurements at OCV reveals a similar value of 0.15 µV Pa^{-1}. However, under load at 1.6 A cm^{-2}, the same pressure increase led to a steady-state cell voltage change of 2.4 µV Pa^{-1}, which is substantially lower than the quasi-static magnitude of 40 µV Pa^{-1} at 1.2 A cm^{-2}. This observation is surprising, because the quasi-static magnitude of EPIS is expected to approach the value at steady state. It is hypothesized that the quasi-static state is not reached at the lowest applied frequency of 10 mHz. This explanation is supported by the phase shift $\varphi(Z_{V/p})$, which is not 0° at the lowest recorded frequency.

The phase shift shows a monotonic decrease over the whole frequency range, exceeding –360° at 100 Hz. The authors argued that, due to the decrease of the wave length of the

pressure excitation with increasing frequency, more than one oscillation may be required before a voltage response of the PEMFC is observed, hence, resulting in a phase shift below –360°. Therefore, the phase shift is strongly dependent on the cell geometry and the location of the pressure oscillation source relative to the cell. To prove this explanation, the propagation of the pressure front needs to be further investigated. The spectra of the phase shift show no significant dependence on the current density; note that the phase shift at OCV is not presented.

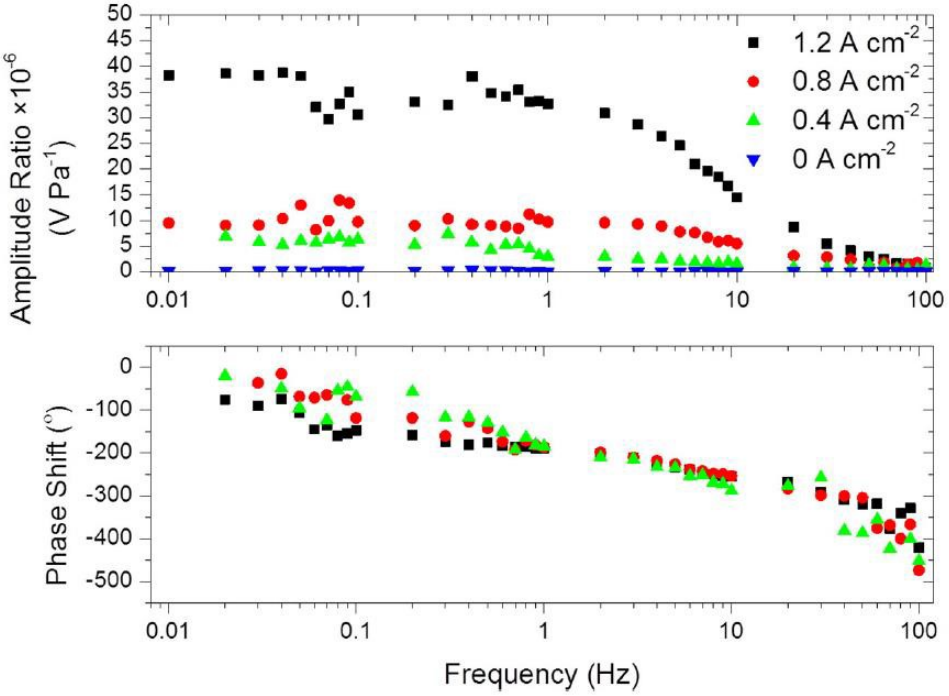

Figure 2: Bode plot of EPIS results obtained by Engebretsen et al. for different current densities. The top panel shows the amplitude ratio between the cell voltage and the cathode outlet pressure oscillation and the bottom panel the corresponding phase shift. The figure is extracted from Engebretsen et al. [19].

The authors made another EPIS study by changing the humidification of the gas inlet streams. It shows that the magnitude $|Z_{V/p}|$ increased for dry inlet gas streams compared to humidified gases, with a stronger increase in case of a dry anode. As a consequence, the authors claimed that water imbalances can be indirectly measured with EPIS.

2.2.2 Excitation with pressure controller by Shirsath et al.

This section reviews the experiments of the project partner to which the present model was parametrized and which are partially reproduced in Chapters 5 and 6. It starts with a description of the experimental setup. Subsequently, the results of the fuel cell response to the pressure excitation are reviewed. First, the pressure response of the fuel cell is described, followed by the cell voltage response for the operation with air, for changing gas compositions, and for pure oxygen.

Experimental setup

The second experimental approach of EPIS in a PEMFC was applied by Shirsath et al. [14–17]. Although the general principle is the same as in Engebretsen et al., there are differences in the experimental setup, which is shown in Figure 3. One difference is that they used an elastomer sealed pressure controller to perform the pressure excitation instead of a loudspeaker. Due to the dynamic limitations of the experimental setup, the upper limit of the frequency range was 1 Hz.

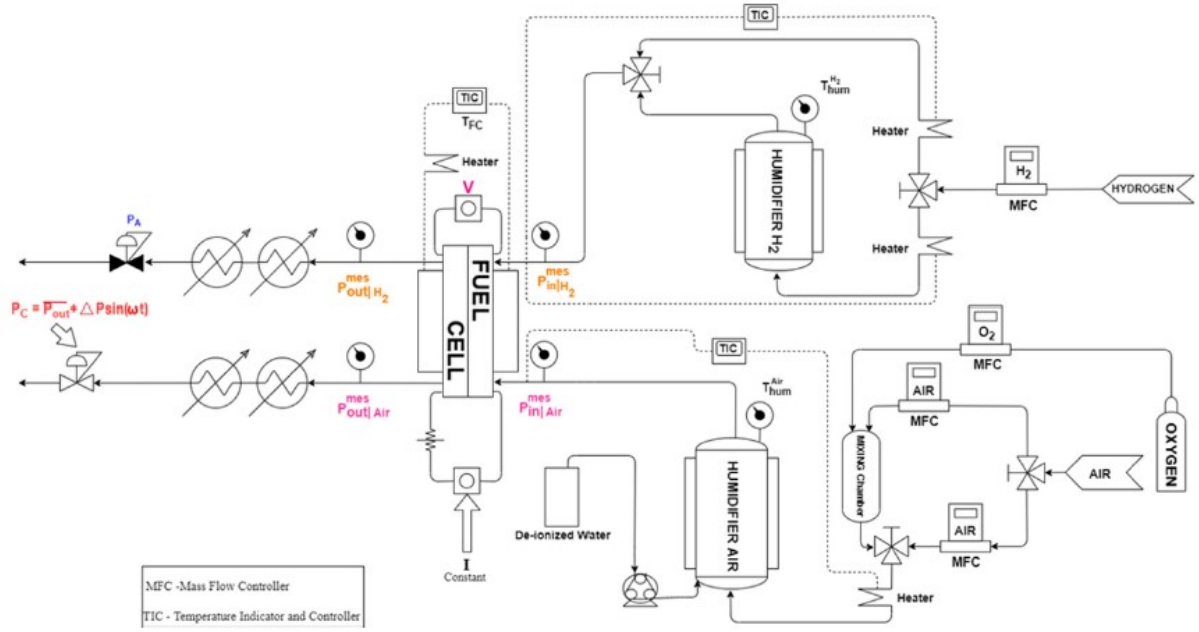

Figure 3: Experimental EPIS setup of Shirsath et al. with pressure excitement of the PEMFC at the cathode outlet by the use of a pressure controller. The figure is extracted from Shirsath et al. [17].

Another difference is the variation of the pressure excitation amplitude with frequency. They reported to use a pressure amplitude of 2500 Pa from 1–10 mHz with a reduction down to 200 Pa above 0.2 Hz [17]. The variation of pressure amplitude was justified by conflicting requirements for the pressure excitation. To limit the distortion of the measured cell voltage, it is an advantage to apply a higher excitation amplitude. On the contrary, to attain a linear response of the system and to prevent reactant starvation, the amplitude should be kept preferably small. Reactant starvation can occur as a consequence of an oscillating inlet flow rate. As the amplitude of the oscillating inlet flow rate increases with frequency, the authors had to decrease the pressure amplitude at higher frequencies [17]. The origin of the oscillating inlet flow rate is discussed more detailed subsequently.

The authors analyzed a PEMFC with an active area of 100 cm^2 and multiple serpentine flow fields with 23 channels operated in counterflow. They supplied dry gas at the anode and humidified gas at the cathode with a gauge pressure of 15 kPa at both outlets. They

kept the water level in the humidifier constant so that the gas volume in the humidifier was 850 ml with a tolerance of 50 ml [17].

Pressure response

To analyze the propagation of the pressure excitation along the gas channel first, the authors [14,17] calculated a transfer function between the measured inlet and outlet pressure oscillation (in Figure 3 $P^{mes}_{in|Air}$ and $P^{mes}_{out|Air}$) according to

$$Z_{p/p}(\omega) = \frac{\mathcal{F}\left\{\Delta p^{in}_{CCH}(t)\right\}}{\mathcal{F}\{\Delta p^{out}_{CCH}(t)\}} . \quad (3)$$

Figure 4 shows experimental and simulated spectra of the transfer function for different gas volumes in the humidifier upstream the cathode inlet. The simulated results were obtained by using an equivalent circuit model. The equivalent circuit comprises a source for the constant flow rate into the humidifier, a capacitor representing the capacitive behavior of the humidifier, a resistor for the pressure drop along the gas channel, and a reference pressure representing the harmonic pressure excitation at the outlet. The pressure drop was measured, whereas the capacitance could be calculated with the actual gas volume in the humidifier. With the given circuit, the authors could accurately reproduce the measured pressure dynamics at the inlet.

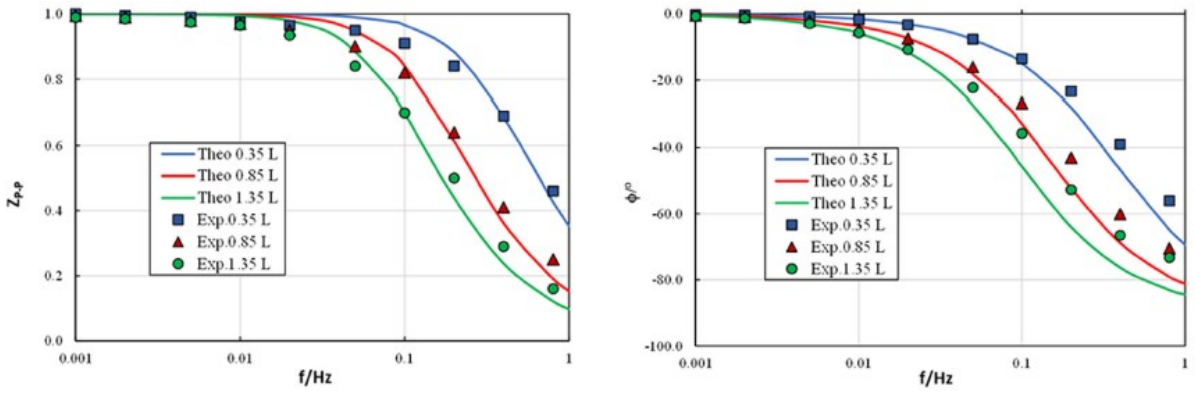

Figure 4: Bode plot of simulated (solid lines) and experimental spectra (squares, triangle and circles) of the transfer function $Z_{p/p}$ between the gas channel inlet oscillation and the outlet pressure excitation for different gas volumes in the cathode humidifier. The figure is extracted from Shirsath et al. [17].

The spectra, shown in Figure 4, revealed that with increasing frequency the inlet pressure oscillation is damped, visible as a decrease in magnitude, and delayed, visible as a decrease in phase shift, in relation to the pressure oscillation at the outlet. For a gas volume of 850 ml, the inlet pressure oscillated at 1 Hz with a remaining amplitude of 20% compared to the outlet pressure amplitude and with a phase shift of about −70°.

By varying the gas volume in the humidifier, the authors were able to show the strong influence of the humidifier on the frequency dependence of this phenomenon. An increase

in gas volume led to a shift of the damping and delay of the pressure oscillation towards lower frequencies.
The authors discovered another important effect of the humidifier. The inlet flow rate at the cathode, which corresponds to the outlet stream of the humidifier, was oscillating during pressure excitation, although the gas feed into the humidifier was kept constant [17]. They explained this phenomenon with the gas volume inside the humidifier acting as a reservoir for the gas. In other words, the combination of a constant gas feed into the humidifier with an oscillating amount of gas inside the humidifier, due to oscillating pressure, results in an oscillating flow rate out of the humidifier.
With their equivalent circuit model, the authors were able to quantify the oscillating inlet flow rate and could show that this effect amplifies with increasing excitation frequency. Furthermore, they reported that increasing the gas volume in the humidifier leads to increased inlet flow rate oscillations, which can even result in reactant starvation at higher frequencies. Favorable low gas volumes in the humidifier were stated to be limited by the occurring entrainment of water droplets, for which reason they kept the gas phase volume at 850 ml as a compromise.

Cell voltage response for operation with air

After summarizing the preparative works of Shirsath et al., in the following, the results of the cell voltage response to pressure excitation by means of the transfer function $Z_{V/p}$ are reviewed. First, typical common features of the spectra where the fuel cell was operated with air as the cathode gas feed are discussed.
Figure 5 shows two examples of the characteristic spectra which Shirsath et al. observed for the operation with air. The magnitude $|Z_{V/p}|$ is nearly constant below 10 mHz followed by an increase with frequency up to a maximum slightly below 1 Hz. A comparison with the results of Engebretsen et al. [19] shows that their progression of magnitude is qualitatively different, as they observed a constant magnitude in the overlapping frequency range between 0.01–1 Hz.
The phase shift $\varphi(Z_{V/p})$ that Shirsath et al. measured for the operation with air, typically shows a continuous decrease from 0° at 1 mHz to about –200° at 1 Hz. The authors attributed the negative phase shift to the phenomenon of diffusion [16]. In the common frequency range between 0.01–1 Hz, the phase shift agrees qualitatively and quantitatively with the experiments of Engebretsen et al. [19].
Shirsath et al. presented a comprehensive study of EPIS by changing numerous operational and a few structural fuel cell parameters. In the following, the variation of parameters and the observed influence on the transfer function $Z_{V/p}$ for the operation with air is reviewed.
A quantitative analysis of the measured magnitude at the lowest analyzed frequency reveals values between 0.5 µV Pa^{-1} and 2.4 µV Pa^{-1} for all parameter variations. The

variation of the current density showed that the quasi-static magnitude distinctively increased with current density [14,28]. This trend of increasing quasi-static magnitude with current density was also observed by Engebretsen et al. [19], although to a stronger extent. An increase in relative humidity led to a small increase in quasi-static magnitude, which was more pronounced at higher current densities [14]. The change of the GDL from a product with microporous layer (MPL) to one without also led to a small increase of the quasi-static magnitude [16] (cf. Figure 5). The oxygen stoichiometry revealed no significant influence on the quasi-static magnitude [16].

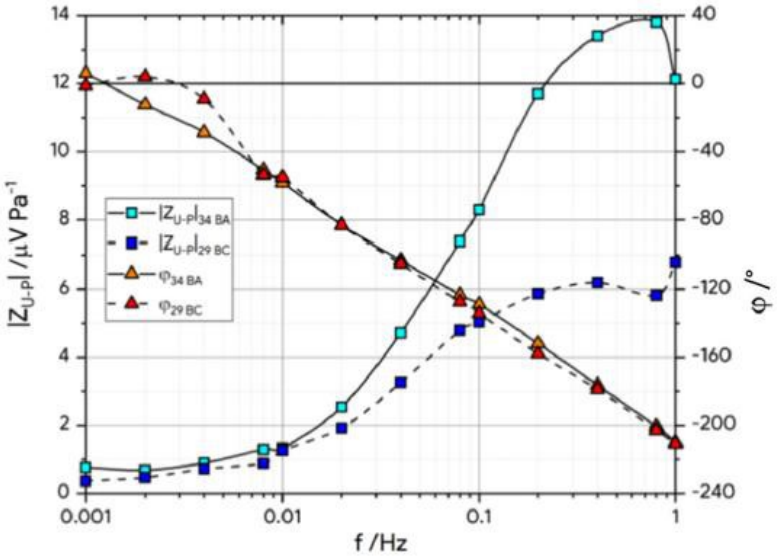

Figure 5: Typical spectra of the transfer function $Z_{V/p}$ between the cell voltage oscillation and the outlet pressure excitation for operation with air as the cathode gas feed. The magnitude is displayed on the left axis and the phase shift on the right axis. Comparison of two different GDLs (34 BA: without MPL, 29 BC: with MPL) operated at 0.2 A cm^{-2} with λ_{O_2} = 2.5, T = 55 °C and φ_C = 20%. The figure is extracted from Shirsath et al. [16].

A quantitative analysis of the characteristic maximum of the magnitude reveals different dependencies on the parameters. The authors reported a strong influence of the oxygen stoichiometry on the maximum magnitude [16]. The maximum increased from 3 µV Pa^{-1} for an oxygen stoichiometry of 4 to 27 µV Pa^{-1} for an oxygen stoichiometry of 1.5 at a current density of 0.2 A cm^{-2}. The authors related the increase of magnitude for reduced stoichiometry to diffusion phenomena, which become more rate-controlling when oxygen is higher depleted.

To further analyze the influence of diffusivity on EPIS, the authors made an experiment in which they replaced the inert gas nitrogen by helium, in which oxygen is reported to have a four times higher diffusivity [16]. The maximum magnitude revealed a decrease of 20%, which supported their presumed correlation between diffusion phenomena and maximum magnitude.

The change of the GDL from a product with MPL to one without resulted in a strong increase of maximum magnitude from 6 μV Pa^{-1} to 14 μV Pa^{-1}, at a low current density of 0.2 A cm^{-2} and a relative humidity of 20% (cf. Figure 5). Operation of the fuel cell using the GDL without MPL at 1.0 A cm^{-2} and 100% relative humidity led to an even stronger increase of maximum magnitude to more than 50 μV Pa^{-1}. The authors related this observation to an increase of mass transport resistance due to the poor water management of the GDL [15].

For the dependencies between the phase shift $\varphi(Z_{V/p})$ and the parameters, the authors observed the following trends. They reported the phase shift to be relatively independent of the current density and gas feed humidification [14]. Changing the GDL from a product with MPL to one without also led to a similar phase shift at low current density and humidification (cf. Figure 5). However, at high current density and humidification the phase shift revealed a substantial change to 170° at 1 mHz, with a subsequent decrease to nearly –250° at 1 Hz. The authors attributed the strong change in phase shift to flooding conditions, as a consequence of poor water management of the MPL-free GDL. The phase shift of about 180° at 1 mHz is surprising, as it means that the increase of pressure leads to a decrease in cell voltage, whereas in all other experiments the opposite trend was observed at quasi-static conditions.

Furthermore, a trend of the phase shift for a change in oxygen stoichiometry was observed. A decrease in stoichiometry led to more negative values of the phase shift in the complete frequency range. The authors related this trend to diffusion phenomena, similar to the explanation for the change of magnitude with stoichiometry.

Cell voltage response for operation with varying gas compositions

Shirsath et al. [17] performed another set of experiments for different cathode gas feed compositions, by stepwise increasing the oxygen molar fraction from air towards pure oxygen. They kept the flow rate constant, so that the oxygen stoichiometry increased accordingly. The magnitude at the lowest frequency of 10 mHz varied in the range of 0.5–1.0 μV Pa^{-1} with a decreasing trend towards pure oxygen. Qualitatively, the typical progression of magnitude for air, with an increase up to a maximum around 1 Hz, changed by increasing the molar fraction of oxygen. For an oxygen molar fraction of 0.5 the maximum was already reduced and vanished completely for molar fractions of 0.8 and higher. A more detailed examination of the spectra for pure oxygen is given subsequently.

Furthermore, the characteristic progression of phase shift for air, with a continuous decrease down to –200° at 1 Hz, also changed. Towards pure oxygen the phase shift became less. The authors argued that the changes in magnitude and phase shift with oxygen concentration can be linked to the diffusion of oxygen in nitrogen.

Cell voltage response for operation with pure oxygen

In the following, spectra of the transfer function $Z_{V/p}$ are discussed in which the authors operated the fuel cell with pure oxygen as the cathode gas feed. Figure 6 shows spectra for a variation of the oxygen stoichiometry. Qualitatively, all spectra show a similar progression of magnitude $|Z_{V/p}|$. The magnitude is nearly constant below 10 mHz, which is similar to what has been observed with air as the gas feed. But, in the frequency range of 0.01–1 Hz the magnitude decreases, which is the opposite trend compared to the spectra obtained under operation with air.

The phase shift $\varphi(Z_{V/p})$ revealed also a qualitatively different progression than under operation with air. The spectra show a continuous decrease down to a minimum around 0.1 Hz with a subsequent increase.

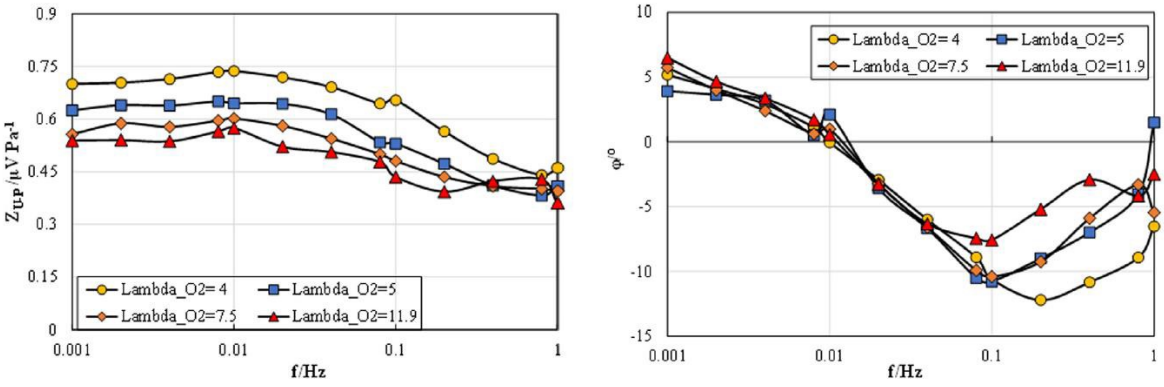

Figure 6: Bode plot of transfer function $Z_{V/p}$ between the cell voltage oscillation and the outlet pressure excitation for operation with pure oxygen as the cathode gas feed at different oxygen stoichiometries. The cell was operated at 1.0 A cm^{-2} and φ_C = 100%. The figure is extracted from Shirsath et al. [17].

Similar to the experiments with air, the authors made numerous experiments for the operation with pure oxygen by changing operational and structural parameters. Quantitatively, the quasi-static magnitude was measured in the range of 0.4–1.4 µV Pa^{-1} with a decrease down to 0.2–0.6 µV Pa^{-1} at 1 Hz, depending on the parameter configuration [15–17]. The phase shift at the lowest frequency of 1 mHz was measured always positive between 0°–10°. The minimum phase shift around 0.1 Hz was between –10° and –30° with a subsequent increase towards 0°.

By changing the stoichiometry of the gas feed (cf. Figure 6), an increase of quasi-static magnitude with a decrease of stoichiometry was observed, while the phase shift showed no clear trend. A comparison of an aged and fresh MEA revealed an increase in quasi-static magnitude for the aged MEA and a nearly unchanged phase shift [16].

The change of the GDL from a product with MPL to one without resulted in an increase of the quasi-static magnitude by 20% and a lower minimum phase shift, operated at 0.2 A cm^{-2} and a relative humidity of 20% [16]. A similar trend between the magnitude of

both type of GDLs was observed at an increased current density of 1.0 A cm^{-2} and a relative humidity of 100% [15]. The comparison of a third GDL, also without MPL but not PTFE-treated as the other two GDLs, revealed an even stronger increase of magnitude at the lowest frequency. The authors related this observation to the poorer water management.

Although the quasi-static magnitude showed a clear trend for a change of specific parameters, one should keep in mind that this information could presumably be obtained without EPIS by simply analyzing the static pressure-voltage response.

2.2.3 Excitation with pressure controller by Zhang et al.

This section about the EPIS experiments of Zhang et al. is divided into a description of the experimental setup and a review of the results in terms of pressure response and cell voltage response to the pressure excitation.

Experimental setup

The recently published experimental approach of EPIS by Zhang et al. [18] is quite similar to the approach of Shirsath et al. They excited the outlet pressure of the cathode with an electro-pneumatic pressure controller, using an amplitude of 1 kPa within the frequency range of 2–100 mHz. The scheme of their experimental setup is shown in Figure 7.

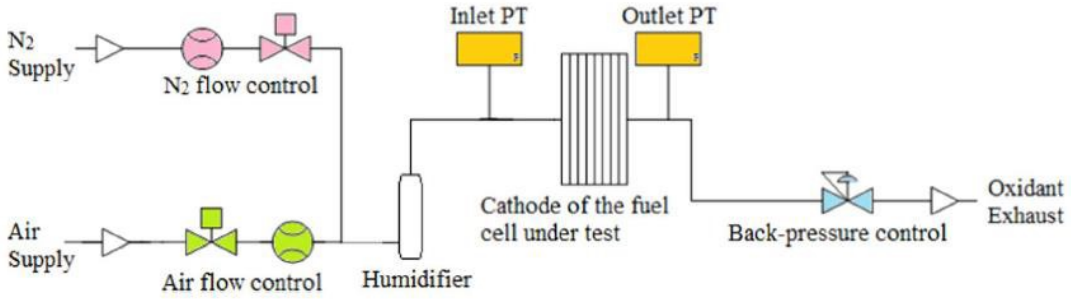

Figure 7: Experimental setup of Zhang et al. for EPIS in a PEMFC with excitation of the cathode outlet pressure by the use of a pressure controller. The system components are shown for the cathode gas stream. The figure is extracted from Zhang et al. [18].

The authors analyzed two different fuel cells, one with an active are of 50 cm^2 with a serpentine flow field and another one with an active area of 12 cm^2 with a parallel flow field. Both cells had a GDL with MPL, treated with PTFE. Other than in the setup of Shirsath et al., the authors humidified both the anode and cathode gas feed with 90% relative humidity. The gas phase volume in the humidifier was not specified, but referred to as “large volume”. The gauge pressure was 100 kPa at both sides.

Pressure response

Similar to Shirsath et al., the authors made a preliminary study on the relationship between the pressure response at the inlet and the pressure excitation at the outlet with both fuel cells. Instead of presenting the transfer function between inlet and outlet

pressure, they reported fitted parameters of an RC-equivalent circuit model, used to reproduce the measured pressure response. The model is similar to the one proposed by Shirsath et al., but additionally considers the reduced amplitude of inlet pressure oscillations at the quasi-static frequency.

Qualitatively similar to Shirsath et al., Zhang et al. observed an increased damping and delay of the outlet pressure excitation towards the channel inlet with increasing frequency. However, their interpretation of the study is different. The authors claimed that they excluded the influence of the gas volume of the humidifier in their experiments. Therefore, they related the capacitive behavior to the gas channel flow field, which also provides a certain storage volume for gas. This interpretation contradicts the observation by Shirsath et al. [17], who clearly demonstrated the influence of the gas volume in the humidifier on the inlet pressure response. Furthermore, it is questionable how Zhang et al. were able to isolate the effect of the humidifier with their presented experimental setup.

Comparing the characteristic frequency for both tested fuel cells at which the amplitude of inlet pressure oscillation has dropped by 50%, revealed that the characteristic frequency of the 50 cm^2 cell was lower than for the 12 cm^2 cell at the same flow rate. The authors deduced that the change in the capacitive behavior can only be related to the change of the channel flow field, as the humidifier is the same for both setups.

By varying the flow rate, Zhang et al. were able to show that the characteristic frequency decreased with increasing flow rate. Another observation was the decrease of the inlet pressure amplitude at quasi-static frequency with increasing flow rate. The authors attributed this phenomenon to the interaction between the mass flow controller and the pressure oscillation at the gas channel inlet.

Cell voltage response

In their EPIS analysis Zhang et al. made studies for both type of fuel cells and varied operational parameters such as current density, stoichiometry, flow rate and gas composition. In the Bode representation, the EPIS results revealed an increase of magnitude $|Z_{V/p}|$ with frequency for operation with air, at all current densities in case of the 12 cm^2 cell and at high current densities in case of the 50 cm^2 cell. This is qualitatively the same what Shirsath et al. observed in their experiments. For the operation of the 50 cm^2 cell at current densities ≤ 0.66 A cm^{-2}, the magnitude revealed a decrease with frequencies. The authors stated that the small voltage amplitude measured at those current densities is not suitable for diagnostics, due to interference with the background noise.

The authors measured quasi-static magnitudes ≤ 2 µV Pa^{-1}, which is in a similar range as the measurements of Shirsath et al. Another similarity is the increase of the quasi-static magnitude with current density. Zhang et al. related the quasi-static magnitude to the change of the Nernst potential with pressure.

The maximum magnitude was observed to increase with current density. At first glance, this is different to what Shirsath et al. observed, who reported a similar or an even smaller maximum magnitude at higher current densities [14]. The reason for this difference is most probably the different operating conditions. Zhang et al. made their current density study with a fixed flow rate, while Shirsath et al. maintained the oxygen stoichiometry instead. As the stoichiometry was observed to have a strong influence on the maximum magnitude, the decrease in stoichiometry is expected to be responsible for the increase in maximum magnitude observed by Zhang et al.

A comparison of the maximum magnitude between the 50 cm^2 and the 12 cm^2 cell revealed a striking difference at the highest current density. At 1.0 A cm^{-2} the magnitude of the bigger cell reached only a maximum of 2 µV Pa^{-1} for an oxygen stoichiometry of 2, whereas the smaller cell reached a maximum of 40 µV Pa^{-1} for a stoichiometry of 3. The authors related this observation to the structural differences between both cells which were a different gas channel flow field and fuel cell area.

The phase shift $\varphi(Z_{V/p})$ observed by Zhang et al. was stated to approach 0° towards the lowest applied frequency and is therefore expected to approach the cell response at steady state. With increasing frequency, the phase shift continuously decreased down to –160° at 0.1 Hz. This progression of phase shift is similar to the observation of Shirsath et al. For small current densities applied to the bigger cell the decrease in phase shift was less pronounced.

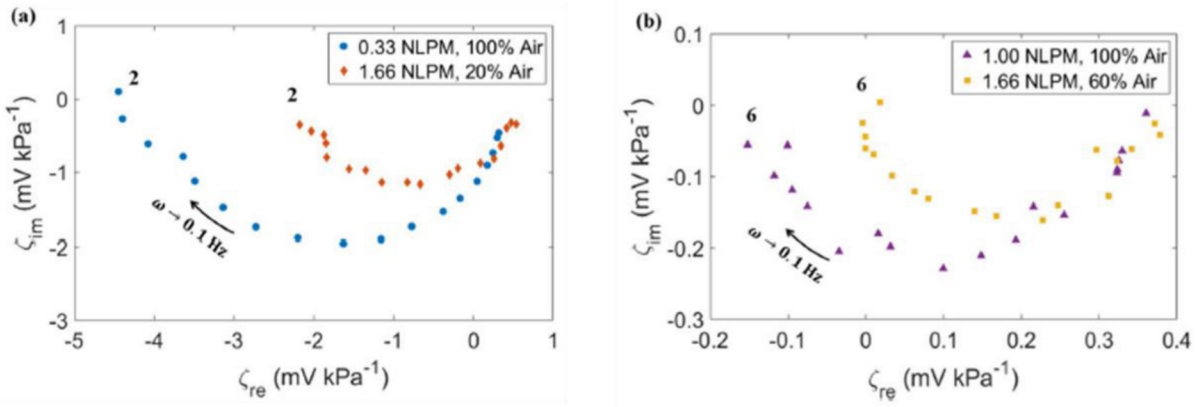

Figure 8: Nyquist plot of transfer function $Z_{V/p}$ between the cell voltage oscillation and the outlet pressure excitation with different cathode gas compositions. The 50 cm^2 cell was operated at 0.2 A cm^{-2} with λ_{O_2} = 2 (left panel) and λ_{O_2} = 6 (right panel). The figure is extracted from Zhang et al. [18].

The remaining studies were presented in the Nyquist representation, which makes comparing them to the previous studies more difficult. Nevertheless, some trends can be worked out as follows. The previously described spectra in the Bode representation appear as semicircles in the Nyquist plot, as can be seen in Figure 8. For the 50 cm^2 cell, Zhang et al. varied the flow rate and therefore the oxygen stoichiometry at constant

current density of 0.2 A cm^{-2}. The semicircles in the Nyquist plot showed a strong increase with decreasing oxygen stoichiometry. This agrees with the observed increase in magnitude with decreasing stoichiometry by Shirsath et al [16].
Furthermore, Zhang et al. changed the gas composition by diluting the air further with nitrogen. The reduction of the oxygen molar fraction led to an increase of the diameter of the semicircle. This also agrees with the observation of Shirsath et al., who observed a decrease of maximum magnitude with increasing oxygen molar fraction.
Another experiment made by Zhang et al. with the larger cell revealed an interesting trend. Again, they changed the gas composition by further diluting the cathode gas feed with nitrogen, but this time they kept the oxygen stoichiometry constant, by adjusting the flow rate accordingly. Results of this experiment at a current density of 0.2 A cm^{-2} are shown as a Nyquist plot in Figure 8. Surprisingly, the authors observed a decrease in dynamic voltage response with a more diluted gas mixture, resulting in a two times larger semicircle of the 100% air mixture compared to the 20% air diluted gas mixture. The expectation would have led to the opposite trend, as an increased mass transport hindrance by an increased amount of inert gas is expected to increase the magnitude. At the quasi-static frequency, the expectation seems to persist, as the magnitude is larger here for the diluted gas mixture, but with increasing frequency the proportion in magnitude changes. The authors explanation for this surprising observation is that rather the change in flow rate is the cause for the changing semicircle diameter than the dilution of the gas.

2.3 CFRA in PEMFCs by Sorrentino et al.

Another characterization method closely related to EPIS is called CFRA and has been applied to a PEMFC by the working group of Vidakovic-Koch. The corresponding publications comprise Sorrentino et al. [20–22], which are reviewed subsequently. This subchapter is divided into a description of the experimental setup and a review of the results by means of the cell voltage and the cell current response to the reactant excitation.

Experimental setup

The experimental setup of CFRA is different compared to EPIS in terms of the pressure excitation and the analyzed transfer function. Other than in the experiments described above, in which the total pressure at the cathode outlet was excited, in the CFRA experiments, the partial pressure of reactants at the cathode inlet was excited. The procedure is explained in more detail below.
The analyzed transfer function describes the relationship between the electric cell response and the excited partial pressure at the inlet. This is different to the approaches described above, in which the analyzed transfer function describes the electric cell response to the excited total pressure at the cathode outlet. Under galvanostatic control the

transfer function is calculated as the Fourier-transformed voltage response to partial pressure changes at the inlet according to

$$Z_{V/p(i)}(\omega) = \frac{\mathcal{F}\{\Delta V_{\mathrm{cell}}(t)\}}{\mathcal{F}\{\Delta p_{i,\mathrm{CCH}}^{\mathrm{in}}(t)\}} . \quad (4)$$

Other than the previously described approaches of EPIS in a PEMFC, in which the electric cell response was measured only under galvanostatic control, the authors additionally applied CFRA under potentiostatic control. The transfer function is then calculated as the Fourier-transformed cell current response to partial pressure changes at the inlet according to

$$Z_{i/p(i)}(\omega) = \frac{\mathcal{F}\{\Delta i_{\mathrm{cell}}(t)\}}{\mathcal{F}\{\Delta p_{i,\mathrm{CCH}}^{\mathrm{in}}(t)\}} . \quad (5)$$

The experimental CFRA setup is shown in Figure 9. The excitation of the partial pressure was realized by adding a supplemental stream of a specific gas to the cathode gas feed, controlled by an alternately opening valve with the required frequency. As a consequence of the added gas stream, not only the partial pressure of the added gas was excited, but rather the partial pressure of all species. Assuming that the inert gas nitrogen has no direct effect on the cell voltage and current, the measured cell response can be attributed to the partial pressure changes of water and oxygen.

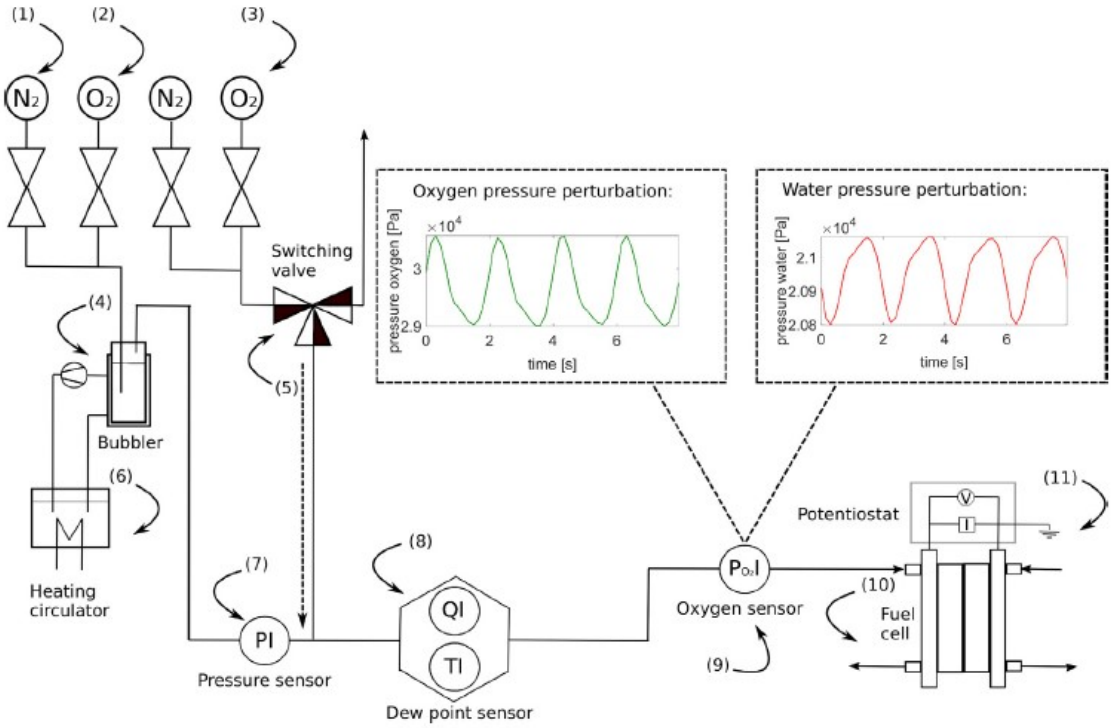

Figure 9: Experimental CFRA setup of Sorrentino et al. with species excitation by the addition of a supplemental gas stream to the cathode gas feed. The figure is extracted from Sorrentino et al. [21].

The coupled electric cell response makes the calculation of separated transfer functions for water and oxygen difficult. In their first experimental study, Sorrentino et al. [20]

added oxygen to the gas feed and the analyzed transfer function contained coupled contributions of oxygen and water pressure changes. In their second experimental study [21] the authors decoupled the electric cell response for changes in water and oxygen pressure. To this end, they extended the set of experiments by additionally using nitrogen as a supplemental gas. Through algebraic rearrangement they were able to calculate decoupled transfer functions for both species.

Sorrentino et al. [21] measured the partial pressure of oxygen at the cathode inlet with a fiber sensor and the partial pressure of water with a dew point meter. They reported a maximum amplitude in oxygen pressure oscillation of 750 Pa and a maximum amplitude of total pressure oscillation of 30 Pa. Due to the dynamic limitations of the experimental setup, the upper limit of the analyzed frequency range was 1 Hz. It is worth mentioning that at low frequencies the electric cell response had the shape of a square wave, while at higher frequencies the shape was more sinusoidal.

The authors analyzed a fuel cell with an active area of 25 cm^2 and a flow field with parallel channel configuration. The GDL of the fuel cell was stated as TGP-H-60, which was not named explicitly to have an MPL.

Cell voltage and cell current response

Sorrentino et al. supported their experimental results by simulations using a 1D PEMFC model [22]. The model had a high degree of freedom, as plenty of parameters were fitted to match the results. The fitted parameters were the cathode charge transfer coefficient, the porosity related to oxygen and water diffusion, the nominal diffusivity in Nafion® and the electroosmotic drag. Furthermore, the parameters were fitted for each spectrum separately and showed a great variety between the simulations. Another drawback of the simulations is that one of the studied dynamics was the oxygen transport in the gas channel. In their 1D model the authors treated the gas channel as a perfectly mixed volume, which prevents the consideration of effects such as gas distributions along the channel. Therefore, the simulated results should be interpreted with caution, although the authors reported a good agreement between the simulations and the experiments.

In the following, the results of the decoupled transfer functions are reviewed, starting with the transfer function that describes the voltage response to changes in the oxygen pressure under galvanostatic control. The corresponding spectra are shown in the left panels of Figure 10. The magnitude revealed a constant value up to 0.1 Hz with a subsequent decrease towards zero. The authors related the decrease in magnitude with frequency to the duration of the gas transport through the channel and the GDL.

The variation of the current density revealed an increase of the magnitude at low frequency with current density. With the derivative of the overpotential with respect to the oxygen pressure, the authors demonstrated that the contribution of cathode reaction kinetics to the magnitude is inversely proportional to the oxygen pressure [21]. Therefore,

at higher current densities at which the oxygen pressure is lower at the catalytic sites, due to a decrease in stoichiometry for a constant flow rate and due to an increase in mass transport resistance, the magnitude is expected to be higher. As a consequence of their finding, the authors proposed to use the transfer function to evaluate the mass transport resistance. It should be stated here that the quasi-static magnitude is most likely approaching the change of cell voltage with oxygen pressure at steady state. Therefore, the evaluation of the mass transport resistance could be obtained by simply increasing the partial pressure statically.

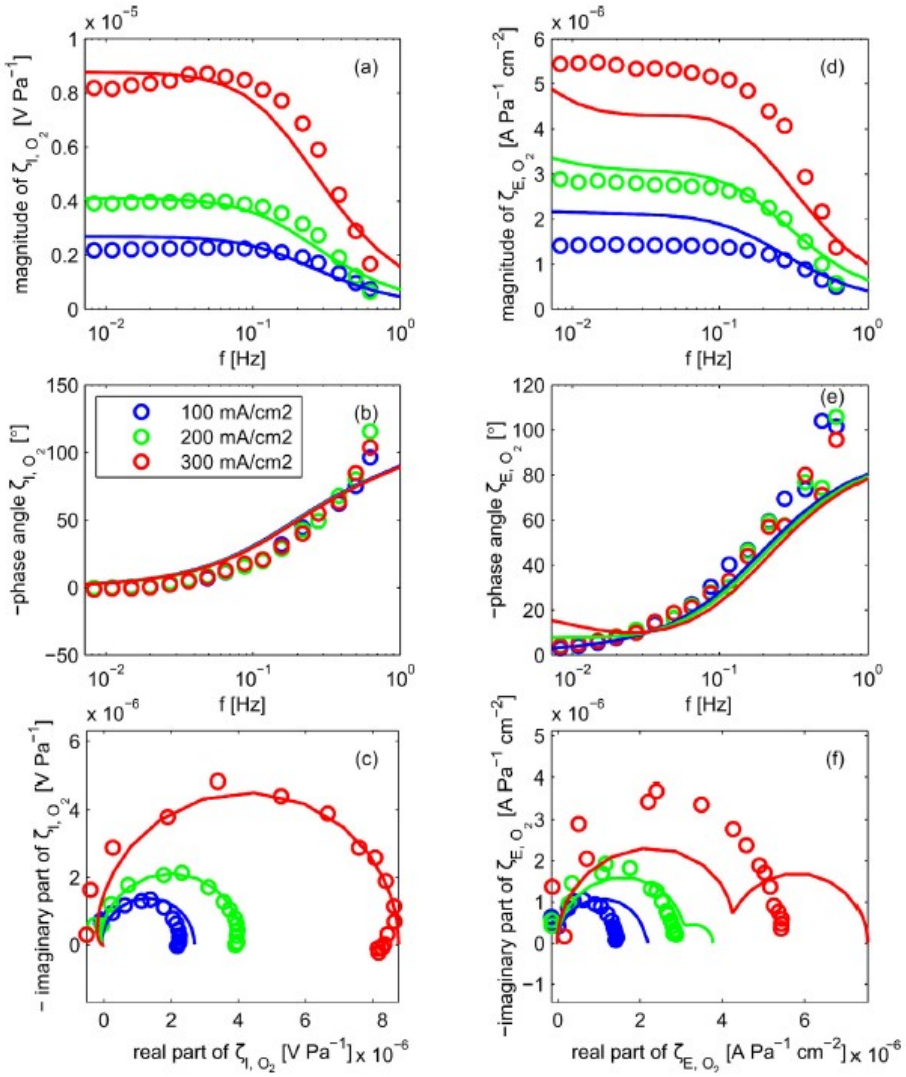

Figure 10: CFRA spectra of the decoupled transfer function $Z_{V/p(O_2)}$between the cell voltage oscillation and the partial pressure excitation of oxygen (left panels) and of the decoupled transfer function $Z_{i/p(O_2)}$ between the cell current response and the partial pressure excitation of oxygen (right panels) at different current densities. The upper rows show the Bode representation, the bottom row the Nyquist representation. The figure is extracted from Sorrentino et al. [21].

A comparison with EIS measurements revealed the following. The magnitude of EIS measurements in the low-frequency region at the same current density showed not the

monotonic dependence on the current density. The authors explain this observation with the superposition of different processes. Therefore, EIS was stated to be less appropriate for the evaluation of the mass transport resistance.
The phase shift of the analyzed CFRA transfer function revealed a continuous decrease from 0° below 10 mHz to –100° around 0.7 Hz. The phase shift was nearly independent of current density.
The spectra of the transfer function between the current density response of the cell related to a change of oxygen pressure under potentiostatic control are shown in the right panels of Figure 10. They are qualitatively similar to the previously described transfer function measured under galvanostatic control, in both magnitude and phase.
The decoupled transfer functions, describing the electric cell response to a change in water pressure, revealed features in different frequency ranges compared to the transfer functions related to the oxygen pressure change shown above. The magnitude of the transfer function obtained under galvanostatic control showed a decrease with increasing frequency in the range from 7–100 mHz. The authors related this change in magnitude to the sorption of water into the electrolyte, which is accompanied by an increase in conductivity and hence an increase in cell voltage.
The magnitude of the transfer function under potentiostatic control revealed a decrease with increasing frequency in the range of 7–30 mHz. The shift of the sorption process towards lower frequencies is explained by the induced change of the electro-osmotic drag as a consequence of the change in current. The electro osmotic drag transports water against the direction of water diffusion. The authors proposed to further exploit this finding to study the water transport driven by diffusion and electro-osmotic drag.

2.4 Continuum modeling of PEMFCs

The aim of this subchapter is to provide a brief overview of the different type of PEMFC models, by referring to examples of the mentioned model type. The overview focuses on continuum models and does not contain atomistic modeling approaches such as molecular dynamics or density functional theory. For a more detailed description of the state of the art in PEMFC modeling the reader is referred to the review papers [33–36].
The complexity of a fuel cell model is dependent on the assumed simplifications of the fuel cell processes and can vary strongly from simple empiric 0D models to detailed physics-based 3D models. The requirement of a detailed fuel cell description competes with the one of economical computational and modeling efforts. Hence, the selected model type necessarily is a compromise between these two considerations. Depending on its application and the focus of the investigation, a different model might be appropriate.
The simplest kind of models are empirical 0D models which describe the relationship between the cell voltage and current based on simple empirical correlations, without

consideration of the spatial domain. This type of model is often used to determine kinetic or ohmic resistance parameters from current-voltage measurements [33]. Examples of this kind of models can be found in Refs. [37–44].

Fuel cell models that additionally consider the spatial domain describe the fuel cell behavior through physics-based equations with the use of a continuum approach. The equations of the subdomains or components of the fuel cell can comprise the conservation equations of mass, momentum, energy, and charge. Figure 11 shows a schematic representation of a PEMFC with indications of the different dimensions. The layer structure of the fuel cell and its function is described more detailed in the context of the modeling domain in Chapter 3.1.1.

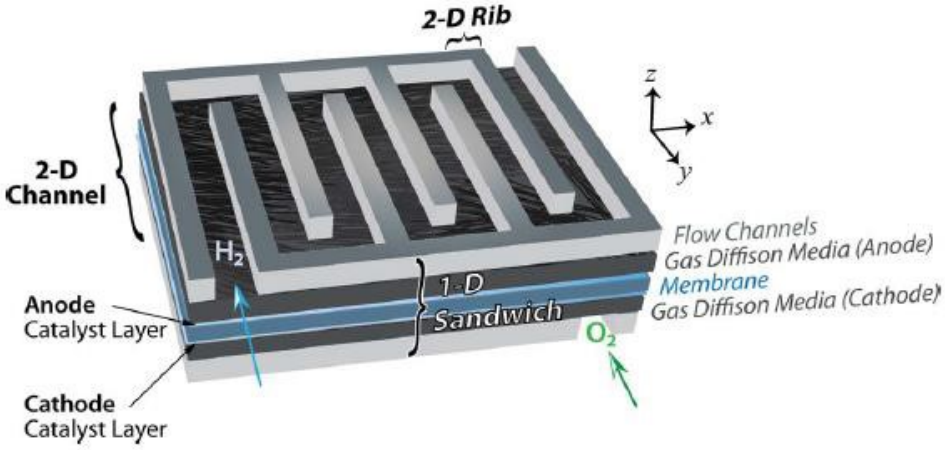

Figure 11: Schematic representation of a PEMFC showing the different dimensions and the sandwich structure between the bipolar plates containing the flow channels. The figure is extracted from [33].

1D models typically describe the fuel cell processes occurring in through-plane direction across the MEA (see Figure 11: 1D sandwich). Basically, they comprise the transport of mass and charge through the porous electrodes and the membrane and the electrochemical reactions at the catalytic sites. Additionally, some models consider the transport of heat.

Two prominent models should be pointed out here which were one of the first 1D models and have been reproduced and modified numerously: the model of Springer et al. [45] and the model of Bernardi and Verbrugge [46]. The first model of Springer et al. was isothermal and treated the electrochemistry through a simple 0D polarization equation. However, they considered the sorption of water into the membrane and the transport of water through the membrane. By modeling the variable water content in the membrane, they were able to show the importance of the membrane hydration to maintain a sufficient proton conductivity. Based on this model the authors made further studies in which they added additional features such as a detailed cathode [47] and anode [48] model as well as

an AC-impedance model [8]. The Bernardi and Verbrugge model, which was published around the same time as the first model of Springer et al., provided a more detailed description of the gas transport in the porous media. Different to the first study of Springer et al. they considered the presence of liquid water, but treated as a constant volume fraction rather than in the form of a true two-phase flow. The Bernardi and Verbrugge model formed the basis for further studies in which the model was extended through additional effects [49–54]. A more recent example of a 1D model was published by Vetter and Schumacher [55] who included the transport of heat and the transport of liquid water through the porous media of the cathode.

The limitation of the 1D model is the assumption that the transport of charge and mass across the MEA is evenly distributed over the remainder dimensions in across-the-channel and along-the-channel direction. However, in reality this is not the case and, dependent on the cell load, the transport situation across the MEA can vary substantially. 2D models extend the previously described 1D models by considering another dimension, in either across-the-channel or along-the-channel direction. The former combination is used to study the effect of the gas channel rib [56–58], which allows the transport of charge and heat but hinders the transport of mass in and out of the adjacent gas diffusion media. The other form of a 2D model combines the direction across the MEA with the direction along the channel [27,59–64]. This type of model considers the important effect of reactant depletion and water accumulation along the channel on the current distribution by approximating the flow channel as a straight channel [33]. Furthermore, by describing the gas transport in the gas channels with the Navier-Stokes equations the dynamic pressure propagation along the channel can be reproduced, which is essential for the simulation of EPIS.

Closely related to these models but with a reduced computational effort are the so-called pseudo-2D models or 1+1D models [23,24,26,65–67]. They describe phenomena in both dimensions, across the MEA and along the channel dimension, without actually solving 2D equations. This kind of approach is justified by the fact that the mass and charge transport in the MEA is mainly occurring across the MEA due to the greater concentration and electric potential gradient compared to the along-the-channel direction.

The technological progress in the field of computing power has led to the development of complex 3D models, which allow the analysis internal states in the 3D domain. The 3D approach was used for example for detailed studies of the two-phase characteristics in PEMFCs [68–71] and for studies of the flow field [72,73]. Similar to the pseudo-2D models, there are pseudo-3D or 1+2D models [74–76].

In the present work the approach of a pseudo-2D model is chosen to be the best compromise between the accurate description of the relevant fuel cell processes on the one hand and the computational and modeling effort on the other hand.

2.5 Research gaps

The pioneering works of EPIS showed its potential as a complementary tool to EIS, by being more sensitive to transport-related parameters. The reviewed experiments demonstrated the feasibility of applying EPIS to PEMFCs. The measured spectra contained features and thus, in principle, information about time-dependent processes. However, to further benefit from these features, it is essential to understand their unknown origin, which will be described more detailed subsequently.

Shirsath et al. and Zhang et al. both measured an increase of magnitude with frequency up to a maximum around 1 Hz, in case the fuel cell was operated with air as the cathode gas feed. The increase in magnitude was accompanied by a continuous decrease in phase shift with frequency. Zhang et al. did not provide an explanation for this observation at all. Shirsath et al. argued that these two major characteristics are related to the process of diffusion based on empiricism, but without explanation of a causal link. Therefore, the origin of these features still needs to be explained on the base of a causal link.

Operated with pure oxygen, the spectra of Shirsath et al. revealed a different progression compared to the operation with air. Instead of increasing with frequency, the magnitude decreased between 0.01–1 Hz, accompanied by a minimum of the phase shift at about 0.1 Hz. The reason for these two features is unknown.

Engebretsen et al. were able to measure spectra up to 100 Hz, but with the disadvantage of obtaining a strong scattering of the data. They observed a decrease in magnitude between 1–100 Hz and related it to processes with a time constant below one second, without going into detail.

The variation of numerous structural and operational parameters revealed a few promising correlations between the parameters and the features of the spectra. In case the fuel cell was operated with air, the experiments revealed a strong dependence of the maximum magnitude on the oxygen stoichiometry, the type of GDL, especially at high current densities, and the cell area or rather the channel length. To further exploit these dependencies, the relationship between the parameters and the extent of magnitude increase needs to be understood.

To comprehend the EPIS features it is necessary to understand the causal link between the cell voltage and the outlet pressure. In this context, Zhang et al. mention the change in equilibrium potential. Sorrentino et al. reason the cell voltage response with the change of overpotential, due to changed reaction kinetics, and the change of conductivity losses in the electrolyte due to a change of the electrolyte humidification. It would be useful to study the three effects together and compare their individual contribution to the overall change of cell voltage.

Shirsath et al. and Zhang et al. both demonstrated that the pressure excitation becomes increasingly damped and delayed along the channel with increasing frequency. While

Shirsath et al. relate this effect to the gas volume of the humidifier upstream the cell, Zhang et al. claim that the effect is rather caused by the gas channel. Neither Shirsath et al. nor Zhang et al. explain how the variation of pressure oscillation along the channel affects the cell voltage response.

Another interesting observation made by Shirsath et al. is the oscillation of the inlet flow rate during pressure excitation. The amplitude of this oscillation increased with frequency. The effect on the cell voltage response needs to be further investigated.

To conclude, the numerous experimental works brought up a lot of questions which need to be answered to further evaluate the potential of EPIS as a useful characterization method of transport processes. As mentioned in the introduction, modeling and simulation can be helpful tools to analyze internal states which are hardly accessible in the experiments. To simulate EPIS, it is essential to extend the state of the art in PEMFC modeling by adding a model for the capacitive behavior of the humidifier. Using the advantage of the simulations, the remainder of this work aims to answer the open questions and deepen the interpretation of EPIS features.

3 Methodology

In this chapter, the PEMFC model and the approach of the impedance spectroscopy simulations EIS and EPIS are presented. Additionally, the pressure derivative of the cell voltage on the base of the model equations is described.

3.1 PEMFC model

The description of the PEMFC model is structured as follows. First, the modeling domain is going to be described, followed by the governing model equations. Subsequently, the parameters which are needed for the previous equations are presented. At the end of this subchapter the numerical implementation of the model is described.
The presented PEMFC model is used to reproduce and interpret the experiments of the project partner and therefore parametrized to their experimental setup. The same PEMFC model was used in our joint EPIS publication [28].

3.1.1 Modeling domain

The implemented model dimension is a trade-off between the reduction of modeling and computational efforts on the one hand and the ability of the model to capture the major processes which are relevant for EPIS on the other hand. Modeling of the gas channel dimension proved to be quite important for reproducing the EPIS results, as the pressure oscillation can strongly differ along the gas channel depending on the excitation frequency. Therefore, the PEMFC model used in this work is a pseudo-2D model, whose schematic representation can be seen in Figure 12. A pseudo-2D model connects two 1D subsystems together without solving 2D equations, which is reducing the computational effort of the simulation. One subsystem is the 1D gas transport through the gas channels on a macroscopic scale in x-direction. The second subsystem, sandwiched between the gas channels, considers the 1D transport of mass and charge on a mesoscopic scale in y-direction through the MEA. As the connection of both subsystems is along the gas channel direction, the subsystem of the MEA in y-direction has to be solved for each discretization step of the gas channel in x-direction.
The actual flow field geometry of the bipolar plates used in the experiments consists of 23 parallel serpentine gas channels. The present model simulates only one of the 23 channels, simplified to a straight channel, assuming it to be representative for all gas channels. Although effects such as uneven distribution of reactants in turns of the channels cannot be reproduced by the model, the important change of gas composition along the channel is captured. The 1D transport in the gas channels is assumed to be only gaseous and the occurrence of liquid water is avoided by allowing the gas to be supersaturated. The gas

channel of the anode and cathode are simulated as counterflow. As stated previously, the humidifier of the cathode gas stream has a strong influence on the pressure dynamics along the gas channel. A novelty of the present modeling approach is the consideration of the gas reservoir in the humidifier upstream the cathode channel inlet [28]. This is realized by a 0D model of the gas reservoir, which enables the reproduction of its capacitive behavior to pressure changes.

The MEA consists of five spatially resolved layers, which can be seen in Figure 12. In the middle, separating the anode and cathode is the polymer electrolyte membrane (PEM), which consists of an electrolyte phase. It allows the conductance of protons but acts as an insulator for electrons. The conductivity of the electrolyte is strongly related to its humidification. Therefore, the electrolyte can uptake and transfer water, whereas it is assumed to be impermeable for gases. Attached to each side of the PEM are the catalyst layers (CL), where the electrochemical reactions occur. The CLs are composite electrodes with the coexistence of a gaseous, an electron-conducting and an electrolyte phase. Outside the CLs are the GDLs, in which gas is transported through the pores of an electron-conducting structure. The geometry of the modeling domain is symmetric with respect to the middle axis along the PEM layer. This means that the geometric parameters of the gas channel, i.e. the channel length, width, height and land width; and the geometric parameters of the GDL and CL, i.e. the thickness, tortuosity, porosity, particle and pore diameters and electrode composition, are the same for anode and cathode.

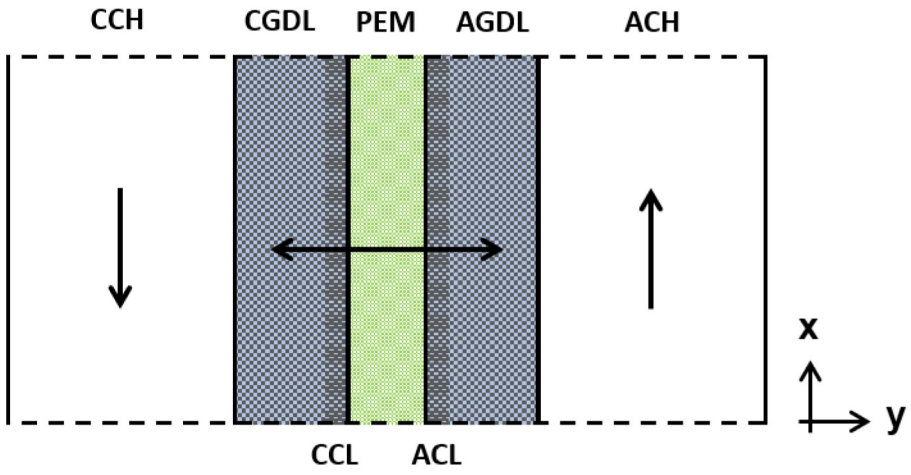

Figure 12: Schematic representation of the pseudo-2D modeling domain (cutout). The mass transport directions are indicated by the arrows. In x-direction, along the cathode and anode gas channel layer (CCH/ACH). In y-direction, through the cathode and anode gas diffusion layer (CGDL/ AGDL), through the cathode and anode catalyst layer (CCL/ ACL), and through the polymer electrolyte membrane (PEM). The figure is extracted from Schiffer et al. [28]

Consistent with the assumption made for the gas channel, it is assumed that gas in the electrodes can be supersaturated. Hence, the occurrence of liquid water is neglected. It

should be stressed here that this assumption limits the validity of the model to only non-condensing conditions, which are given under sufficiently low humidification of the gas inlet streams and/ or sufficiently low current densities. Furthermore, the model is assumed to be isothermal.

3.1.2 Governing equations

In the following subsections the governing equations of the PEMFC model are presented, which describe the electrochemistry, the charge transport and the mass transport. The mass transport is further divided into the gas phase transport through the gas channel in x-direction, the gas transport through the pores of the electrodes in y-direction and the water transport through the electrolyte in y-direction. An additional subsection describes the 0D model of the gas reservoir in the humidifier, which is a boundary condition for the gas transport in the cathode gas channel.

3.1.2.1 Electrochemistry

In this subsection, the thermodynamic and kinetic equations for the electrochemical reactions occurring in the CLs are described. The respective half-cell reactions are at the cathode the oxygen reduction reaction (ORR) and at the anode the hydrogen oxidation reaction (HOR). In the ORR, gaseous oxygen in the pores of the CLs reacts together with hydrogen protons of the electrolyte and electrons of the electron-conducting phase to water which is assumed to evolve dissolved in the electrolyte phase [55,70]. The ORR is defined as

$$\frac{1}{2}\mathrm{O_2(g)} + 2\,\mathrm{H^+(elyt)} + 2\mathrm{e^-(elde)} \rightleftharpoons \mathrm{H_2O(elyt)}\ . \tag{6}$$

In the HOR, hydrogen in the pores of the CL gets oxidized into hydrogen protons in the electrolyte and into electrons in the electron-conducting phase according to

$$\mathrm{H_2(g)} \rightleftharpoons 2\,\mathrm{H^+(elyt)} + 2\mathrm{e^-(elde)}\ . \tag{7}$$

For the sake of simplicity, the half-cell reactions are treated as single-step reactions and it is assumed that the kinetics of the half-cell reaction can be described sufficiently by the use of the following Butler-Volmer (BV) equation [28]

$$i_\mathrm{F}^\mathrm{V} = i_0^\mathrm{V}\left(\exp\left[\frac{\alpha_\mathrm{A}F}{RT}\eta\right] - \exp\left[-\frac{\alpha_\mathrm{C}F}{RT}\eta\right]\right)\ , \tag{8}$$

where i_F^V is the volumetric faradaic current density, i_0^V the volumetric exchange current density, $\alpha_\mathrm{A,C}$ the anodic and cathodic transfer coefficients, T the temperature, η the overpotential, F = 96 485 C mol^{-1} the Faraday constant, and R = 8.314 J mol^{-1} K^{-1} the ideal gas constant. The expression of the faradaic current is volumetric, because the CL is spatially resolved and not treated as an interface. The sign convention for the faradaic current is positive for anodic currents and negative for cathodic currents. The overpotential, being

the driving force for the electrochemical reaction, is defined as the difference between the actual local Galvani potential $\Delta\phi$ and its value at equilibrium $\Delta\phi^{\mathrm{eq}}$ [77]

$$\eta = \Delta\phi - \Delta\phi^{\mathrm{eq}} \ . \tag{9}$$

The introduced sign convention for the faradaic current above leads to a positive overpotential for anodic currents and to a negative overpotential for cathodic currents. The Galvani potential is defined as the difference between the electrode and the electrolyte potential ϕ_{elde}, ϕ_{elyt}, [77]

$$\Delta\phi = \phi_{\mathrm{elde}} - \phi_{\mathrm{elyt}} \ . \tag{10}$$

At equilibrium the Galvani potential is calculated as a function of the local reactant composition by the use of the Nernst equation. The equilibrium Galvani potential of the ORR in the CCL is [55]

$$\Delta\phi^{\mathrm{eq,ORR}} = -\frac{\Delta H_{\mathrm{ORR}} - T\Delta S_{\mathrm{ORR}}}{2F} + \frac{RT}{2F}\ln\left(\sqrt{\frac{p_{\mathrm{O_2}}}{p_{\mathrm{ref}}}}\right) , \tag{11}$$

where ΔH is the reaction enthalpy, ΔS the reaction entropy, $p_{\mathrm{O_2}}$ the partial pressure of gaseous oxygen, and p_{ref} = 101 325 Pa the reference pressure. The other reactants and products of the ORR other than the gaseous oxygen are assumed to have an activity of one and do therefore, not appear in the expression above.

The equilibrium potential of the HOR in the ACL is [55]

$$\Delta\phi^{\mathrm{eq,HOR}} = \frac{\Delta H_{\mathrm{HOR}} - T\Delta S_{\mathrm{HOR}}}{2F} - \frac{RT}{2F}\ln\left(\frac{p_{\mathrm{H_2}}}{p_{\mathrm{ref}}}\right) , \tag{12}$$

where $p_{\mathrm{H_2}}$ is the partial pressure of gaseous hydrogen and p_{ref} = 101 325 Pa. Analogous to the ORR, the products of the HOR are assumed to have an activity of one.

Next to the faradaic current, current can flow due to the charge and discharge of the electric double layer (DL), which evolves at the interface between the electrode and the electrolyte. The charge and discharge are caused by a change in the Galvani potential. The volumetric current density of the DL charge and discharge $i_{\mathrm{DL}}^{\mathrm{V}}$ is calculated as [77]

$$i_{\mathrm{DL}}^{\mathrm{V}} = C_{\mathrm{DL}}^{\mathrm{V}} \frac{\partial\Delta\phi}{\partial t} \ , \tag{13}$$

where, $C_{\mathrm{DL}}^{\mathrm{V}}$ is the volume specific capacitance of the DL, assumed to be independent of the Galvani potential, and t the time.

3.1.2.2 Charge transport

Electric charge is transported in the fuel cell in the form of electrons and protons. The electrons are exchanged between both electrodes by an external circuit, providing electricity as the useful energy. The resistance to the electron transport along the electrodes is assumed to be negligible. This assumption results in a spatially constant potential of the electrodes, expressed by

$$\frac{\partial\phi_{\mathrm{elde}}}{\partial x} = \frac{\partial\phi_{\mathrm{elde}}}{\partial y} = 0 \ . \tag{14}$$

The contact resistances at the electron-conducting interfaces, e.g. between the bipolar plates and the GDL, are respected by the parameter R_{contact} used in Eq. 19.
The transport of protons between both electrodes through the electrolyte causes a significant voltage loss due to its limited proton conductivity. Therefore, the gradient of the electric potential across the electrolyte is considered and modelled by the use of Ohm's law

$$\frac{\partial \phi_{\mathrm{elyt}}}{\partial y} = -\frac{i_{\mathrm{elyt}}}{\sigma_{\mathrm{elyt}}} \ , \tag{15}$$

where i_{elyt} is the ionic current and σ_{elyt} the conductivity of the electrolyte.
The charge continuity equation in the CLs equates the gradient of the ionic current with the sum of the volumetric faradaic current and the volumetric DL current:

$$\frac{\partial i_{\mathrm{elyt}}}{\partial y} = i_{\mathrm{F}}^{\mathrm{V}} + i_{\mathrm{dl}}^{\mathrm{V}} \ . \tag{16}$$

The boundary condition for the charge continuity equation is the ionic current at the interface between the CL and the GDL being zero at both electrodes:

$$i_{\mathrm{elyt}}^{\mathrm{CL|GDL}} = 0 \ . \tag{17}$$

The electric observables on the cell level are the cell voltage V_{cell} and cell current density i_{cell}. The cell current density is calculated by integrating the faradaic and DL current over the cathode CL in both, x- and y-direction according to

$$i_{\mathrm{cell}} = -\frac{1}{L_{\mathrm{CH}}} \int_{x=0}^{L_{\mathrm{CH}}} \int_{y=0}^{L_{\mathrm{CL}}} (i_{\mathrm{F}}^{\mathrm{V}} + i_{\mathrm{dl}}^{\mathrm{V}}) \, \mathrm{d}y \mathrm{d}x \ . \tag{18}$$

The cell voltage is the difference between the electrode potentials of anode and cathode with consideration of the voltage loss due to the contact resistance R_{contact}:

$$V_{\mathrm{cell}} = \phi_{\mathrm{elde,C}} - \phi_{\mathrm{elde,A}} - i_{\mathrm{cell}} R_{\mathrm{contact}} \ . \tag{19}$$

3.1.2.3 Gas-phase transport in the channels

The transport in the subsystem of the gas channel is modelled as gaseous 1D flow in x-direction. The predominant transport mechanism is convection. The exchange with the adjacent subsystem of the MEA is realized via a source term. The transient bulk continuity equation is

$$\frac{\partial \rho}{\partial t} = -\frac{\partial (\rho v)}{\partial x} + \sum_{i=1}^{N} \dot{s}_i \ , \tag{20}$$

where ρ is the gas density, v the velocity, and $\dot{s}_i$ the mass specific source term of species i.
The source term is equal to a conversion of the molar specific boundary flux $J_i^{\mathrm{CH|GDL}}$ of the MEA subsystem at the interface between the GDL and the gas channel. The boundary flux is defined positive in the direction of the GDL. In the experiments, the transport through the GDL in through plane direction is hindered under the rib of the bipolar plate. In the model, the rib is assumed to not interfere with the transport in the GDL. The flux along

the full width of the gas channel w_{CH} and rib w_{rib} gets transferred unhindered into the gas channel, described by the source term

$$\dot{s}_i = -\frac{w_{\mathrm{CH}}+w_{\mathrm{rib}}}{A_{\mathrm{CH}}} j_i^{\mathrm{CH|GDL}} M_{\mathrm{i}} \ , \tag{21}$$

where A_{CH} is the cross section of the gas channel and M_i the molar mass of species i.

The momentum conservation equation for the bulk [78] can be simplified with the assumptions of a 1D flow, neglecting the gravity forces, and assuming that the viscous forces can be described by the wall shear stress, to

$$\frac{\partial \rho v}{\partial t} = -\frac{\partial \rho v^2}{\partial x} - \frac{\partial p}{\partial x} - \frac{P_{\mathrm{CH}}}{A_{\mathrm{CH}}} \tau_{\mathrm{w}} \ , \tag{22}$$

where P_{CH} is the perimeter of the gas channel and τ_w the wall shear stress.

Next to the motion of bulk through convection, the species transport through free molecular diffusion is considered. The species continuity equation is [77,78]

$$\frac{\partial \rho_i}{\partial t} = -\frac{\partial \rho_i v}{\partial x} - \frac{\partial j_i^{\mathrm{diff}}}{\partial x} + \dot{s}_i \ , \tag{23}$$

where j_i^{diff} is the diffusive mass flux of species i relative to the motion of the mass average velocity. The diffusive flux is calculated by the use of an analytical solution of the Maxwell-Stefan equation for multi-component diffusion [78] according to

$$\frac{\partial x_i}{\partial x} = -\sum_{j=1}^{N} \frac{1}{c D_{ij}} \left(\frac{x_j j_i^{\mathrm{diff}}}{M_i} - \frac{x_i j_j^{\mathrm{diff}}}{M_j} \right) \ , \tag{24}$$

where x_i and x_j are the molar fraction of species i and j, c the gas concentration of the gas mixture and D_{ij} the binary diffusion coefficients for diffusion of species i in j. Because the Maxwell-Stefan equations describe a set of linear dependent equations, an additional constraint has to be formulated. As the diffusive fluxes describes the transport of species in relation to the average mass velocity, the sum of the diffusive fluxes of all species has to be zero [78]:

$$\sum_{i=1}^{N} j_i^{\mathrm{diff}} = 0 \ . \tag{25}$$

To solve the previously described gas transport equations, a set of boundary conditions needs to be defined. These are at the gas channel inlet, the velocity $v_{\mathrm{CH}}^{\mathrm{in}}$ and the gas composition in terms of the molar fraction of the species $x_{i,\mathrm{CH}}^{\mathrm{in}}$, and at the gas channel outlet, the pressure $p_{\mathrm{CH}}^{\mathrm{out}}$.

Depending on the operation conditions, the boundary conditions of the inlet quantities are not given directly but rather calculated as a function of extrapolated inlet quantities. The gas composition at the gas channel inlet for example can be expressed indirectly by the molar fraction of the dry gas $x_{i,\mathrm{CH}}^{\mathrm{in,dry}}$ together with a given relative humidity $\varphi_{\mathrm{CH}}^{\mathrm{in}}$. The actual gas composition becomes then a function of the inlet pressure. At the cathode with the species oxygen, nitrogen and water the gas composition is then given by

$$x_{\mathrm{H_2O,CCH}}^{\mathrm{in}} = \varphi_{\mathrm{CCH}}^{\mathrm{in}} \frac{p_{\mathrm{H_2O}}^{\mathrm{sat}}}{p_{\mathrm{CCH}}^{\mathrm{in}}} \ , \tag{26}$$

$$x_{\mathrm{O_2,CCH}}^{\mathrm{in}} = x_{\mathrm{O_2,CCH}}^{\mathrm{in,dry}}\left(1 - x_{\mathrm{H_2O,CCH}}^{\mathrm{in}}\right) , \tag{27}$$

$$x_{\mathrm{N_2,CCH}}^{\mathrm{in}} = x_{\mathrm{N_2,CCH}}^{\mathrm{in,dry}}\left(1 - x_{\mathrm{H_2O,CCH}}^{\mathrm{in}}\right) . \tag{28}$$

At the anode with the species hydrogen and water the gas composition is given by

$$x_{\mathrm{H_2O,ACH}}^{\mathrm{in}} = \varphi_{\mathrm{ACH}}^{\mathrm{in}} \frac{p_{\mathrm{H_2O}}^{\mathrm{sat}}}{p_{\mathrm{ACH}}^{\mathrm{in}}} , \tag{29}$$

$$x_{\mathrm{H_2,ACH}}^{\mathrm{in}} = 1 - x_{\mathrm{H_2O,ACH}}^{\mathrm{in}} . \tag{30}$$

The boundary condition of the gas channel inlet velocity is calculated in different ways for the anode and cathode. This is due to the fact that upstream the cathode gas channel, the gas feed is passing through the humidifier, whose gas volume is affecting the gas flow rate into the gas channel. The anode gas feed is not flowing through a humidifier before entering the gas channel. Therefore, the inlet velocity at the anode can be calculated relatively simple according to

$$v_{\mathrm{ACH}}^{\mathrm{in}} = \frac{\dot{m}_{\mathrm{feed,A}}}{\rho_{\mathrm{ACH}}^{\mathrm{in}} A_{\mathrm{CH}}} , \tag{31}$$

where $\dot{m}_{\mathrm{feed}}$ is the mass flow rate of the gas feed. Depending on the simulated operating conditions, the gas feed can be set directly, or calculated based on a fixed stoichiometry of reactant i according to

$$\dot{m}_{\mathrm{feed}} = \frac{\lambda_i}{x_{i,\mathrm{CH}}^{\mathrm{in}}} \frac{i_{\mathrm{cell}} A_{\mathrm{FC}}}{z_i F n_{\mathrm{CH}}} \bar{M}_{\mathrm{CH}}^{\mathrm{in}} , \tag{32}$$

where λ_i is the stoichiometry of the reactant i, A_{FC} = 100 cm^2 the fuel cell area, z_i the number of transferred electrons per mol of reactant i, n_{CH} = 23 the number of channels, and $\bar{M}_{\mathrm{CH}}^{\mathrm{in}}$ the average molar mass of the gas mixture at the gas channel inlet.

The calculation of the gas channel inlet velocity at the cathode $v_{\mathrm{CCH}}^{\mathrm{in}}$, by incorporating the capacitive behavior of the gas volume inside the humidifier, is rather complex compared to its counterpart at the anode. Therefore, its calculation is described more detailed in the subsection 3.1.2.6.

3.1.2.4 Gas-phase transport in porous layers

The gas transport in the subsystem MEA occurs in the porous layers GDL and CL. The bulk is moving through the pores according to the pressure gradient by convection, modeled by the use of Darcy's law. The other considered transport mechanism is diffusion, in which the gas of each species moves due to its concentration gradient. The species continuity equation is

$$\frac{\partial(\varepsilon c_i)}{\partial t} = -\frac{\partial J^{\mathrm{conv}} x_i}{\partial y} - \frac{\partial J_i^{\mathrm{diff}}}{\partial y} + \dot{S}_i , \tag{33}$$

where ε is the porosity, J^{conv} the molar flux of the bulk due to convection, J_i^{diff} the molar flux of species i due to diffusion, and $\dot{S}_i$ a molar specific source term of species i. The source term is needed in the CL to account for the consumption or production of species

due to the electrochemical reactions, and in case of water, to account for the absorption or desorption of water into or out of the electrolyte.

The convective transport of the gas bulk phase through the pores is calculated with the use of Darcy's law [78]. With neglecting the gravity forces, the flow velocity can be expressed as

$$v = -\frac{\kappa}{\mu}\frac{\partial p}{\partial y} \ , \tag{34}$$

where κ is the permeability of the porous electrode and μ the dynamic viscosity of the gas mixture. The flow velocity is converted to the molar flux by multiplication with the gas concentration:

$$J^{\mathrm{conv}} = cv \ . \tag{35}$$

The diffusive flux in the porous layers is calculated by the use of the Maxwell-Stefan equations [78], similar to the transport in the gas channels according to

$$\frac{\partial x_i}{\partial y} = -\sum_{j=1}^{N} \frac{1}{cD_{ij}^{\mathrm{eff}}}\left(x_j J_i^{\mathrm{diff}} - x_i J_j^{\mathrm{diff}}\right) \ , \tag{36}$$

where D_{ij}^{eff} are effective binary diffusion coefficients, whose determination is explained subsequently. The set of linear dependent equations obtained by the Maxwell-Stefan equations, are extended by the constraint that the sum of molar diffusive fluxes is zero [78]. In other words, the diffusive fluxes describe the net transport relative to the molar average velocity which is defined by

$$\sum_{i=1}^{N} J_i^{\mathrm{diff}} = 0 \ . \tag{37}$$

The effective binary diffusion coefficients are used to account for free molecular and Knudson diffusion, realized by the use of Bosanquet's formula. The symmetry of the effective binary diffusive coefficients is ensured by calculating averaged diffusion coefficients [77] according to

$$D_{ij}^{\mathrm{eff}} = D_{ji}^{\mathrm{eff}} = \frac{\epsilon}{\tau^2}\frac{1}{2}\left(\frac{1}{1/D_i^{\mathrm{K}}+1/D_{ij}} + \frac{1}{1/D_j^{\mathrm{K}}+1/D_{ji}}\right) \ , \tag{38}$$

where τ is the tortuosity of the porous layer and D_i^{K} the Knudsen diffusion coefficient of species i. Knudsen diffusion is used in porous media with small pores, in which the collision of a molecule with the wall becomes more likely than the collision with another molecule. The coefficient is therefore a function of the pore size of the porous layer [78] given by

$$D_i^{\mathrm{K}} = \frac{2}{3} r_{\mathrm{pore}} \left(\frac{8}{\pi}\frac{RT}{M_i}\right)^{\frac{1}{2}} \ . \tag{39}$$

As stated before, in the CLs species can enter or leave the gas phase, which is considered by the molar specific source term in the species continuity equation. The consumption of gaseous reactants is calculated based on the reaction stoichiometry and the sign convention of the Faradaic current, which is negative for a cathodic and positive for an anodic current. In the anode CL, hydrogen is consumed by the HOR according to

$$\dot{S}_{\mathrm{H_2}} = -\frac{i_{\mathrm{F}}^{\mathrm{V}}}{2F} \ . \tag{40}$$

The consumption of oxygen due to the ORR is

$$\dot{S}_{\mathrm{O_2}} = \frac{i_{\mathrm{F}}^{\mathrm{V}}}{4F} \ , \tag{41}$$

note that the production of water due to the ORR is not considered here, as water is assumed to be produced in the dissolved form in the electrolyte. Gaseous water can leave or enter the gas phase due to absorption or desorption into or out of the electrolyte. The exchange rate of water between the gas phase and electrolyte phase is dependent on the saturation of the electrolyte [79,80] and defined as

$$\dot{S}_{\mathrm{H_2O}} = -\frac{k_{\mathrm{a,d}}}{L_{\mathrm{CL}} V_{\mathrm{m}}} \left(\lambda_{\mathrm{eq}} - \lambda\right) \ , \tag{42}$$

where $k_{\mathrm{a,d}}$ is the absorption and desorption rate constant, L_{CL} the thickness of the CL, V_{m} the volume of the electrolyte per sulfonic acid sides, λ the actual water content of the electrolyte, and λ_{eq} the water content of the electrolyte at equilibrium. The volume of the electrolyte per sulfonic acid sides is calculated as

$$V_{\mathrm{m}} = \frac{\mathrm{EW}}{\rho_{\mathrm{elyt}}^{\mathrm{dry}}} \ , \tag{43}$$

where EW is the equivalent weight, defined as the weight per sulfonic acid sites, and $\rho_{\mathrm{elyt}}^{\mathrm{dry}}$ the density of the dry electrolyte.

To solve the set of differential equations, describing the gas transport in the porous layers, the following boundary conditions are defined. As the PEM is assumed to be impermeable for gases, the convective flux of the bulk, as well as the diffusive flux of each species is set to zero at the interface between the CL and the PEM:

$$J^{\mathrm{conv,CL|PEM}} = 0 \ , \tag{44}$$

$$J_i^{\mathrm{diff,CL|PEM}} = 0 \ . \tag{45}$$

Furthermore, the total pressure at the interface between the GDL and the gas channel is set equal to the total pressure of the adjacent gas channel compartment:

$$p^{\mathrm{CH|GDL}} = p_{\mathrm{CH}} \ . \tag{46}$$

Analogous to the total pressure, the gas concentration of species i as set equal at the same locations:

$$c_i^{\mathrm{CH|GDL}} = c_{i,\mathrm{CH}} \ . \tag{47}$$

3.1.2.5 Water transport in electrolyte

Water transport in the electrolyte of the CL and the PEM is assumed to occur in the dissolved form. The flux of dissolved water is modelled based on the work of Springer et al. [45]. It considers two transport mechanisms, which are diffusion and electro-osmotic drag. The continuity equation for dissolved water in the electrolyte is

$$\frac{\partial \lambda}{\partial t} \frac{\epsilon_{\mathrm{elyt}}}{V_{\mathrm{m}}} = -\frac{\partial J_\lambda^{\mathrm{diff}}}{\partial y} - \frac{\partial J_\lambda^{\mathrm{drag}}}{\partial y} + \dot{S}_\lambda \ , \tag{48}$$

where ϵ_{elyt} is the volume fraction of electrolyte, $J_\lambda^{\mathrm{diff}}$ the molar flux of dissolved water due to diffusion, $J_\lambda^{\mathrm{drag}}$ the molar flux of dissolved water due to electro-osmotic drag, and $\dot{S}_\lambda$ the molar specific source term of dissolved water due to water production or ab- or desorption.

The water content of the electrolyte is defined as the molar amount of water per molar amount of sulfonic acid sides of the electrolyte:

$$\lambda = \frac{n_{\mathrm{H_2O}}}{n_{\mathrm{SO_3^-}}} \ . \tag{49}$$

The diffusive flux is proportional to the gradient of water content and formulated analogous to Fick's first law according to

$$J_\lambda^{\mathrm{diff}} = -\frac{D_\lambda}{V_{\mathrm{m}}}\frac{\partial \lambda}{\partial y} \ , \tag{50}$$

where D_λ is the water diffusivity in the electrolyte.

The water flux due to electro-osmotic drag is proportional to the ionic current and expressed as

$$J_\lambda^{\mathrm{drag}} = \frac{\xi}{F} i_{\mathrm{elyt}} \ , \tag{51}$$

where ξ describes the number of water molecules dragged per proton.

In the CLs, water can leave or enter the electrolyte due to desorption or absorption depending on the electrolyte water saturation. In the cathode CL water gets produced in the dissolved form in the electrolyte due to the ORR. The source term of dissolved water in the electrolyte is defined as

$$\dot{S}_\lambda = \begin{cases} \frac{k_{\mathrm{a,d}}}{L_{\mathrm{CL}} V_{\mathrm{m}}}(\lambda^{\mathrm{eq}} - \lambda) - \frac{i_{\mathrm{F}}^{\mathrm{V}}}{2F} & , \mathrm{CCL} \\ \frac{k_{\mathrm{a,d}}}{L_{\mathrm{CL}} V_{\mathrm{m}}}(\lambda^{\mathrm{eq}} - \lambda) & , \mathrm{ACL} \end{cases} \ . \tag{52}$$

In the layer PEM the source term is zero, $\dot{S}_\lambda = 0$.

To solve the differential equation for the water transport in the electrolyte, the following boundary condition is defined. As the electrolyte is only present inside the CL and the PEM, the water flux through the electrolyte has to be zero at the interface between the CL and the GDL:

$$J_\lambda^{\mathrm{GDL|CL}} = 0 \ . \tag{53}$$

3.1.2.6 Humidifier

Gas humidifiers are used in PEMFCs to humidify the gas inlet stream and thus ensure sufficient hydration of the electrolyte. In the present model, only the cathode gas feed is humidified. The anode gas feed is assumed as dry, with a remaining relative humidity of $\varphi = 0.05$. Figure 13 shows the schematic representation of a gas humidifier. Dry gas is fed from the bottom into the humidifier. It passes the water, regulated at the desired humidifier temperature, through bubbles, and leaves at the top as saturated gas. Above the

water, the humidifier contains a certain gas volume, which acts as a gas reservoir. In case the pressure changes, the amount of gas inside the humidifier also changes due to the change in the gas density. With a constant flow rate of gas feed at the bottom, this results in a change of the flow rate of humidified gas out of the humidifier. To reproduce this important effect in the simulations, a 0D model for the gas volume in the humidifier is included in the present PEMFC model, which is explained in the following.

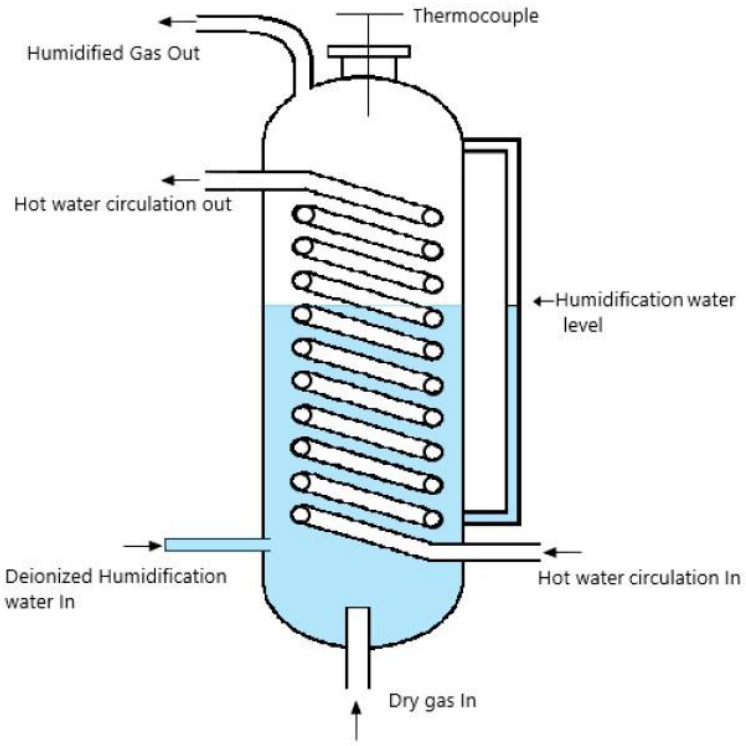

Figure 13: Schematic representation of a gas humidifier. The figure is extracted from Shirsath [81].

As the PEMFC model simulates only one of the 23 parallel serpentine channels, the actual gas volume inside the humidifier of the experimental setup V_{hum} = 850 ml has to be adjusted by the number of channels n_{CH} = 23, resulting in the following mass conservation equation around the gas reservoir of the humidifier

$$\frac{V_{\mathrm{hum}}}{n_{\mathrm{CH}}}\frac{\partial \rho_{\mathrm{hum}}}{\partial t} = \dot{m}_{\mathrm{feed}} - \dot{m}_{\mathrm{CH}}^{\mathrm{in}} \ , \tag{54}$$

where ρ_{hum} is the gas density inside the gas reservoir of the humidifier, $\dot{m}_{\mathrm{feed}}$ is the mass flow of the humidified gas into the gas reservoir calculated according to Eq. 32, and $\dot{m}_{\mathrm{CH}}^{\mathrm{in}}$ the gas stream out of the gas reservoir and into the gas channel. The volume of the gas pipe between humidifier and gas channel inlet is assumed to be negligible compared to the gas reservoir inside the humidifier. Therefore, it is assumed that the mass flow rate out of the humidifier is equal the mass flow rate into the gas channel which is given as

$$\dot{m}_{\mathrm{CH}}^{\mathrm{in}} = v_{\mathrm{CH}}^{\mathrm{in}} A_{\mathrm{CH}} \rho_{\mathrm{CH}}^{\mathrm{in}} \ . \tag{55}$$

Furthermore, by assuming a constant temperature and pressure from the humidifier outlet to the gas channel inlet, also the density can be assumed as constant:

$$\rho_{\mathrm{hum}} = \rho_{\mathrm{CH}}^{\mathrm{in}} \ . \tag{56}$$

The combination of the equations above leads to the following expression for the cathode inlet velocity, which is needed as the boundary condition for the gas transport in the gas channel:

$$v_{\mathrm{CH}}^{\mathrm{in}} = \frac{\left(\dot{m}_{\mathrm{feed}} - \frac{V_{\mathrm{hum}} \partial \rho_{\mathrm{CH}}^{\mathrm{in}}}{n_{\mathrm{CH}} \quad \partial t}\right)}{A_{\mathrm{ch}} \rho_{\mathrm{CH}}^{\mathrm{in}}} \ . \tag{57}$$

3.1.3 Parametrization

This section describes the determination of the parameters used in the governing equations. It is subdivided into the parameters of electrochemistry, charge transport, mass transport, fuel cell structure, and operating conditions. As described previously, the PEMFC model was parametrized to the experimental setup of the project partner [14–17,28,81].

3.1.3.1 Electrochemistry

To calculate the Galvani potential of both half-cell reactions at equilibrium, its thermodynamic properties are needed. The reaction enthalpy and entropy of the ORR and the HOR are given in Table 1.

Table 1: Thermodynamic properties of the half-cell reactions ORR and HOR. The reaction enthalpies are taken from Chase [82], the reaction entropies from Lampinen and Fomino [83]

Reaction	ΔH / kJ mol^{-1}	ΔS / J mol^{-1} K^{-1}
ORR	-285.83	-163.3
HOR	0.00	0.1

The required kinetic parameters for both half-cell reactions are the volumetric exchange current density and the transfer coefficients. The exchange current density of the ORR is calculated by using a pressure and temperature dependent expression based on [37], while the exchange current density at reference conditions was fitted to the experiments of the project partner. This results in the following expression

$$i_0^{\mathrm{V}} = 1.55 \cdot 10^6 \ \mathrm{A\,m^{-3}} \left(\frac{p_{\mathrm{O_2}}}{p_{\mathrm{ref}}}\right)^{0.54} \exp\left(\frac{67 \ \mathrm{kJ\,mol^{-1}}}{R}\left(\frac{1}{T_{\mathrm{ref}}} - \frac{1}{T}\right)\right) , \tag{58}$$

where T_{ref} = 353.15 K is the reference temperature and p_{ref} = 101 325 Pa the reference pressure. The reference values are also used in the following expressions, if not

mentioned explicitly to be different. The pressure dependence of the exchange current density ensures the change of reaction kinetics during the pressure excitation.
The cathodic transfer coefficient of the ORR was also fitted to the previously mentioned experiments $\alpha_C = 0.566$. The anodic transfer coefficient α_A is calculated, based on the relationship between anodic and cathodic transfer coefficient of the BV equation used in reference [55] $\alpha_A = 2 - \alpha_C = 1.434$.
The exchange current density of the HOR is calculated based on the kinetics measured by Durst et al. [39], in combination with a platinum (Pt) loading of the anode CL used in [55] which leads to:

$$i_0^V = 2.7 \cdot 10^3 \text{ A m}_{Pt}^{-2} \cdot 10^7 \text{ m}_{Pt}^2 \text{ m}^{-3} \exp\left(\frac{16 \text{ kJ mol}^{-1}}{R}\left(\frac{1}{T_{ref}} - \frac{1}{T}\right)\right) . \quad (59)$$

Other than the ORR the reaction kinetics of the HOR are independent of the gas composition in the CL. The transfer anodic and cathodic transfer coefficient of the HOR are defined as $\alpha_A = \alpha_C = 1$ [55].
To calculate the DL charge and discharge current in the anode and cathode CL the volume specific capacitance C_{DL}^V is needed. The capacitance at the cathode was fitted to the subsequently shown EIS results (see Chapter 4.2). The capacitance at the anode is assumed to have the same value which is

$$C_{DL}^V = 4.1 \cdot 10^7 \text{F m}^{-3} .$$

3.1.3.2 Charge transport

The contact resistance, accounting for the resistances at the electron-conducting interfaces, such as between the GDL and the bipolar plate, was fitted by matching experimental EIS results (see Chapter 4.2) according to

$$R_{contact} = 6.3 \cdot 10^{-2} \text{ Ω cm}^2 .$$

The proton conductivity is modelled as a function of the water content according to Springer et al. [45], who fitted an expression for their experimentally measured conductivities at 30 °C. They derived the activation energy of the temperature correction from another experiment conducted at 80 °C with a fully hydrated electrolyte, which they assumed to be valid for all water contents. The Bruggemann correction of the conductivity is used to account for the volume fraction of electrolyte in the CL [84]. This results in the following definition of the proton conductivity

$$\sigma_{elyt} = \epsilon_{elyt}^{1.5}(0.5139\lambda - 0.326) \text{ S m}^{-1} \exp\left(1268\left(\frac{1}{303 \text{ K}} - \frac{1}{T}\right)\right) . \quad (60)$$

According to the approach of Springer et al., the conductivity is assumed to not decrease below a value of $\sigma_{elyt}(\lambda = 1)$ for a water content $\lambda < 1$.

3.1.3.3 Mass transport

In the subsystem of the gas channels, the wall shear stress is used in the momentum conservation equation and needs to be parametrized. The wall shear stress is a function of the velocity with a term of linear and quadratic dependence defined as

$$\tau_{\mathrm{w}} = \frac{1}{8}\frac{P_{\mathrm{CH}}}{A_{\mathrm{CH}}}\mu v f_1 + \frac{1}{2}\rho v^2 f_2 \ . \tag{61}$$

where f_1 and f_2 are fitted friction factors. The linear term describes the pressure loss for a laminar flow due to viscous forces, whereas the quadratic term accounts for turbulent pressure losses due to additional flow hindrance, such as turns of the serpentine flow field. The friction factors are fitted to match experimental pressure loss measured at 20 °C and 50 °C (see Chapter 4.3). The obtained values are:

$$f_1 = 18.5 \ ,$$
$$f_2 = 0.021 \ .$$

The binary diffusion coefficients D_{ij}, needed for the calculation of the diffusive flux in the gas channel and the MEA, is taken from Fuller et al. [85].

In the subsystem of the MEA, the permeability of the porous media is needed to calculate the convective gas transport in the electrodes. The expression of the permeability is called the Kozeny-Carman equation and is a function of the porosity , the tortuosity, and the particle diameter d_{particle} [86]

$$\kappa = \frac{\epsilon^3 d_{\mathrm{particle}}^2}{72\tau(1-\epsilon)^2} \ . \tag{62}$$

To describe the transport of dissolved water inside the electrolyte, the diffusivity of dissolved water inside the electrolyte and the electro-osmotic drag coefficient need to be defined. The diffusivity is given by an expression derived from Motupally et al. [87], who fitted the diffusivity expression to measured values of Zawodzinski et al. [88]. As the experiments of Zawodzinski et al. were conducted at 30 °C, Motupally et al. extended the equation by a temperature correction from Yeo and Eisenberg [89]. Again the Bruggemann correction is used to account for the volume fraction of electrolyte in the CL [84]. This results in the following definition of the water diffusivity

$$D_\lambda = \begin{cases} 3.1\cdot10^{-7}\ \mathrm{m^2\ s^{-1}}\cdot\epsilon_{\mathrm{elyt}}^{1.5}\,\lambda(-1+\exp(0.28\lambda))\exp\left(-\frac{2436\ \mathrm{K}}{T}\right) & \text{,for } \lambda\leq 3 \\ 4.17\cdot10^{-8}\ \mathrm{m^2\ s^{-1}}\cdot\epsilon_{\mathrm{elyt}}^{1.5}\,\lambda(1+161\cdot\exp(-\lambda))\exp\left(-\frac{2436\ \mathrm{K}}{T}\right) & \text{,for } \lambda>3 \end{cases} \ . \tag{63}$$

The number of dragged water molecules per proton is modelled by the approach of Springer et al. [45]. They obtained a linear dependence of the electro-osmotic drag coefficient from the water content according to

$$\xi = \frac{2.5\lambda}{22} \ . \tag{64}$$

To quantify the exchange rate of water between the dissolved form in the electrolyte and the gas phase, the absorption and desorption coefficients are needed. Both coefficients

are assumed to increase proportionally to the volume fraction of water in the electrolyte f [79] according to

$$k_{\mathrm{a,d}} = a_{\mathrm{a,d}}\, f \exp\left[\frac{20\ \mathrm{kJ\ mol^{-1}}}{R}\left(\frac{1}{T_{\mathrm{ref}}} - \frac{1}{T}\right)\right] , \tag{65}$$

where the kinetic absorption and desorption parameters are $a_{\mathrm{a}} = 3.53 \cdot 10^{-5}$ m s^{-1} and $a_{\mathrm{d}} = 1.42 \cdot 10^{-4}$.

The volume fraction of water in the electrolyte used to calculate the absorption and desorption coefficients is calculated by

$$f = \frac{\lambda V_{\mathrm{w}}}{\lambda V_{\mathrm{w}} + V_{\mathrm{m}}} , \tag{66}$$

where $V_{\mathrm{w}} = M_{\mathrm{H_2O}} / \rho_{\mathrm{H_2O}}$ is the molar volume of water, with $M_{\mathrm{H_2O}} = 18$ g mol^{-1} and $\rho_{\mathrm{H_2O}} = 978$ kg m^{-3}.

Another parameter, needed to calculate the absorption or desorption rate of water into or out of the electrolyte, is the saturated water content of the electrolyte, called the equilibrium water content. The used polynomial is based on the expression of Springer et al. [45], who fitted it to experiments obtained at 30 °C. Similar to Springer et al, who assumed the expression to be valid up to 80 °C, the expression is used at an operating temperature of 55 °C. In case of supersaturation, for a water activity $a > 1$, the water content is modelled to increase linearly up to a value of 16.8 and remains constant for activities above:

$$\lambda^{\mathrm{eq}} = \begin{cases} 0.043 + 17.81a - 39.85a^2 + 36.0a^3 & \text{,for } a \leq 1 \\ 14 + 1.4(a-1) & \text{,for } 1 < a \leq 3 \end{cases} . \tag{67}$$

The activity of water is calculated as

$$a = \frac{p_{\mathrm{H_2O}}}{p^{\mathrm{sat}}_{\mathrm{H_2O}}(T)} . \tag{68}$$

The saturation water pressure is calculated with the Arden Buck equation [90] according to

$$p^{\mathrm{sat}}_{\mathrm{H_2O}}(T) = 611.21\ \mathrm{Pa} \cdot \exp\left(\frac{\left(18.678 - \frac{T}{234.5\ ^\circ\mathrm{C}}\right)T}{T + 257.14\ ^\circ\mathrm{C}}\right) , \tag{69}$$

where the temperature T has to be inserted in °C, instead of K as done throughout the remaining work.

3.1.3.4 Structural parameters

The structural parameters of the MEA are given in Table 2 and the structural parameters of the gas channel in Table 3. The parameters are not differentiated for the anode and cathode, because the model is assumed to be symmetric with respect to the middle axis along the PEM layer.

Table 2: Structural parameters of the MEA. The porosity of the CL and the volume fraction of the electrolyte in the CL are taken from Vetter and Schumacher [55]. The remaining parameters are taken from the experimental setup.

Parameter MEA	Value	Unit
Thickness L {GDL, CL, PEM}	{212.15, 10, 50}	µm
Porosity ϵ {GDL, CL}	{0.77, 0.4}	–
Tortuosity τ {GDL, CL}	{1.26, 1.26}	–
Volume fraction electrolyte ϵ_{elyt} {CL, PEM}	{0.3, 1.0}	–
Particle diameter d_{particle} {GDL, CL}	{0.54, 0.54}	µm
Pore radius r_{pore} {GDL, CL}	{0.27, 0.27}	µm

Table 3: Structural parameters of the gas channel. The parameters are taken from the experimental setup.

Parameter Gas channel	Value	Unit
Channel length L_{CH}	0.304	m
Channel cross-section area A_{CH}	0.308	mm^2
Channel width w_{CH}	0.7	mm
Channel rib width w_{rib}	0.73	mm
Channel wetted perimeter P_{CH}	2.28	mm

3.1.3.5 Operating conditions

Unless stated otherwise, the default operating conditions listed in Table 4 are used. The average outlet pressure at the anode and cathode is the same, whereas the dynamic pressure excitation only applies to the cathode. The relative humidity at the cathode is constant, because the gas leaves the humidifier with an adjusted relative humidity of 55%. At the anode, the gas feed is not humidified, but a constant gas humidity of 5% is assumed to remain.

In addition to the simulations using the default operating conditions, there are simulations with a different outlet pressure, relative humidity, inlet mixture and stoichiometry. Furthermore, there are simulations in which the condition of the gas inlet is defined by other parameters than the one given in Table 4. Instead of fixing the inlet gas composition of the dry gas for a constant relative humidity, the inlet gas composition of all species is set constant, by allowing the relative humidity to change. Additionally, instead of keeping the stoichiometry of the reactants constant, the mass flow rate at the inlet is set constant.

Table 4: Default operating conditions of the PEMFC model.

Operation conditions	Value	Unit
Temperature T	328.15	K
Outlet pressure $p_{\mathrm{CH}}^{\mathrm{out}}$	116 325	Pa
Inlet relative humidity $\varphi_{\mathrm{ACH}}^{\mathrm{in}}, \varphi_{\mathrm{CCH}}^{\mathrm{in}}$	0.05, 0.55	–
Inlet mixture (dry) anode $x_{\mathrm{H_2}}$	1.00	–
Inlet mixture (dry) cathode $x_{\mathrm{O_2}}, x_{\mathrm{N_2}}$	0.21, 0.79	–
Inlet stoichiometry $\lambda_{\mathrm{H_2}}, \lambda_{\mathrm{O_2}}$	1.2, 2.5	–

3.1.4 Numerical implementation

The PEMFC model described above was implemented using the in-house software package DENIS (Detailed Electrochemistry and Numerical Impedance Simulation) [24,77], written in the programming language C/C++. The set of equations is a combination of partial differential equations (PDE) and algebraic equations. The PDEs were approximated using the finite volume method. The discretization mesh is a tradeoff between the accuracy of the solution and computational efforts. In the subsystem of the gas channel in x-direction, the compartment size is in the magnitude of a centimeter, identical for the anode and cathode. The vector describing the compartment sizes in x-direction is

$$\Delta x_{\mathrm{CH}} = [1 \times 0.1, 3 \times 10.1, 1 \times 0.1]\ \mathrm{cm}\ .$$

where the vector has to be read as [“number of compartments” “times” “compartment size”, …].

In the subsystem of the MEA the discretization mesh is in the magnitude of a micrometer, resulting in the following vector for the cathode GDL

$$\Delta y_{\mathrm{CGDL}} = [3 \times 70.6, 1 \times 0.7]\ \mu\mathrm{m}\ .$$

the cathode CL

$$\Delta y_{\mathrm{CCL}} = [1 \times 1.0, 3 \times 10.0, 1 \times 1.0, 1 \times 0.5]\ \mu\mathrm{m}\ .$$

and the PEM

$$\Delta y_{\mathrm{PEM}} = [1 \times 0.9, 1 \times 2.6, 5 \times 8.6, 1 \times 2.6, 1 \times 0.9]\ \mu\mathrm{m}\ .$$

The vectors of the anode GDL and CL are the flipped version of the corresponding cathode layer vector as the MEA is assumed to be symmetric with respect to the PEM. The above shown discretization is used throughout the present work, if not stated otherwise.

The resulting system of algebraic-differential equations was solved by using the solver LIMEX (version 2.4), which is an adaptive, semi-implicit time-step solver [91,92]. The simulations were carried out through MATLAB (version R2019a), which executes the simulation package DENIS. Furthermore, MATLAB was used for post-processing and visualization of the results.

The EPIS simulation of a full spectrum in the frequency range between 1 mHz - 100 Hz with four frequencies per decade has a computational time of about 1.5 h on an Intel Core i7-6700 processor with 3.4 GHz and 32 GB memory using the full model setup with an absolute and relative error tolerance of 10^{-5}.

3.2 Impedance spectroscopy simulations

In this subchapter, the methodologies for the two impedance spectroscopy simulations EIS and EPIS are going to be presented. Both approaches analyze the cell response to a specific cell excitation in the frequency domain, with the difference in the type of cell excitation and cell response. First, the simulative approach of EIS is described, followed by the description of the EPIS simulations.

3.2.1 EIS

In EIS, the dynamic relationship between the cell voltage and the cell current is analyzed. It is possible to either excite the cell voltage harmonically and measure the cell current response or vice versa [93]. The transfer function between both quantities, that is the electrochemical impedance, is calculated as the relationship between the Fourier-transformed voltage response and current excitation at each analyzed frequency according to

$$Z_{V/i}(\omega) = \frac{\mathcal{F}\{\Delta V_{\mathrm{cell}}(t)\}}{\mathcal{F}\{\Delta i_{\mathrm{cell}}(t)\}} \,. \tag{70}$$

The EIS experiments of the project partner, to which the present model is parametrized, were performed with the excitation of the current density and measurement of the cell voltage response. The cell current was excited with an amplitude of 10% of the actual current density. The simulative approach of EIS is different in terms of the excitation of the current density. Due to its advantage of faster simulations, the approach of applying one rapid step excitation [94] is used instead of applying multiple harmonic excitations. The same approach was applied in [28]: The cell current was increased by 10% of the actual current density within 0.1 µs and the resulting cell voltage response was measured. Afterwards, the impedance was calculated according to Eq. 70.

The experimental EIS measurements were made for constant gas feed rates, which were fixed according to the desired stoichiometry at the anode and cathode, respectively. To reproduce the experiments, the following procedure is applied for the simulations. First, a steady-state simulation with the desired cell current is conducted under stoichiometric control. The obtained mass flow rate is then used as an input for the further simulations under mass flow control. Before starting the actual step excitation, a combination of a steady-state simulation followed by a transient simulation for a time period of 1000 s, is performed. Only after these preparative steps, the actual step excitation is simulated.

3.2.2 EPIS

In the present EPIS study, the dynamic relationship between the cathode outlet pressure excitation and the cell voltage response is analyzed under galvanostatic control. The analyzed transfer function $Z_{V/p}$, sometimes referred as pressure impedance, is calculated as the relationship between the Fourier transform of both quantities according to Eq. 2 at each analyzed frequency.

The experimental approach of EPIS by Shirsath et al. is described and reviewed in Chapter 2.2.2 above. The authors varied the pressure excitation amplitude due to conflicting requirements in the range between 200–2500 Pa, depending on the excitation frequency. The requirement defining the lower limit is that the amplitude still induces a detectable cell voltage response, which can be distinguished from the noisy fluctuations of the voltage signal. Among others, the requirement defining the upper limit is the linearity between the cell excitation and cell response. For the sake of simplicity, the EPIS simulations are conducted with a constant excitation amplitude of $\Delta p_{\mathrm{CH}}^{\mathrm{out}}$ = 100 Pa, as the signal distortion of the simulations is far smaller compared to the experiments.

Similar to the EIS experiments, the EPIS experiments were conducted with a constant mass flow rate according to its stoichiometric control at steady state. Therefore, the preparative steps for the EIS simulations are also applied for the EPIS simulations. After these preparative steps, the cathode outlet pressure is excited by modifying the boundary condition of the cathode outlet pressure according to

$$p_{\mathrm{CCH}}^{\mathrm{out}}(t) = \bar{p}_{\mathrm{CCH}}^{\mathrm{out}} + \Delta p_{\mathrm{CCH}}^{\mathrm{out}} \sin(\omega t) \ . \tag{71}$$

where $\bar{p}_{\mathrm{CCH}}^{\mathrm{out}}$ is the average outlet pressure equal to the default value given in Table 4 and $\omega = 2\pi f$ the angular frequency, with the excitation frequency f. The pressure excitation at the cathode channel outlet is simulated repeatedly until the change in magnitude of $Z_{V/p}$ between the present and the previous sine wave is less than 1%. Hence, at least two pressure excitation waves are simulated for each frequency. If the accuracy of 1% cannot be reached, which occurs occasionally at the highest frequencies, a maximum number of twenty sine waves is used. Furthermore, to ensure the accuracy of the simulations, a number of thousand timesteps per sine wave are simulated.

As pointed out before, the additional value of the simulations compared to the experiments is the analysis of internal states, which are difficult to access in the experiments. To analyze the internal states in the frequency domain, defining new transfer functions between the oscillation of the quantity of interest and the outlet pressure oscillation proved most practical. To this end, the enumerator of the transfer function needs to be replaced by the Fourier transform of the quantity of interest, as was done with the inlet pressure response in Eq. 3.

The cell voltage, being spatially independent, is the integrated consequence of local states of the fuel cell. Therefore, in the context of the total pressure response, the average value

along the gas channel is analyzed in addition to the value at the inlet. The transfer function between the average pressure oscillation along the channel and the pressure excitation is then

$$Z_{p(\mathrm{avg})/p}(\omega) = \frac{\mathcal{F}\{\Delta\bar{p}_{\mathrm{CCH}}(t)\}}{\mathcal{F}\{\Delta p_{\mathrm{CCH}}^{\mathrm{out}}(t)\}} \,. \tag{72}$$

To analyze the average molar fraction oscillation of a species i along the channel, the following transfer function is defined:

$$Z_{x(i,\mathrm{avg})/p}(\omega) = \frac{\mathcal{F}\{\Delta\bar{x}_{i,\mathrm{CCH}}(t)\}}{\mathcal{F}\{\Delta p_{\mathrm{CCH}}^{\mathrm{out}}(t)\}} \,. \tag{73}$$

To analyze the average partial pressure oscillation of a species i along the channel, the following transfer function is used:

$$Z_{p(i,\mathrm{avg})/p}(\omega) = \frac{\mathcal{F}\{\Delta\bar{p}_{i,\mathrm{CCH}}(t)\}}{\mathcal{F}\{\Delta p_{\mathrm{CCH}}^{\mathrm{out}}(t)\}} \,. \tag{74}$$

In the enumerator of the three transfer functions above, the average value along the channel is calculated by weighting each discrete value with its relative compartment size.
Additional to the average value along the gas channel, transfer functions can be calculated by considering the average value of a different layer in the enumerator. In case of the CL, the quantity is then averaged in both dimensions, through the CL thickness and along the channel length.
Another quantity which is analyzed in the frequency domain (see Chapter 5.1.2.3), is the oscillation of the inlet flow rate at the cathode gas channel $Q_{\mathrm{CCH}}^{\mathrm{in}}$. The corresponding transfer function is defined as

$$Z_{Q/p}(\omega) = \frac{\mathcal{F}\left\{\Delta Q_{\mathrm{CCH}}^{\mathrm{in}}(t)\right\}}{\mathcal{F}\{\Delta p_{\mathrm{CCH}}^{\mathrm{out}}(t)\}} \,. \tag{75}$$

The volumetric flow rate in the enumerator is calculated in Nl s^{-1} and therefore rather a measure of the actual mass flow than a measure of the actual volumetric flow rate.

3.3 Analytical pressure derivative of the cell voltage

Based on the previously-introduced model equations, the derivative of the cell voltage with respect to the cathode outlet pressure is presented in this chapter. With the derivative we want to understand in detail how the cell voltage of the model changes with the outlet pressure.
The cell voltage is the potential difference between both electrodes, reduced by the ohmic losses due to the contact resistances (cf. Eq. 19). It is a measure of the overall system and therefore spatially independent. However, the potential profile between both electrodes is dependent on local quantities and changing in x direction. The derivative of the cell voltage can be approximated by the sum of the derivatives of local potential differences according to

$$\frac{\partial \mathrm{V_{cell}}}{\partial p_{\mathrm{CCH}}^{\mathrm{out}}} \approx \frac{\partial \Delta\phi_{\mathrm{C}}^{\mathrm{eq}}(x)}{\partial p_{\mathrm{CCH}}^{\mathrm{out}}} + \frac{\partial \eta_{\mathrm{C}}(x)}{\partial p_{\mathrm{CCH}}^{\mathrm{out}}} + \frac{\partial \Delta\phi_{\mathrm{elyt}}(x)}{\partial p_{\mathrm{CCH}}^{\mathrm{out}}} \,. \tag{76}$$

The change of the cell voltage with pressure is composed of the change of the equilibrium potential difference and the overpotential at the cathode and the change of the potential difference across the electrolyte. The change of the potential difference at the anode with the cathode outlet pressure is assumed to be insignificant, because the simulated value ranges in the order of nV Pa^{-1}. Subsequently, the derivatives of the right-hand side of Eq. 76 are presented separately.
Throughout the remainder of this work the interpretation of the simulated cell voltage response for an excitation of the cathode outlet pressure is occasionally supported by the use of the derivatives presented in this chapter.

3.3.1 Cathode equilibrium potential

The equilibrium potential difference at the cathode is described by the Nernst potential in Eq. 11. Differentiation with respect to the cathode outlet pressure leads to

$$\frac{\partial \Delta\phi_{\mathrm{C}}^{\mathrm{eq}}(x)}{\partial p_{\mathrm{CCH}}^{\mathrm{out}}} = \frac{RT}{4F}\frac{1}{p_{\mathrm{O_2,CCL}}(x)}\frac{\partial p_{\mathrm{O_2,CCL}}(x)}{\partial p_{\mathrm{CCH}}^{\mathrm{out}}} \ . \tag{77}$$

From this equation one can see that the equilibrium potential changes with the outlet pressure because of a change of the oxygen pressure with the outlet pressure ($\partial p_{\mathrm{O_2,CCL}}(x)/\partial p_{\mathrm{CCH}}^{\mathrm{out}}$). The relationship between both derivatives is determined by the reciprocal of the oxygen pressure.
Eq. 77 is used in the context of Chapter 4.5, 5.1, 5.2 and 7.

3.3.2 Cathode overpotential

To develop the derivative of the cathode overpotential, an explicit expression for the cathode overpotential is needed at first. The BV equation (see. Eq. 8) is an implicit expression of the overpotential. By assuming that the anodic current can be neglected compared to the cathodic current of the ORR ($\exp[\alpha_{\mathrm{A}}F\eta/(RT)] \ll \exp[-\alpha_{\mathrm{C}}F\eta/(RT)]$), the BV equation can be rearranged to the form of the Tafel law, leading to the following explicit expression of the cathode overpotential:

$$\eta_{\mathrm{C}}(x) = -\frac{RT}{\alpha_{\mathrm{C}}F}\ln\left(-\frac{i_{\mathrm{F,C}}^{\mathrm{V}}(x)}{i_{\mathrm{0,C}}^{\mathrm{V}}(x)}\right) \ . \tag{78}$$

The volumetric faradaic current density at position x can be expressed by combining Eq. 13 and Eq. 16:

$$i_{\mathrm{F,C}}^{\mathrm{V}}(x) = \frac{i_{\mathrm{elyt}}^{\mathrm{CL|PEM}}(x)}{L_{\mathrm{CL}}} - C_{\mathrm{DL}}^{\mathrm{V}}\frac{\partial(\Delta\phi_{\mathrm{C}}(x))}{\partial t} \ . \tag{79}$$

Because the faradaic and DL current are both contributing to the ionic current, the volumetric faradaic current density is equal to the ionic current through the electrolyte divided by the CL thickness, minus the volumetric DL current. By using this expression and additionally inserting the expression for the volumetric exchange current density of Eq. 58 in Eq. 78, the following equation for the cathode overpotential can be obtained:

$$\eta_{\mathrm{C}}(x) = -\frac{RT}{\alpha_{\mathrm{C}}F}\ln\left(-\frac{\frac{i_{\mathrm{elyt}}^{\mathrm{CL|PEM}}(x)}{L_{\mathrm{CL}}} - C_{\mathrm{DL}}^{\mathrm{V}}\frac{\partial(\Delta\phi_{\mathrm{C}}(x))}{\partial t}}{i_{0,\mathrm{C}}^{\mathrm{V}}(T)\left(\frac{p_{\mathrm{O_2,CCL}}(x)}{p_{\mathrm{ref}}}\right)^{0.54}}\right) . \quad (80)$$

The derivation of Eq. 80 with respect to the cathode outlet pressure leads then to

$$\frac{\partial\eta_{\mathrm{C}}(x)}{\partial p_{\mathrm{CCH}}^{\mathrm{out}}} = \frac{RT}{\alpha_{\mathrm{C}}F}\frac{0.54}{p_{\mathrm{O_2,CCL}}(x)}\frac{\partial p_{\mathrm{O_2,CCL}}(x)}{\partial p_{\mathrm{CCH}}^{\mathrm{out}}} + \frac{RT}{\alpha_{\mathrm{C}}F}\frac{1}{-i_{\mathrm{elyt}}^{\mathrm{CL|PEM}}(x)+L_{\mathrm{CL}}C_{\mathrm{DL}}^{\mathrm{V}}\frac{\partial(\Delta\phi_{\mathrm{C}}(x))}{\partial t}}\frac{\partial i_{\mathrm{elyt}}^{\mathrm{CL|PEM}}(x)}{\partial p_{\mathrm{CCH}}^{\mathrm{out}}} -$$

$$\frac{RT}{\alpha_{\mathrm{C}}F}\frac{C_{\mathrm{DL}}^{\mathrm{V}}}{-\frac{i_{\mathrm{elyt}}^{\mathrm{CL|PEM}}(x)}{L_{\mathrm{CL}}}+C_{\mathrm{DL}}^{\mathrm{V}}\frac{\partial(\Delta\phi_{\mathrm{C}}(x))}{\partial t}}\frac{\partial}{\partial p_{\mathrm{CCH}}^{\mathrm{out}}}\frac{\partial(\Delta\phi_{\mathrm{C}}(x))}{\partial t} . \quad (81)$$

From the first summand of the derivative of the cathode overpotential one can see that the overpotential changes with the outlet pressure, because of a change of the oxygen pressure with the outlet pressure ($\partial p_{\mathrm{O_2,CCL}}(x)/\partial p_{\mathrm{CCH}}^{\mathrm{out}}$). This expression is similar to the change of the equilibrium potential with the outlet pressure (cf. Eq. 77), and therefore also characterized by the reciprocal of the oxygen pressure. The change of the cathode overpotential with the oxygen pressure can be interpreted as a change of the reaction kinetics due to a change of the exchange current density (see Eq. 58).

Different to the equilibrium potential, the overpotential changes additionally due to a change of the local ionic current density ($\partial i_{\mathrm{elyt}}^{\mathrm{CL|PEM}}(x)/\partial p_{\mathrm{CCH}}^{\mathrm{out}}$) and due to the change rate of the cathode potential per time ($\partial(\partial\Delta\phi_{\mathrm{C}}(x)/\partial t)/\partial p_{\mathrm{CCH}}^{\mathrm{out}}$). Although the cell current density is constant during galvanostatic operation, locally the current density can change during the pressure excitation. This leads to a change of the local reaction rate and hence to a change of the local overpotential. The influence of the change rate of the cathode potential per time on the overpotential is caused by the charge and discharge of the doubly layer. The DL current, the ionic current, and the faradaic current are related according to Eq. 16. A change of the DL current therefore leads also to a change of reaction rate and hence to a change of overpotential.

Eq. 81 is used in the context of Chapter 4.5, 5.1, 5.2 and 7.

3.3.3 Electrolyte potential

The potential difference across the electrolyte at the location x can be quantified by integration of the charge continuity equation (see Eq. 15) over y. The interval of integration is along the electrolyte from the anode CL through the PEM to the cathode CL:

$$\Delta\phi_{\mathrm{elyt}}(x) = \int_{y=\mathrm{CCL}}^{y=\mathrm{ACL}}\frac{i_{\mathrm{elyt}}(x,y)}{\sigma_{\mathrm{elyt}}(x,y)}\mathrm{d}y . \quad (82)$$

The derivative of the electrolyte potential difference with respect to the cathode outlet pressure is then

$$\frac{\partial\Delta\phi_{\mathrm{elyt}}(x)}{\partial p_{\mathrm{CCH}}^{\mathrm{out}}} = \int_{y=\mathrm{CCL}}^{y=\mathrm{ACL}}\left(i_{\mathrm{elyt}}(x,y)\frac{\partial}{\partial p_{\mathrm{CCH}}^{\mathrm{out}}}\left(\frac{1}{\sigma_{\mathrm{elyt}}(x,y)}\right)+\left(\frac{1}{\sigma_{\mathrm{elyt}}(x,y)}\right)\frac{\partial i_{\mathrm{elyt}}(x,y)}{\partial p_{\mathrm{CCH}}^{\mathrm{out}}}\right)\mathrm{d}y . \quad (83)$$

To obtain a handier equation for the derivative of the potential difference across the electrolyte, Eq. 82 is further simplified. By assuming that the majority of the potential difference across the electrolyte occurs in the layer of the PEM and the potential difference in the CLs can be neglected, the limits of integration change and the ionic current becomes independent of the y-coordinate. Furthermore, the proton conductivity is replaced by its average value across the PEM:

$$\Delta\phi_{\mathrm{elyt}}(x) = \frac{i_{\mathrm{elyt}}(x)}{\bar{\sigma}_{\mathrm{elyt}}(x)} L_{\mathrm{PEM}} \ . \tag{84}$$

The proton conductivity of the membrane is increasing with its water content (see Eq. 60), which again is increasing with the water pressure of the gas phase in the adjacent CLs. The relationship between the average proton conductivity of the membrane and the water pressure in the cathode is quite complex and is only approximated here through a very basic approach. As the proton conductivity of the membrane is known to increase with the water pressure in the cathode, the average proton conductivity is assumed to increase proportionally with the water pressure in the cathode according to

$$\bar{\sigma}_{\mathrm{elyt}}(x) = A + B p_{\mathrm{H_2O,CCL}}(x) \ . \tag{85}$$

The two coefficients *A* and *B* are unknown but positive.

Inserting Eq. 85 in Eq. 84 and differentiating with respect to the cathode outlet pressure leads to

$$\frac{\partial \Delta\phi_{\mathrm{elyt}}(x)}{\partial p_{\mathrm{CCH}}^{\mathrm{out}}} = -i_{\mathrm{elyt}}(x) \frac{B}{\left(\bar{\sigma}_{\mathrm{elyt}}(x)\right)^2} \frac{\partial p_{\mathrm{H_2O,CCL}}(x)}{\partial p_{\mathrm{CCH}}^{\mathrm{out}}} + \left(\frac{1}{A + B p_{\mathrm{H_2O,CCL}}(x)}\right) \frac{\partial i_{\mathrm{elyt}}(x)}{\partial p_{\mathrm{CCH}}^{\mathrm{out}}} \ . \tag{86}$$

It should be stressed here that the derivative above can only be used for a qualitative interpretation of the simulations but does not allow a quantitative analysis. Nevertheless, it can be seen that potential loss across the electrolyte changes with the outlet pressure, because of a change of the water pressure with the outlet pressure ($\partial p_{\mathrm{H_2O,CCL}}(x)/\partial p_{\mathrm{CCH}}^{\mathrm{out}}$). The relation between both derivatives is determined by the ionic current density. The change of potential losses across the electrolyte with a change of the water pressure is caused by a change of the humidification and hence conductivity of the electrolyte.

Similar to the derivative of the overpotential (cf. Eq. 81) the change of the potential difference across the electrolyte is also caused by a change of the local ionic current density ($\partial i_{\mathrm{elyt}}(x)/\partial p_{\mathrm{CCH}}^{\mathrm{out}}$).

Eq. 83 is used in the context of Chapter 7 and Eq. 86 in the context of Chapter 4.5, 5.1 and 6.1.1.

4 Model performance

Before actually using the PEMFC model for the simulation of EPIS, its performance is evaluated in this chapter by various other simulations. It comprises simulations which are compared to the experimental data of the project partner, such as the simulation of the I-V curve, EIS, the pressure loss along the gas channel and the water transfer through the PEM. An additional subchapter contains a purely simulative study, in which the static cell voltage response to an increase of the cathode outlet pressure is analyzed. The results in this chapter were partially published in the Journal of the Electrochemical Society [28].

4.1 I-V Curve

The I-V curve, also called polarization curve, shows the characteristic relationship between the cell voltage and cell current of the fuel cell under steady-state conditions. The experimental results were used for the model parametrization to fit the kinetic parameters of the ORR, such as the exchange current density $i_{\mathrm{F},0}^{\mathrm{V}}$ and the cathodic transfer coefficient α_{C}.

Figure 14 shows the experimental polarization curve in comparison with the fitted simulation, noting that the experimental results stop at a maximum current density of 1.0 A cm^{-2} due to safety restrictions of the test bench. In the common current density range, the simulated cell voltage shows a good agreement with the experiments, although there are minor differences visible.

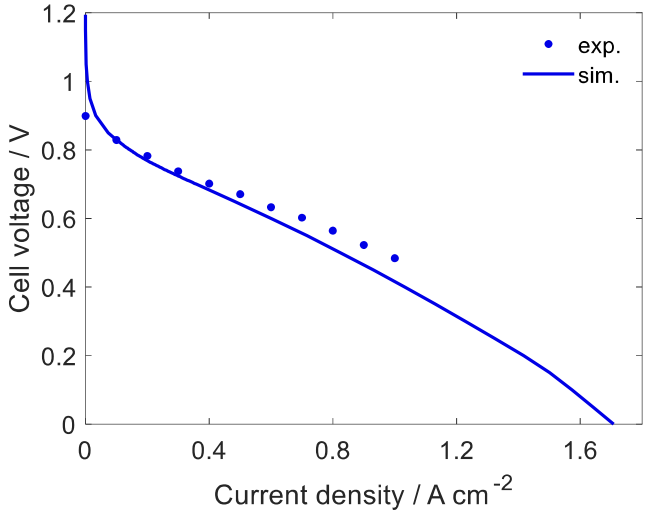

Figure 14: Experimental and simulated steady-state I-V curve operated at 55 °C, 101 325 Pa outlet pressure, with humidified air at the cathode (φ_{C} = 55%, $\lambda_{\mathrm{O_2}}$ = 2.5) and dry hydrogen at the anode (φ_{A} = 5%, $\lambda_{\mathrm{H_2}}$ = 1.2). The figure is extracted from Schiffer et al. [28].

The simulated OCV is close to the equilibrium potential of 1.19 V, which describes the thermodynamic cell voltage at equilibrium. The small difference between the simulated OCV and the equilibrium potential is caused by the fact that there are small overpotentials even at OCV. Although the overall current is zero at OCV, the simulations show that there are locally compensating currents flowing, due to an uneven reactant concentration along the channel, as a consequence of the pressure gradient. However, with the local currents of the simulation being in the magnitude of 10^{-6} A cm^{-2}, the resulting overpotentials are rather insignificant.

The OCV predicted by the simulations is above the experimentally observed OCV, which was observed before. The measured OCV is typically in the range of 0.95–1.05 V, so that compared to the equilibrium potential there is already a loss of up to 20% of efficiency at OCV. In the literature, several possible reasons for the potential difference are given [5,95,96]. A likely given explanation by Vilekar and Datta [96] is the gas transfer between the electrodes, which is not included in the present model under the assumption of gas impermeability of the PEM.

Another difference between the experimental and simulated polarization curve can be seen at current densities above 0.4 A cm^{-2}. The slope of the simulated curve is decreasing continuously, while the slope of the experimental curve remains nearly constant. In this current density range the gradient of the curve is dominated by the ohmic losses. This leads to the hypothesis that the decreasing slope of the simulated polarization curve is caused by a decrease of the electrolyte conductivity, due to a local dry-out. The hypothesis that the simulated and experimental electrolyte conductivity is different is supported by the observations made in the subsequent chapters of the EIS (cf. Chapter 4.2) and the water transfer through the PEM (cf. Chapter 4.4).

To conclude, despite the mentioned differences between the experiment and the simulation, the PEMFC model is able to reproduce the current-voltage behavior of the fuel cell at steady state.

4.2 EIS

In this subchapter, the model performance in terms of the dynamic current-voltage relationship is evaluated by means of a comparison between simulated and experimental EIS. This comparison was used for further model parametrization by fitting the parameters of the contact resistance R_{contact} and the cathode DL capacity C_{DL}. The methodology of EIS is briefly described in Chapter 3.2.1 above.

The comparison between the experimental and simulated EIS is shown in Figure 15 in the Nyquist representation for a variation of current densities. The experimental spectra were recorded for a minimum frequency of 0.1 Hz, whereas the frequency range of the simulations was extended to a minimum frequency of 1 mHz.

First, the experimental spectra are described. The intercept of the spectra with the real axis at high frequencies is relatively independent of the current density. The intercept can be interpreted as the total ohmic resistance of the cell [97], as the cell response at such high frequencies is expected to be purely ohmic. The ohmic resistance of the cell consists of the resistance of the electron-conducting phase, which is dominated by the contact resistances, and the resistance of the ion-conducting phase, the electrolyte. Therefore, the total ohmic resistance of the tested fuel cell is ca. 0.18 Ω cm^2. The inductive behavior of the impedance observed in the experiments above 1 kHz is expected to originate from the magnetic field created by the wires [7].

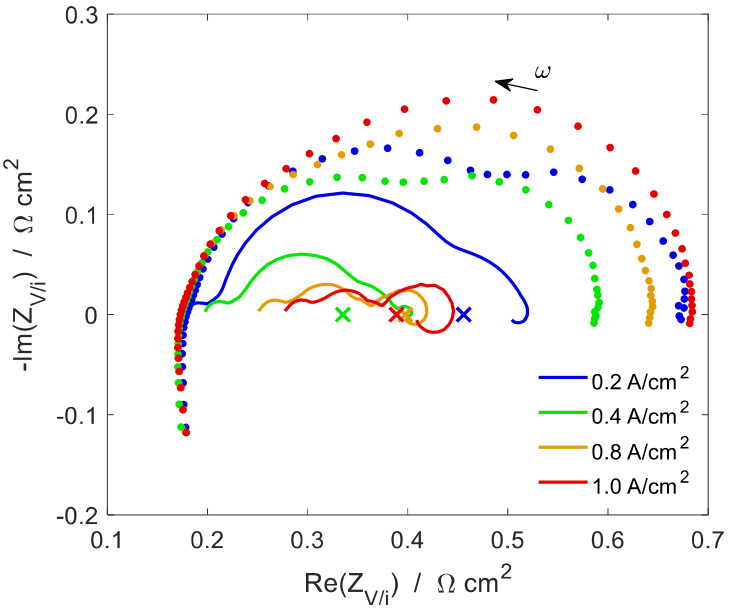

Figure 15: Nyquist plot of experimental (circles) and simulated (solid lines) EIS results of the transfer function $Z_{V/i}$ between the cell voltage response and the cell current excitation for different current densities. The experimental DC resistance (crosses), which is the gradient of the polarization curve in Figure 14, is plotted on the real axis. The figure is adapted from Schiffer et al. [28].

The experimental spectra reveal two overlapping arcs, which are more distinct at lower current density. With increasing current density, the low-frequency arc (LFA) seems to increase, while the high-frequency arc (HFA) decreases, which leads to a progressively masking of the HFA by the LFA. This observation is similar to the EIS results of Xie and Holdcroft [98], who also report an increase of the LFA and a decrease of the HFA with increasing polarization. In the literature, it is generally accepted that the HFA is caused by the charge transfer resistance of the ORR in the cathode CL together with the DL capacity [8,10,12,99]. The origin of the LFA is a rather debated topic in the literature [13]. The LFA has often been interpreted as a mass transport resistance caused by limited gas diffusion in the GDL [8–11,100]. However, Schneider et al. [101,102] report a reasonable

doubt about this interpretation by showing appropriate experiments. They argue that the LFA is rather a phenomenon of the gas channel.

Subsequently, the simulated spectra are discussed. The parameter of the contact resistance was fitted to $R_{\mathrm{contact}} = 6.3 \cdot 10^{-2}\ \Omega\ \mathrm{cm}^2$ so that the simulated intercept with the real axis at high frequency matches with the experiments at a current density of 0.2 A cm^{-2}. From this value it can be deduced that the ohmic resistance of the electrolyte is ca. $R_{\mathrm{elyt}} = 0.12\ \Omega\ \mathrm{cm}^2$ at the same cell load. Different to the experiments, the total ohmic resistance increases with current density, which has to be caused by an increase of the electrolyte resistance, as the contact resistance is constant. This agrees with the previous observation in the context of the I-V curve, in which the slope of the simulated curve is decreasing in the ohmic region, while the experimental curve has a constant slope. It has been hypothesized that this observation is caused by a dry-out of the electrolyte, which is discussed more detailed in the subchapter of the water transfer through the PEM.

Different to the experiments, the simulated spectra reveal three different capacitive arcs, with an additional inductive loop towards the lowest frequencies. The small arc in the highest frequency region above 1 kHz is not observed in the experiments and without explanation of occurrence. The two bigger overlapping arcs in the frequency range below are expected to correspond to the HFA and LFA of the experiments and are hereafter also referred as HFA and LFA. The low-frequency inductive loop was observed in other EIS experiments before [103,104].

The HFA of the simulation is likewise pronounced at 0.2 A cm^{-2} as in the experiments. With increasing current density, the HFA of the simulations decreases strongly. Therefore, the HFA of the simulation at 0.2 A cm^{-2} was used for the parametrization of the capacitance of the DL: The negative imaginary part and the real part of the impedance are plotted against the frequency, as shown in Figure 16. The characteristic time of the arcs of the Nyquist plot correspond to the frequency of the local maximum of the negative imaginary part of the impedance, shown in the top panel of Figure 16. The cathode DL capacity was fitted to $C_{\mathrm{DL}}^{\mathrm{V}} = 4.1 \cdot 10^{7}\ \mathrm{F\ m}^{-3}$, so that the frequency of the high frequency maximum matches between the experiments and the simulation.

The LFA of the simulation is already less pronounced at 0.2 A cm^{-2} than in the experiments. With increasing current density, the difference between the experimental and simulated spectra increases, as the simulations show a decreasing trend of the LFA, contrary to the trend of the experiments.

The inductive loop of the simulated spectra of the Nyquist plot can be seen in Figure 16 in the frequency range below 0.1 Hz. The process seems to be more pronounced at higher current densities. As the experimental spectra are only recorded down to a minimum frequency of 0.1 Hz, this observation cannot be confirmed by the experiments. Based on the low-frequency range of this time-dependent process, this feature might be related to a

change in the humidification of the electrolyte and consequently to a change in electrolyte conductivity.

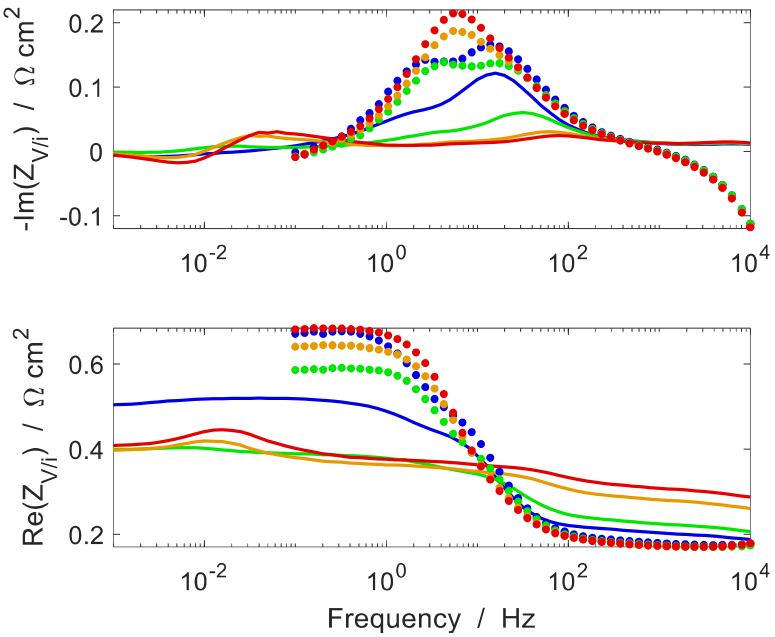

Figure 16: Bode plot of experimental (circles) and simulated (solid lines) EIS results of the transfer function $Z_{V/i}$ between the cell voltage response and the cell current excitation in for different current densities. The imaginary part (top panel) and the real part (bottom panel) of the impedance $Z_{V/i}$ are plotted against the frequency. The figure is adapted from Schiffer et al. [28].

This EIS study contains some remarks at the end about the low-frequency intercept with the real axis of the simulated and experimental spectra in Figure 15. Theoretically, at quasi-static conditions, the impedance corresponds to the negative slope of the I-V curve, representing the relationship between cell voltage and current density at the current cell load at steady state. To compare the slope of the polarization curve with the impedance at low frequencies, the slope of the experimental polarization curve is added on the abscissa of the Nyquist plot, for each analyzed current density. In case of the experimentally obtained impedance, this value differs strongly from the slope of the polarization curve, being up to nearly twice as much. This difference was already observed and analyzed in previous studies [105,106]. The difference is related to the fact that the stoichiometry is oscillating during EIS, due to a constant flow rate and changing current density, while the polarization curve is obtained under constant stoichiometry. Although the EIS simulations were made under the same flow rate conditions as the experiments (see Chapter 3.2.1), the impedance of the simulation at the lowest frequency is way smaller and corresponds more to the slope of the simulated polarization curve albeit not exactly.

To conclude, at a current density of 0.2 A cm^{-2}, the dynamic current-voltage relationship can be approximated accurately with the PEMFC model, whereas with increasing current density the dynamic behavior diverges between the experiments and the simulation.

4.3 Pressure loss along the gas channel

The pressure loss along the gas channel is described by the wall shear stress expressed in Eq. 61. It considers two friction factors. The first one f_1 describes the pressure losses of the laminar flow, which are proportional to the flow velocity and the second one f_2 describes the additional losses, caused by the turns or entrance/exit of the serpentine flow field, which are proportional to the square of the flow velocity.

Figure 17 shows results of the parameter fit to measured pressure losses in the cathode gas channels for varying flow rates at 20 °C and 50 °C. The fitted friction factors are valid for both, anode and cathode, because the flow field is the same. It can be seen that, with the fit of friction factors f_1 = 18.5 and f_2 = 0.021, the pressure change along the channel can be described sufficiently accurate.

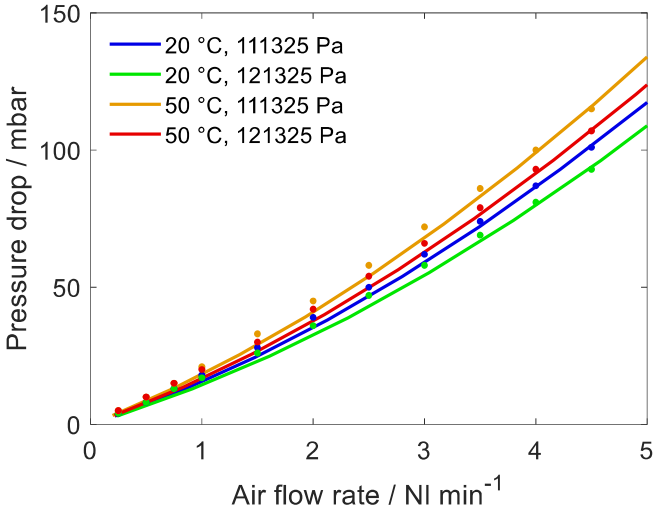

Figure 17: Experimental (circles) and simulated (solid lines) pressure drop in the cathode gas channels plotted against the air flow rate (total flow rate of all 23 channels) for different temperatures. The cell was operated at OCV. The figure is extracted from Schiffer et al. [28].

4.4 Water transfer through the PEM

In this subchapter, the ability of the PEMFC model to reproduce the measured water transfer through the PEM is evaluated.

The transferred amount of water from the cathode to the anode is often given in relation to the produced amount of water as a coefficient. With neglecting the small amount of water in the anode gas feed, the transfer coefficient can be calculated as the flow rate of water at the anode outlet in relation to the produced water according to

$$\alpha = \frac{\dot{n}_{\mathrm{H_2O,ACH}}^{\mathrm{out}}}{i_{\mathrm{cell}} A_{\mathrm{FC}}/(2Fn_{\mathrm{CH}})} \,. \tag{87}$$

Figure 18 shows results of the experimental and simulated water transfer coefficient α for varying current densities. The experimental data is only available up to a maximum current density of 1.0 A cm^{-2}, whereas the simulated coefficient is shown up to the maximum current density at 0 V, analogue to the I-V curve in Figure 14. The experimental water transfer coefficient shows a linear increase with current density. At 0.2 A cm^{-2} ca. 10% of the produced water are transferred to the anode, increasing up to ca. 30% at 1.0 A cm^{-2}. Although the simulations show qualitatively the same trend in that current density range, they are quantitatively a magnitude smaller with a maximum transfer of 3% of the produced water. Above 1.0 A cm^{-2} the simulated transfer coefficient even decreases. The model is thus not able to reproduce the experimentally observed water balance accurately, which becomes more prominent with increasing current density.

For the present operating conditions of a humidified gas feed at the cathode and a dry gas feed at the anode, the water transfer through the PEM is important for the humidification of the electrolyte at the anode. The humidification again ensures the sufficient conductivity of the electrolyte. The observed difference between the conductivity of the experiments and the simulation in the Chapters 4.1 and 4.2 is therefore probably caused by the demonstrated limited ability of the model to reproduce the water transfer through the PEM.

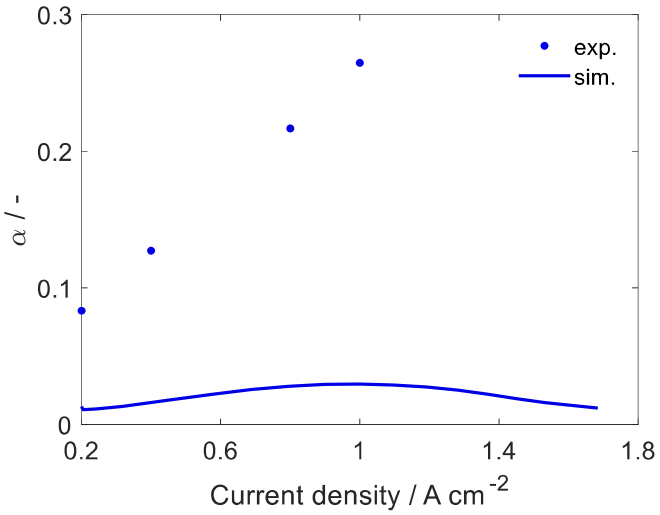

Figure 18: Experimental (circles) and simulated (solid lines) water transfer coefficient α. The cell was operated at 55 °C, 101 325 Pa outlet pressure, with humidified air at the cathode (φ_{C} = 55%, $\lambda_{\mathrm{O_2}}$ = 2.5) and dry hydrogen at the anode (φ_{A} = 5%, $\lambda_{\mathrm{H_2}}$ = 1.2).

To find an explanation for the difference between the experimental and simulated water transfer, the different mechanisms of water transfer through the PEM are recalled. Assuming that the PEM is impermeable for gases, water is transferred through the electrolyte by the following mechanisms. The electro-osmotic drag is the drag of water by the

hydrogen ions, which move from anode to cathode. Due to a gradient of humidification across the electrolyte, water diffuses in the direction opposed by the gradient. These two mechanisms are incorporated by the model as described in Chapter 3.1.2.5. Additionally, at high current densities where a lot of water is produced, water is expected to move by convection, due to a hydraulic pressure gradient across the electrolyte [26]. This mechanism is not included in the present model, which may be a reason for the observed difference between the simulations and the experiments. However, the water transfer through the electrolyte is not expected to be critical for the reproduction of EPIS.

4.5 Static pressure-voltage response

Before analyzing the dynamic relationship between the cell voltage and the cathode outlet pressure in the context of EPIS in Chapter 5, 6 and 7, their static relationship is analyzed. To achieve this, galvanostatic steady-state simulations at different current densities between 0–1.0 A cm^{-2} were conducted with the reference cathode outlet pressure and with an increase of the outlet pressure by 100 Pa. The static cell voltage response is then analyzed in relation to the cathode outlet pressure increase as the following quotient and is hereafter referred to as the static pressure-voltage response:

$$\frac{\Delta V_{\mathrm{cell}}}{\Delta p_{\mathrm{CCH}}^{\mathrm{out}}} = \frac{V_{\mathrm{cell}}\left(p_{\mathrm{CCH}}^{\mathrm{out}}=116\,425\ \mathrm{Pa}\right)-V_{\mathrm{cell}}\left(p_{\mathrm{CCH}}^{\mathrm{out}}=116\,325\ \mathrm{Pa}\right)}{100\ \mathrm{Pa}} \,. \tag{88}$$

First, the static pressure-voltage response as a function of the current density is discussed. Subsequently, for selected current densities, the static pressure-voltage response is split into the response of its constituent potential differences across the MEA.

Figure 19 shows the simulated static pressure-voltage response as function of the cell current density. For all current densities, the increase of the cathode outlet pressure leads to an increase of the cell voltage with values between 0.06–1.2 µV Pa^{-1}. The change of the cell voltage increases with current density, with an abrupt increase from OCV to the first simulated cell load, followed by a moderate growth which further increases with current density.

A similar increase of the cell voltage response towards higher current densities was observed by Zhang et al. [107], who made a combined theoretical and semi-empirical study on the effect of the outlet pressure increase on the cell voltage. They concluded that the outlet pressure affects the equilibrium potential, the exchange current densities of the electrochemical reactions, the membrane conductivity as well as mass transfer properties. Their results are partially supported by a previously published experimental study on the effect of the outlet pressure on the fuel cell performance [108].

To understand how the outlet pressure affects the cell voltage of the present model in detail, the cell voltage response can be subdivided into the response of its constituent potential differences across the MEA. According to the analytical pressure derivative of the

cell voltage in Chapter 3.3, the change of the cell voltage is composed of the change of the equilibrium potential and the overpotential at the cathode and the change of the potential difference across the electrolyte. The change of the anode potential with the cathode outlet pressure is stated to be insignificant.

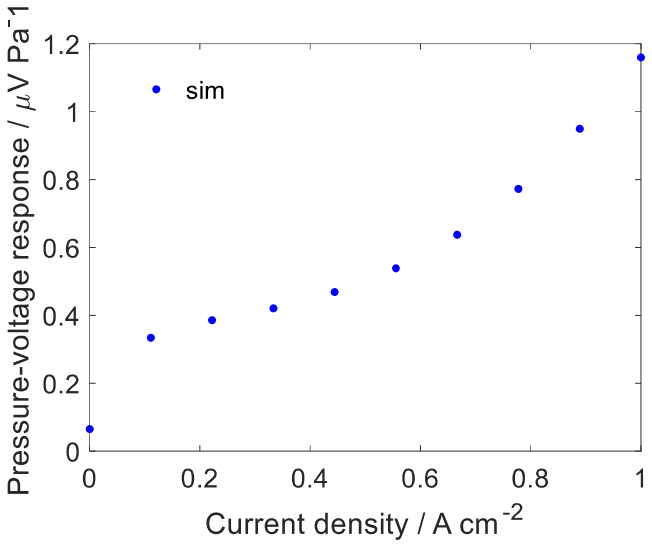

Figure 19: Simulated static pressure-voltage response plotted against the cell current density. Beside the increase of the cathode outlet pressure by 100 Pa from the default value, the cell was operated at the default operating conditions.

The decomposition of the simulated static pressure-voltage response into its constituents is shown in Figure 20 for four selected current densities. The constituents are stacked so that they can be cumulated to the total pressure-voltage response. Furthermore, the stacked elements are plotted as function of the x-direction, as the composition depends on local states (see Chapter 3.3).

In the top left panel at OCV it can be seen that the cell voltage changes according to the change of the cathode equilibrium potential with 0.06 µV Pa^{-1}. This value is nearly independent of the x-direction and can be approximated by the use of the derivative of the equilibrium potential with respect to the cathode outlet pressure (cf. Eq. 77):

$$\frac{\partial \Delta\phi_{\mathrm{C}}^{\mathrm{eq}}(x)}{\partial p_{\mathrm{CCH}}^{\mathrm{out}}} = \frac{RT}{4F}\frac{1}{p_{\mathrm{O_2,CCL}}(x)}\frac{\partial p_{\mathrm{O_2,CCL}}(x)}{\partial p_{\mathrm{CCH}}^{\mathrm{out}}} \approx \frac{RT}{4F}\frac{1}{\bar{p}_{\mathrm{CCL}}} = 0.06\ \mu\mathrm{V\ Pa^{-1}}\ , \qquad (89)$$

with the average pressure in the CL of $\bar{p}_{\mathrm{CCL}}$ = 1.17 bar. The product of the reciprocal partial pressure of oxygen and its derivative are approximated through the following relation:

$$\frac{1}{p_{\mathrm{O_2,CCL}}(x)}\frac{\partial p_{\mathrm{O_2,CCL}}(x)}{\partial p_{\mathrm{CCH}}^{\mathrm{out}}} = \frac{1}{p_{\mathrm{CCL}}(x)}\frac{\partial p_{\mathrm{CCL}}(x)}{\partial p_{\mathrm{CCH}}^{\mathrm{out}}} + \frac{1}{x_{\mathrm{O_2,CCL}}(x)}\frac{\partial x_{\mathrm{O_2,CCL}}(x)}{\partial p_{\mathrm{CCH}}^{\mathrm{out}}} \approx$$

$$\frac{1}{p_{\mathrm{CCL}}(x)}\frac{\partial p_{\mathrm{CCL}}(x)}{\partial p_{\mathrm{CCH}}^{\mathrm{out}}} \approx \frac{1}{p_{\mathrm{CCL}}(x)} \approx \frac{1}{\bar{p}_{\mathrm{CCL}}}\ . \qquad (90)$$

First, the partial pressure of oxygen is replaced by the product of its molar fraction and the total pressure and subsequently differentiated. For a pressure increase at steady state, the change of molar fraction is expected to be insignificant (see Chapter 5.1.2), hence its

derivative is assumed to be zero. Furthermore, the change of total pressure is assumed to be uniform throughout the channel. Finally, the local pressure along the channel is replaced by its average value. As a comparison, Engebretsen et al. [19] reported a measured voltage increase of 0.15 µV Pa^{-1} at OCV, which they stated to be consistent with the theoretic change of equilibrium potential with pressure.

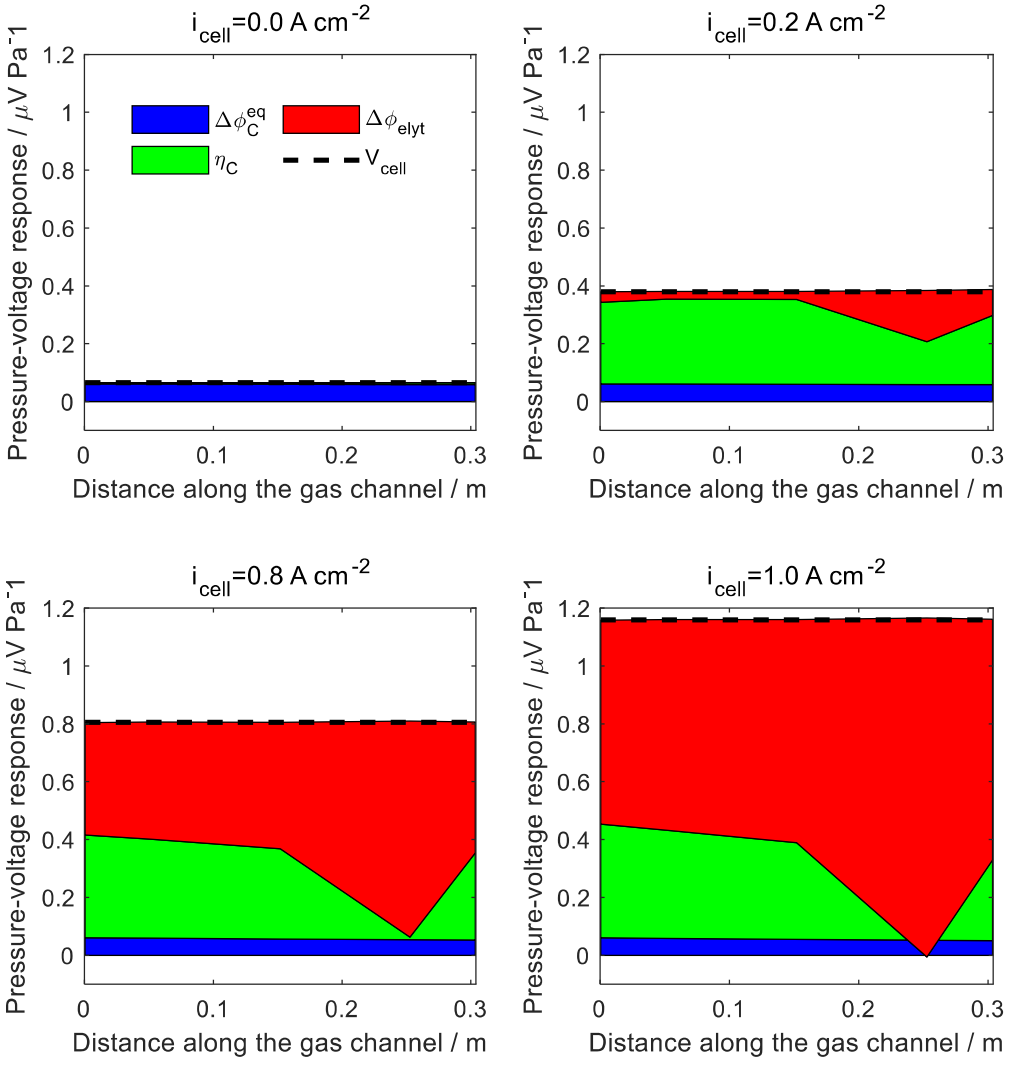

Figure 20: Composition of the simulated static cell voltage response for a cathode outlet pressure increase by 100 Pa plotted against the distance along the cathode gas channel (0 m corresponds to the cathode inlet) at four different current densities. The response of the cell voltage is subdivided into the response of the cathode equilibrium potential and overpotential and the potential difference across the electrolyte. The voltage response is given in relation to the pressure increase.

In the remaining panels, the fuel cell is operated under load. The comparison of the response of the equilibrium potential in the panels under load with the panel at OCV shows that the response of the equilibrium potential remains the same and can be stated as independent of the current density.

Under load, the change of the cathode overpotential and the change of the potential difference across the electrolyte contribute additionally to the change of the cell voltage. At

0.2 A cm^{-2} the highest share belongs to the change of the overpotential. The previously observed abrupt increase of the static pressure-voltage response from OCV to operation under load (see Figure 19) can therefore be mainly attributed to the increased reaction kinetics with pressure.

The cathode overpotential changes with the cathode outlet pressure according to its derivative in Eq. 81. Without considering the time-dependent terms in the present static analysis, the derivative simplifies to

$$\frac{\partial \eta_{\mathrm{C}}(x)}{\partial p_{\mathrm{CCH}}^{\mathrm{out}}} = \frac{RT}{\alpha_{\mathrm{C}} F} \frac{0.54}{p_{\mathrm{O_2,CCL}}(x)} \frac{\partial p_{\mathrm{O_2,CCL}}(x)}{\partial p_{\mathrm{CCH}}^{\mathrm{out}}} + \frac{RT}{\alpha_{\mathrm{C}} F} \frac{1}{-i_{\mathrm{elyt}}^{\mathrm{CL|PEM}}(x)} \frac{\partial i_{\mathrm{elyt}}^{\mathrm{CL|PEM}}(x)}{\partial p_{\mathrm{CCH}}^{\mathrm{out}}} \ . \tag{91}$$

The first term in the equation above describes the change of the cathode overpotential caused by a change of the oxygen pressure and has a similar form compared to the derivative of the cathode equilibrium potential (cf. Eq. 89). Therefore, this term has to be also relatively independent of the x-coordinate and can be approximated by the use of Eq. 90 to

$$\frac{RT}{\alpha_{\mathrm{C}} F} \frac{0.54}{p_{\mathrm{O_2,CCL}}(x)} \frac{\partial p_{\mathrm{O_2,CCL}}(x)}{\partial p_{\mathrm{CCH}}^{\mathrm{out}}} \approx \frac{RT}{\alpha_{\mathrm{C}} F} \frac{0.54}{\bar{p}_{\mathrm{CCL}}} = 0.23 \ \mu\mathrm{V\ Pa^{-1}} \ . \tag{92}$$

Furthermore, similar to the derivative of the equilibrium potential this term is independent of the current density. Therefore, the average value of the overpotential response is constant, except towards OCV where the reaction kinetics become irrelevant.

The potential difference across the electrolyte changes with the outlet pressure according to the derivative of Eq. 86. The first term describes the influence of the water pressure. The increase of the water pressure leads to an increased humidification and hence conductivity of the electrolyte. This effect is proportional to the current density, which is the reason why the highest portion of the static pressure-voltage response at 1.0 A cm^{-2} belongs to the change of the potential difference across the electrolyte.

Different to the response of the equilibrium potential, the response of the overpotential and the potential difference across the electrolyte are significantly dependent on the x-direction. However, the sum of both measures is independent of the x-direction, which shows that their relationship is interdependent. This has to be the case, because the sum of all potential changes has to correspond to the change of the cell voltage, which is independent of the x-direction. The second term of Eq. 91 describes the change of the cathode overpotential caused by a change of the local current density. Although the cell current density is constant for a galvanostatic operation, the current density can change locally. Looking at the second term of the derivative of the potential difference across the electrolyte in Eq. 86 reveals that it is also dependent on the change of the local current density. The aforementioned interdependence between the response of the cathode overpotential and the potential difference across the electrolyte is therefore caused by the change of the local current density. Furthermore, the interdependence changes with the cell load.

5 EPIS (1): Analysis of pressure dynamics

After the preliminary study of the model performance, we now want to turn to the analysis of EPIS, which is divided into three parts. The aim of the first part is to work out the origin of typical EPIS features which were observed in the experiments for the operation with air as the cathode gas feed. Zhang et al. [18] and Shirsath et al. [14–17] both measured an increase of the magnitude with frequency up to a maximum around 1 Hz, accompanied by a continuous decrease in phase shift. In the following, an explanation for these features is demonstrated.

As stated appropriately by Zhang et al. [18], "the cell voltage is the cumulative response of all the pressure signals along the channel". To understand the cell voltage response, it is hence crucial to analyze the pressure response along the channel at first, which is done in the first subchapter. In the second subchapter the cell voltage response with its characteristic features is explained by tracing them back to the previous observations of the pressure response analysis. The chapter closes with a conclusion.

The results of this chapter were partially published in Schiffer et al. [28], which is indicated in the description of the relevant figures. The experimental data used in this chapter was provided by the project partner.

5.1 Pressure response

In the presented PEMFC model, the cell voltage is affected by a change of the partial pressures of oxygen and water. The oxygen pressure has a direct influence on the equilibrium potential (cf. Eq. 77) and the overpotential (cf. Eq. 81) of the cathode. The water pressure has an indirect influence on the conductivity of the electrolyte and hence on the potential difference across the electrolyte (cf. Eq. 86). Therefore, it is important to analyze the partial pressure oscillation of both species.

To understand how the partial pressure of oxygen and water change during the pressure excitation, the derivative of the partial pressure with respect to the outlet pressure is shown subsequently. The partial pressure of a species i can be expressed as the product of the total pressure and its molar fraction:

$$p_i(x) = p(x)x_i(x) \ . \tag{93}$$

The derivative of the partial pressure with respect to the cathode outlet pressure is then

$$\frac{\partial p_i(x)}{\partial p_{\mathrm{CCH}}^{\mathrm{out}}} = x_i(x)\frac{\partial p(x)}{\partial p_{\mathrm{CCH}}^{\mathrm{out}}} + p(x)\frac{\partial x_i(x)}{\partial p_{\mathrm{CCH}}^{\mathrm{out}}} \ . \tag{94}$$

From the equation above it can be seen that the change in partial pressure depends on the change in total pressure, represented by the first summand and the change of the molar

fraction, represented by the second summand. In the following it is shown that the ratio between these two summands changes with the excitation frequency.
The total and partial pressure oscillations in the cathode during one excitation period are shown in Figure 21 and Figure 22 for two different excitation frequencies respectively. The subplots of the figures correspond to the location at the height of the channel inlet, center and outlet. For the quasi-static frequency of 1 mHz in Figure 21, the total pressure oscillation is quite uniform along the channel. The species partial pressure oscillations follow the total pressure oscillation with a reduced amplitude corresponding to the species molar fraction. An exception is the water pressure at the channel inlet, which is constant due to the boundary condition of constant relative humidity. Taking a look at Eq. 94 reveals that the change of partial pressure is dominated by the first summand. This means the change of the molar fraction is insignificant at the quasi-static frequency.

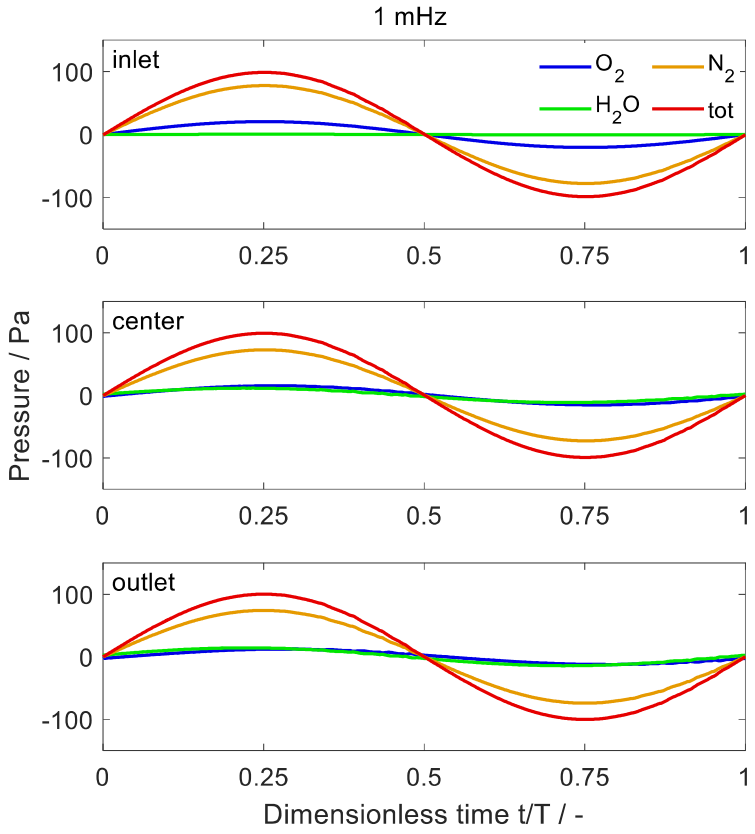

Figure 21: Total and partial pressures oscillation (averaged over the CCL thickness) at 1 mHz during one excitation period T at the gas channel inlet, center, and outlet. The amplitude of the outlet pressure excitation is 100 Pa. The cell was operated at 0.2 A cm^{-2}. The figure is adapted from Schiffer et al. [28].

At an increased frequency of 0.56 Hz, shown in Figure 22, the pressure dynamics change and become more complex. The total pressure at the inlet oscillates only with a small remaining amplitude, while the oscillation at the outlet is forced externally with the given amplitude and phase. The partial pressure oscillations at the inlet show only small

amplitudes, whereas towards the channel outlet the oscillations become strongly amplified and do not follow the total pressure oscillation anymore. At the channel center and outlet, the amplitudes of the partial pressure oscillations exceed the amplitude of the total pressure oscillation, in case of oxygen at the outlet about three times. Furthermore, at the same positions, the oxygen pressure oscillation is in antiphase with the total pressure oscillation. An explanation for the different behavior of the partial pressure oscillation at an increased frequency can be found by looking at Eq. 94. While for the quasi-static frequency the change of partial pressure is dominated by the first summand, for the increased frequency the change of partial pressure has to be significantly influenced by the second summand. This means that at 0.56 Hz, the molar fraction of species oscillates with a considerable amount along the channel.

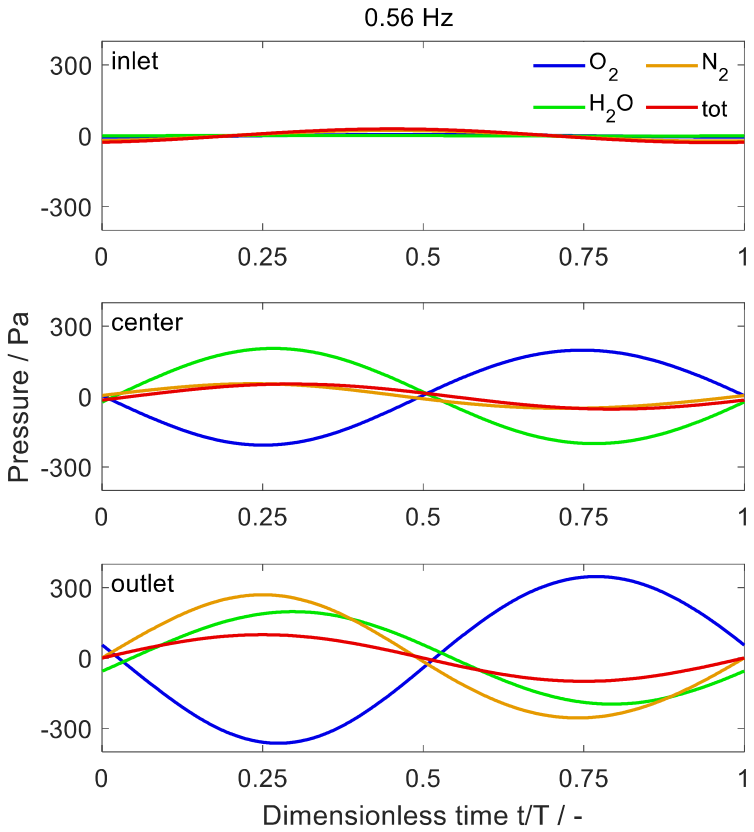

Figure 22: Total and partial pressures oscillation (averaged over the CCL thickness) at 0.56 Hz during one excitation period T at the gas channel inlet, center, and outlet. The amplitude of the outlet pressure excitation is 100 Pa. The cell was operated at 0.2 A cm^{-2}. The figure is adapted from Schiffer et al. [28].

Based on this finding, the frequency dependence of the pressure response is further studied as follows. First, the total pressure response is analyzed, followed by a study of the oscillation of the species molar fraction. In the last section, the partial pressure response is discussed.

5.1.1 Total pressure

In the experiments, the total pressure response in the cathode gas channel was studied by means of the inlet pressure oscillation. The same approach is followed in the first part of this section. In the later part, additionally, the average total pressure oscillation along the channel is presented.

5.1.1.1 Inlet pressure

The inlet pressure response is analyzed in relation to the outlet pressure excitation in the frequency domain by the use of the transfer function $Z_{p/p}$ between both quantities, calculated according to Eq. 3. First, the ability of the present model to reproduce the experimentally observed pressure dynamics is shown. Subsequently, simulated results showing the influence of the gas volume in the humidifier and the influence of the gas channel length on the transfer function are demonstrated.

Figure 23 shows a comparison of simulated and experimental spectra of the transfer function $Z_{p/p}$ between the inlet pressure oscillation and the outlet pressure excitation at different current densities. The experiments are only available up to a maximum frequency of 1 Hz, while the simulations were extended up to a frequency of 100 Hz.

Taking a look at the experimental spectra first reveals that the magnitude at the lowest frequency is close to one and the phase shift zero. This means that the pressure oscillation is nearly uniform throughout the channel.

With increasing excitation frequency, a characteristic decrease in magnitude and phase shift can be observed. The decrease in magnitude with frequency can be interpreted as an increased damping of the pressure oscillation at the channel inlet, which was also observed by Zhang et al. [18]. At 1 Hz, the inlet pressure oscillates with a remaining amplitude of 10% of the outlet pressure oscillation. The decrease in phase shift with frequency can be interpreted as an increased delay of the inlet pressure oscillation compared to the outlet pressure excitation. At 1 Hz, the phase shift between both quantities is between -70 and –80°.

The variation of current density does not reveal a clear trend for the experimental spectra. It can be hypothesized that the small difference between the different currents is caused by the scattering of the data.

The comparison of the simulated spectra with the experiments shows that both, magnitude and phase shift, reveal a good qualitative and quantitative agreement. This proves that the model is able to reproduce the experimentally observed damping and delay of the pressure excitation along the channel.

For frequencies below 10 mHz, the simulated magnitude is slightly below 1 which is more pronounced with increasing current density. This phenomenon was also observed by Zhang et al. [18]. The authors attribute this observation to the mass flow controller, which

is affected by the pressure change during excitation. We give a different explanation for this phenomenon [28]. Because the mass flow rate at the inlet is constant during pressure excitation, the flow velocity decreases with increasing pressure. The pressure loss along the channel is proportional to the velocity and, therefore, decreases with decreasing velocity. This results in a smaller pressure increase at the inlet compared to the outlet. This effect fortifies with increasing current density, as the mass flow increases with current density for a constant oxygen stoichiometry.

Another observation of the simulated spectra is that the decrease in magnitude and phase shift with frequency is shifted towards lower frequencies for increasing current densities and hence, increasing flow rates. This observation agrees with the observation of Zhang et al. [18], who reported a decrease of the characteristic frequency with increasing flow rate.

The simulations beyond the frequency range of the experiments confirm the experimental trend of the magnitude to approach zero. The phase shift above 1 Hz shows a minimum at ca. 80° with a following increase towards 100 Hz. The increase of phase shift was not further investigated, because the magnitude in this frequency range tends to zero.

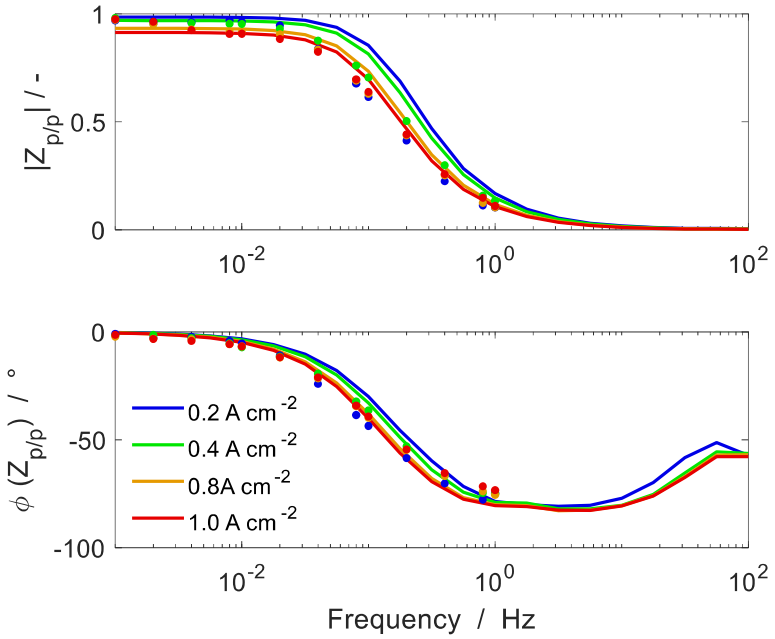

Figure 23: Bode plot of experimental (circles) and simulated (solid lines) spectra of the transfer function $Z_{p/p}$ between the inlet pressure oscillation and the outlet pressure excitation at different current densities. The figure is adapted from Schiffer et al. [28].

Although Shirsath et al. and Zhang et al. both observed a damping and delay of the pressure excitation along the channel, they give different explanations for this phenomenon. Shirsath et al. [14,17] relate the observed pressure dynamics to the gas reservoir in the humidifier upstream the fuel cell, which is supported by their experiments with varying gas volumes inside the humidifier. However, Zhang et al. [18] argue that the observed

pressure dynamics are not related to the humidifier, but rather to the gas volume of the gas channel. Their statement is based on their observation that different flow fields operated with the same humidifier configuration lead to different pressure dynamics. To work out the influence of both parameters on the transfer function $Z_{p/p}$, simulations for a variation of the gas volume inside the humidifier and simulations for a variation of the gas channel length are shown in the following consecutively.

In the study presented in Figure 24, the gas volume in the humidifier is varied between 0–1000 ml; note that the default volume corresponding to the experimental setup is 850 ml. The simulated spectra of $Z_{p/p}$ for a cell load of 0.2 A cm^{-2} reveal a strong dependence on the gas volume. By decreasing the volume, the damping and delay of the pressure excitation along the channel gets shifted towards higher frequencies. This trend agrees with the observation of the experiments of Shirsath et al. [17].

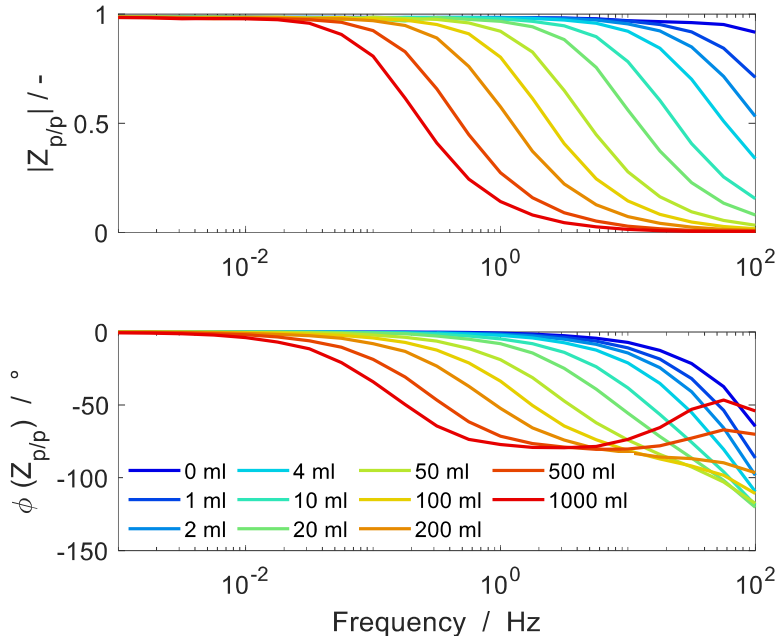

Figure 24: Bode plot of simulated spectra of the transfer function $Z_{p/p}$ between the inlet pressure oscillation and the outlet pressure excitation for different gas volumes in the cathode humidifier (default value: V_{hum} = 850 ml) at 0.2 A cm^{-2}. The figure is adapted from Schiffer et al. [28].

Without consideration of the gas volume in the humidifier, the amplitude of the pressure oscillation at the inlet nearly remains the same over the whole frequency range, and the phase shift becomes significant first above 1 Hz. Therefore, it can be concluded that the experimentally observed damping and delay of the pressure oscillation along the channel in the frequency range below 1 Hz is caused by the humidifier gas volume upstream the fuel cell.

After showing that the experimentally observed pressure dynamics below 1 Hz are caused by the humidifier, the additional influence of the channel length is analyzed. Figure

25 shows simulated spectra of the transfer function $Z_{p/p}$ for three different channel lengths with consideration of the humidifier. The flow rates were adjusted so that the stoichiometries remained constant. The default channel length, corresponding to the experiments, is 0.304 m. By doubling the default channel length, the magnitude at the lowest frequency decreases. Possible reasons for the quasi-static magnitude below one were discussed previously in the context of the current density study of $Z_{p/p}$. Considering the argument of a changing pressure loss along the channel during pressure excitation, the effect becomes more pronounced for a longer channel and hence, greater pressure loss.
The damping and delay of the inlet pressure oscillation with frequency, caused by the humidifier, is also influenced by the channel length. With increasing channel length, the characteristic feature gets shifted towards lower frequencies. This trend agrees with the observation of Zhang et al. [18].

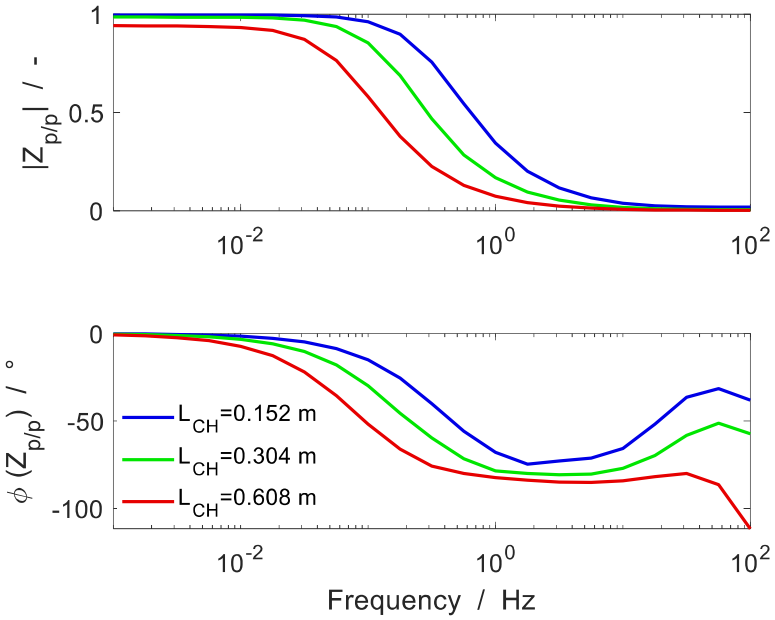

Figure 25: Bode plot of simulated spectra of the transfer function $Z_{p/p}$ between the inlet pressure oscillation and the outlet pressure excitation for different gas channel length (default value: L_{CH} = 0.304 m) at 0.2 A cm^{-2}.

To conclude, the sluggish pressure response of the fuel cell is caused by the big gas reservoir of the humidifier upstream the fuel cell. Additionally, the pressure dynamics are influenced by the channel length, which determines the distance between the gas reservoir and the location of pressure excitation.

5.1.1.2 Average pressure

In this subsection, the average pressure oscillation along the channel is analyzed in relation to the cathode outlet pressure excitation. The average total pressure response is of interest, because the cell voltage response is the sum of all pressure signals along the

channel. The approach of analyzing the average response of a quantity is repeated in the context of the molar fraction and partial pressure response in the subsequent chapters. The analyzed transfer function between the average total pressure response and the outlet pressure excitation $Z_{p(\mathrm{avg})/p}$ is calculated according to Eq. 72. The simulated spectra of the transfer function are shown in Figure 26 for different current densities. The progression of the magnitude is qualitatively similar compared to the magnitude of $Z_{p/p}$ (cf. Figure 23), because the same phenomena cause the characteristics, which are not repeated here. Quantitatively, the magnitude is different, because the average pressure oscillation is the mean value of the inlet pressure oscillation and the outlet pressure excitation. Because the amplitude of the inlet pressure oscillation approaches zero above 1 Hz, the magnitude in the figure below approaches 0.5 above 1 Hz.

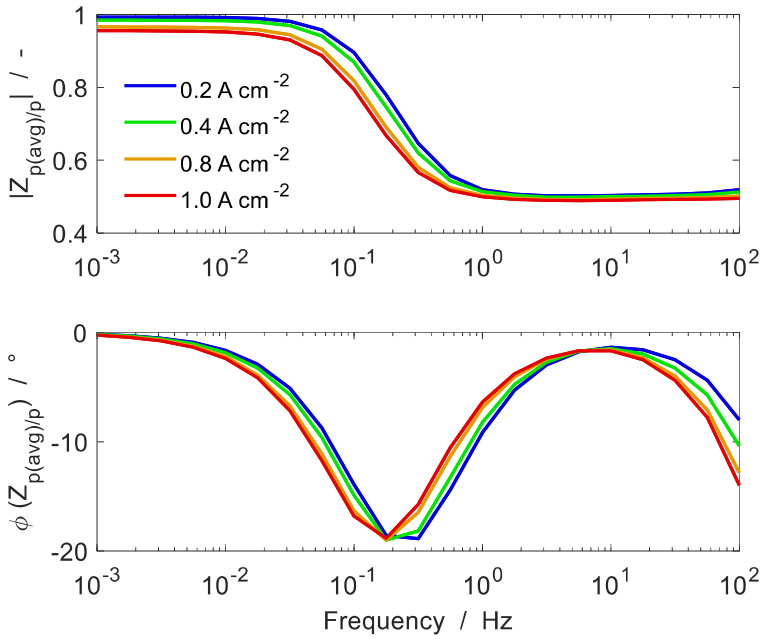

Figure 26: Bode plot of simulated spectra of the transfer function $Z_{p(\mathrm{avg})/p}$ between the average pressure oscillation along the gas channel and the outlet pressure excitation at different current densities.

The phase shift of the transfer function $Z_{p(\mathrm{avg})/p}$, shows a distinct minimum around 0.2 Hz, with a subsequent increase. The minimum can be explained as follows. First the phase shift of the average pressure oscillation decreases with frequency due to the delay of the pressure oscillation towards the inlet. The increased damping of the inlet pressure oscillation with frequency diminishes this effect. Because the amplitude of the outlet pressure oscillation remains constant, the average pressure oscillation approaches the oscillation of the outlet pressure. This leads to an increase of the phase shift above 0.2 Hz. Similar to the transfer function of $Z_{p/p}$, the characteristic progression of magnitude and phase get shifted towards lower frequencies with increasing current density.

5.1.2 Molar fraction

In this section, the frequency dependence of the species molar fraction oscillation along the channel is analyzed, by means of its average value along the gas channel. The transfer function $Z_{x(i,\mathrm{avg})/p}$ is introduced for this purpose, which describes the relationship between the average molar fraction oscillation of a species and the outlet pressure excitation according to Eq. 73.

First, the simulated molar fraction oscillations of the species oxygen and water are presented consecutively. Because the oscillation of molar fraction is surprising at first, the reason for this phenomenon is given afterwards by relating it to the oscillation of the inlet flow rate.

5.1.2.1 Oxygen

Figure 27 shows the spectra of the transfer function $Z_{x(\mathrm{O_2},\mathrm{avg})/p}$ between the average molar fraction oscillation of oxygen along the gas channel and the outlet pressure excitation for different current densities. At the lowest frequency, the magnitude tends to zero, which means that the average molar fraction of oxygen is constant during the pressure excitation. This agrees with the previous observation of the partial pressure oscillation following the total pressure oscillation at 1 mHz (cf. Figure 21).

With increasing frequency, the molar fraction of oxygen starts to oscillate with an increase of the amplitude until a frequency of ca. 0.5 Hz. This observation agrees with the interpretation of Figure 22, in which the partial pressure oscillation at 0.56 Hz is attributed to the oscillation of molar fraction. For frequencies above 0.5 Hz, the amplitude decreases and approaches again a magnitude of zero at 100 Hz. The increase of magnitude with frequency is more pronounced for lower current densities.

The phase shift shows a continuous decrease over the whole frequency range with a value of –200° at 1 Hz.

Qualitatively, the increase in magnitude below 1 Hz resembles the increase in magnitude observed for the transfer function $Z_{V/p}$ in the EPIS experiments of Zhang et al. [18] and Shirsath et al. [14–17] (cf. Figure 5). Furthermore, in the same frequency range, the continuous decrease in phase shift of $Z_{x(\mathrm{O_2},\mathrm{avg})/p}$ resembles the phase shift which was observed experimentally for the transfer function $Z_{V/p}$. Based on this similarity, the two EPIS features, of increasing magnitude and decreasing phase shift, can be perhaps traced back to the frequency dependence of the oxygen molar fraction oscillation.

Another similarity can be observed by comparing the spectra of the transfer function $Z_{V/p}$ of Engebretsen et al. [19] (cf. Figure 2) with the simulated spectra of $Z_{x(\mathrm{O_2},\mathrm{avg})/p}$ in the frequency range above 1 Hz. The magnitude of both transfer function shows qualitatively

the same behavior, which is a decrease towards zero. Furthermore, the phase shift seems to be also similar.

To further investigate this supposed connection between the cell voltage oscillation and the molar fraction oscillation of oxygen, the same characteristics of spectra have to be found in the partial pressure oscillation of oxygen, which are shown in Chapter 5.1.3.1.

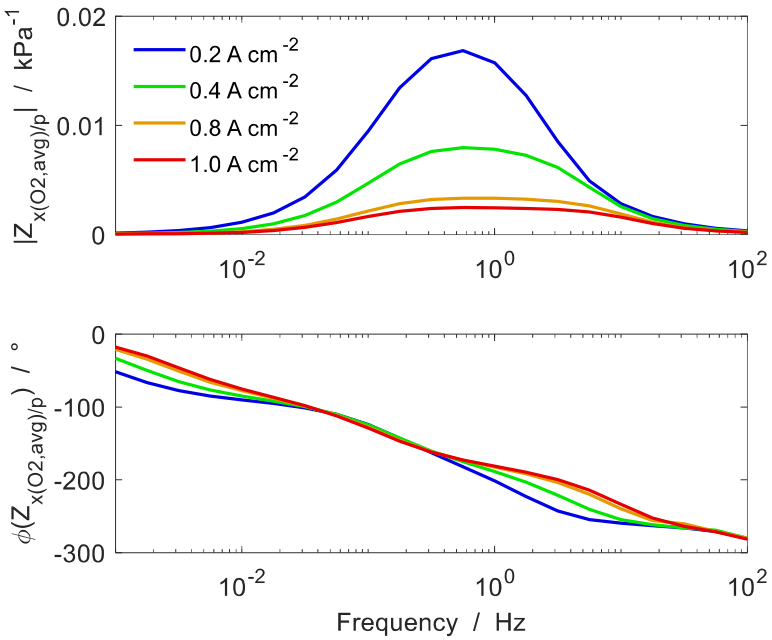

Figure 27: Bode plot of the simulated spectra of the transfer function $Z_{x(O_2,\mathrm{avg})/p}$ between the average molar fraction oscillation of oxygen along the gas channel and the outlet pressure excitation for different current densities.

5.1.2.2 Water

Figure 28 shows the spectra of the transfer function $Z_{x(\mathrm{H_2O,avg})/p}$ between the average molar fraction oscillation of water along the gas channel and the outlet pressure excitation for different current densities.

At the lowest frequency, the magnitude is small but not zero, which is the case for oxygen (cf. Figure 27). The molar fraction of water oscillates already at low frequencies, because of the boundary condition of constant water pressure at the channel inlet determined by the constant relative humidity. For an increase of total pressure, the molar fraction of water thus decreases. This argument is supported by the phase shift of 180° at 1 mHz, which means that the molar fraction of water oscillates in antiphase to the pressure oscillation. With increasing frequency, the magnitude increases similarly to the magnitude of oxygen, followed by a decrease towards zero.

The phase shift decreases with frequency in a similar manner as the phase shift of oxygen, with an offset of 180°.

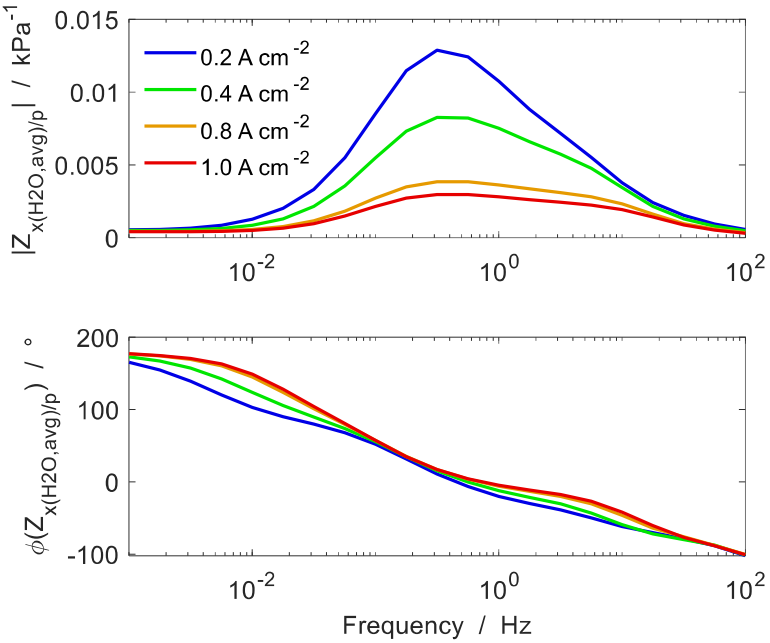

Figure 28: Bode plot of the simulated spectra of the transfer function $Z_{x(\mathrm{H_2O,avg})/p}$ between the average molar fraction oscillation of water along the gas channel and the outlet pressure excitation for different current densities

5.1.2.3 Influence of oscillating inlet flow rate

In this subsection, the reason for the counterintuitive molar fraction oscillation is given by relating it to the oscillating inlet flow rate. As the overall consumption and production of species per time under galvanostatic control is constant, the change in molar fraction is expected to originate from a change in the supply. Shirsath et al. [17] have observed that the air flow rate at the fuel cell inlet is varying during pressure excitation, even though the humidifier upstream the fuel cell is fed with a constant air flow rate. This is due to the gas volume in the humidifier, which acts as a gas reservoir with changing content for a change in pressure. First, the frequency dependence of the oscillating inlet flow rate is compared between the simulations and the approximation made by Shirsath et al. [17]. Afterwards, a simplified model is derived which allows the calculation of the molar fraction as a function of the inlet flow rate.

Shirsath et al. derived an expression for the oscillating inlet flow rate [17]. It is a harmonic function based on the transfer function $Z_{p/p}$ between inlet and outlet pressure:

$$\Delta Q_{\mathrm{CCH}}^{\mathrm{in}}(t) = -C\omega\left|Z_{p/p}\right|\hat{p}_{\mathrm{CCH}}^{\mathrm{out}}\cos\left(\omega t + \phi\left(Z_{p/p}\right)\right), \tag{95}$$

where Q is the flow rate and C a capacitive parameter proportional to the gas volume. It should be stressed here that Q describes the volumetric flow rate at standard conditions and thus has the unit of normal liter per seconds. The magnitude and phase shift of the transfer function $Z_{p/p}$ are

$$\left|Z_{p/p}\right| = \frac{1}{\sqrt{1+(rC\omega)^2}} \text{ and} \tag{96}$$

$$\phi\left(Z_{p/p}\right) = -\operatorname{atan}(rC\omega)\ , \tag{97}$$

where r is the pressure drop along the channel per flow rate.

In the PEMFC model used in the present work, the difference between the constant gas feed into the humidifier and the changing inlet flow rate is described by Eq. 54. To analyze the flow rate oscillation in the frequency domain an additional transfer function $Z_{Q/p}$ between the normal inlet flow rate and the outlet pressure is defined according to Eq. 75.

In Figure 29, the oscillating inlet flow rate, calculated with the approach of Shirsath et al. (cf. Eq. 95), is compared to the oscillating inlet flow rate, simulated with the PEMFC model used in this work, by means of the transfer function $Z_{Q/p}$. The flow rate in the enumerator is given in normal liter per seconds.

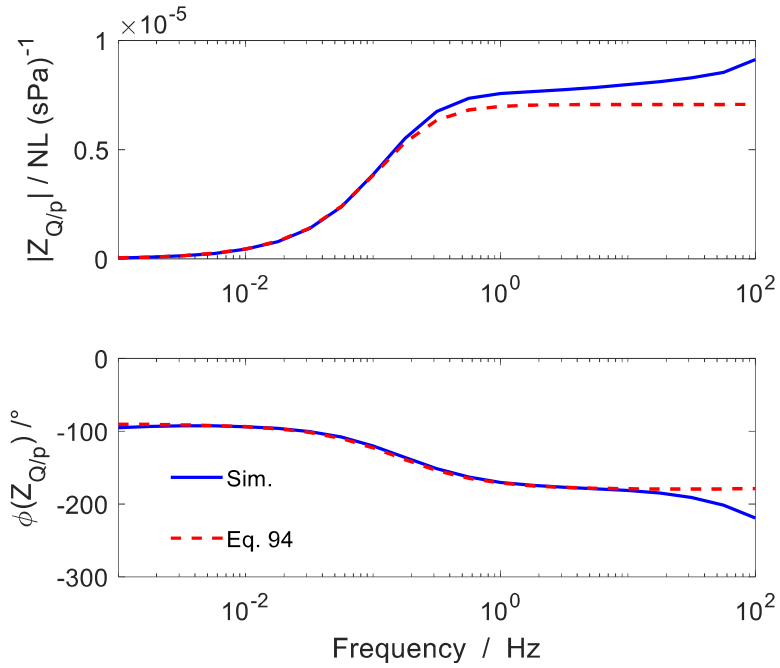

Figure 29: Bode plot of the spectra of the transfer function $Z_{Q/p}$ between the normal inlet flow rate oscillation and the outlet pressure excitation calculated with Eq. 95 and simulated with the present PEMFC model. The cell was operated at 0.2 A cm^{-2}. The flow rate corresponds to the total flow rate for all 23 channels.

The results of Eq. 95 and the simulated results show a good agreement, although there is a clear deviation in the magnitude above 0.1 Hz and in the phase shift above 10 Hz visible. The amplitude of the inlet flow rate oscillation is nearly zero at 1 mHz. Therefore, at the quasi-static frequency the gas flow rate at the fuel cell inlet is constant and corresponds to the defined stoichiometry. With increasing frequency, the inlet flow rate oscillates with an increasing amplitude. The reason for this phenomenon can be seen by reviewing Eq. 54. The change of the inlet mass flow rate is proportional to the change of density and hence to the change of the pressure inside the humidifier per time. In this context it should be stressed that the normal volumetric inlet flow rate is a measure of the actual molar flow rate, rather than a measure of the actual volumetric flow rate. Although the

amplitude of the inlet pressure oscillation decreases with frequency (cf. Figure 23), the change rate of the pressure per time increases, which leads to an increase of the inlet flow rate oscillation with frequency.

Above 1 Hz, the amplitude of inlet flow rate oscillations is constant for the calculation with Eq. 95, while the simulations show a further increase. The reason for this difference between both approaches is not understood.

Qualitatively, the increase of magnitude below 1 Hz is similar to the increase of magnitude of the transfer function $Z_{x(\mathrm{O_2,avg})/p}$ (cf. Figure 27). This similarity supports the hypothesis that the molar fraction oscillation of oxygen is caused by the oscillating inlet flow rate.

The phase shift of $Z_{Q/p}$ is close to –90° at the lowest frequency and decreases with frequency down to a plateau of about –180° above 1 Hz. This progression of phase shift can be explained by reviewing again Eq. 54. The change of the inlet flow rate is proportional to the time derivative of the density inside the humidifier, which again is proportional to the time derivative of the inlet pressure. Assuming that the inlet pressure oscillation can be described by a sine function, the inlet flow rate oscillation, being proportional to the time derivative of the inlet pressure, would have the progression of a cosine function, due to the derivative of the sine function. Compared to the harmonic oscillation of the inlet pressure, the phase shift of the inlet flow rate is therefore shifted by –90°. Based on this explanation, the phase shift of $Z_{Q/p}$ follows the phase shift of $Z_{p/p}$ with an offset of –90° (cf. Figure 23).

By comparing the phase shift in Figure 29 with the phase shift of the transfer function $Z_{x(i,\mathrm{avg})/p}$ (cf. Figure 27), the similarity becomes visible mainly in the frequency range between 0.03–0.5 Hz. Again, this similarity supports the hypothesis that the molar fraction oscillation of oxygen is caused by the oscillating inlet flow rate.

To prove the hypothesis that the oscillating inlet flow rate causes the oscillation of molar fraction, the relationship between both quantities needs to be determined. To this end, a model is derived in the following which allows the simplified calculation of the molar fraction as a function of the inlet flow rate.

The molar fraction of species i at position x can be expressed as the local ratio between the molar flow rate of species i and the total molar flow rate according to

$$x_{i,\mathrm{CCH}}(x,t) = \frac{\dot{n}_{i,\mathrm{CCH}}(x,t)}{\dot{n}_{\mathrm{CCH}}(x,t)} \ . \tag{98}$$

To express both quantities as a function of the inlet flow rate, a molar balance of the gas phase from the inlet to position x has to be made up.

For the sake of simplicity, the following assumptions are made. The molar balance considers only the consumption and production of species along the channel due to the ORR, in which water is assumed to be produced directly in the gas phase. The sorption of water is neglected. The reaction rate of the ORR along the channel is assumed to be constant. Furthermore, the duration which is needed for the gas to pass the channel is assumed to

be negligible, compared to the time period of one excitation wave. Thus, the change of the inlet flow is assumed to have an instant effect on the flow rate throughout the channel. Additionally, the inlet gas composition is assumed to be constant.

With these simplifications, the total molar flow rate at position x can be calculated as

$$\dot{n}_{\mathrm{CCH}}(x,t) = \dot{n}^{\mathrm{in}}_{\mathrm{CCH}}(t) - \dot{n}^{\mathrm{ORR}}_{\mathrm{O_2,CCH}}(x) + \dot{n}^{\mathrm{ORR}}_{\mathrm{H_2O,CCH}}(x) \ . \tag{99}$$

where $\dot{n}^{\mathrm{ORR}}_{\mathrm{O_2,CCH}}(x)$ is the molar rate of consumed oxygen and $\dot{n}^{\mathrm{ORR}}_{\mathrm{H_2O,CCH}}(x)$ the molar rate of produced water, due to the ORR from the channel inlet until position x.

With the species molar balance for oxygen, the molar flow rate of oxygen at position x is calculated as

$$\dot{n}_{\mathrm{O_2,CCH}}(x,t) = \dot{n}^{\mathrm{in}}_{\mathrm{CCH}}(t) x^{\mathrm{in}}_{\mathrm{O_2,CCH}} - \dot{n}^{\mathrm{ORR}}_{\mathrm{O_2,CCH}}(x) \ . \tag{100}$$

Analogue, the molar flow rate of water at position x is calculated as

$$\dot{n}_{\mathrm{H_2O,CCH}}(x,t) = \dot{n}^{\mathrm{in}}_{\mathrm{CCH}}(t) x^{\mathrm{in}}_{\mathrm{H_2O,CCH}} + \dot{n}^{\mathrm{ORR}}_{\mathrm{H_2O,CCH}}(x) \ . \tag{101}$$

The inlet flow rate is calculated as the sum of the constant molar flow rate into the humidifier $\dot{n}_{\mathrm{feed}}$ and the oscillating inlet flow rate out of the humidifier:

$$\dot{n}^{\mathrm{in}}(t) = \dot{n}_{\mathrm{feed}} + \Delta Q^{\mathrm{in}}_{\mathrm{CCH}}(t) \frac{p_{\mathrm{N}}}{R T_{\mathrm{N}}} \ . \tag{102}$$

The oscillating inlet flow rate is calculated by the use of Eq. 95 and needs to be converted from normal volume flow into molar flow, with the standard pressure p_{N} = 101 325 Pa and standard temperature T_{N} = 273.15 K.

The consumption of oxygen due to the ORR from the inlet until position x is

$$\dot{n}^{\mathrm{ORR}}_{\mathrm{O_2,CCH}}(x) = \frac{I(x)}{4F} \ . \tag{103}$$

Analogue, the production of water from the inlet until position x is

$$\dot{n}^{\mathrm{ORR}}_{\mathrm{H_2O,CCH}}(x) = \frac{I(x)}{2F} \ . \tag{104}$$

With the assumption of constant current density along the channel, the produced current until position x is

$$I(x) = i_{\mathrm{cell}} A_{\mathrm{FC}} \frac{x}{L_{\mathrm{CH}}} \ . \tag{105}$$

In case of oxygen as the species of interest, the molar fraction at position x can be approximated as a function of the oscillating inlet flow rate through the use of Eq. 98-105 according to

$$x_{\mathrm{O_2,CCH}}(x,t) = \frac{x^{\mathrm{in}}_{\mathrm{O_2,CCH}} \left(\dot{n}_{\mathrm{feed}} + \Delta Q^{\mathrm{in}}_{\mathrm{CCH}}(t) \frac{p_{\mathrm{N}}}{R T_{\mathrm{N}}} \right) - \frac{i_{\mathrm{cell}} A_{\mathrm{FC}}}{4F} \frac{x}{L_{\mathrm{CH}}}}{\dot{n}_{\mathrm{feed}} + \Delta Q^{\mathrm{in}}_{\mathrm{CCH}}(t) \frac{p_{\mathrm{N}}}{R T_{\mathrm{N}}} + \frac{i_{\mathrm{cell}} A_{\mathrm{FC}}}{4F} \frac{x}{L_{\mathrm{CH}}}} \ . \tag{106}$$

With this relation, it is now possible to approximate the effect of the oscillating inlet flow rate on the molar fraction of oxygen along the channel.

Figure 30 shows the spectra of the transfer function $Z_{x(\mathrm{O_2,avg})/p}$ between the average molar fraction oscillation of oxygen along the gas channel and the outlet pressure oscillation at a current density of 0.2 A cm^{-2}. The spectra of the dashed line represent the transfer

function in which the oxygen molar fraction is calculated by the use of Eq. 106. The solid lines represent the simulated results which are also shown in Figure 27 above.

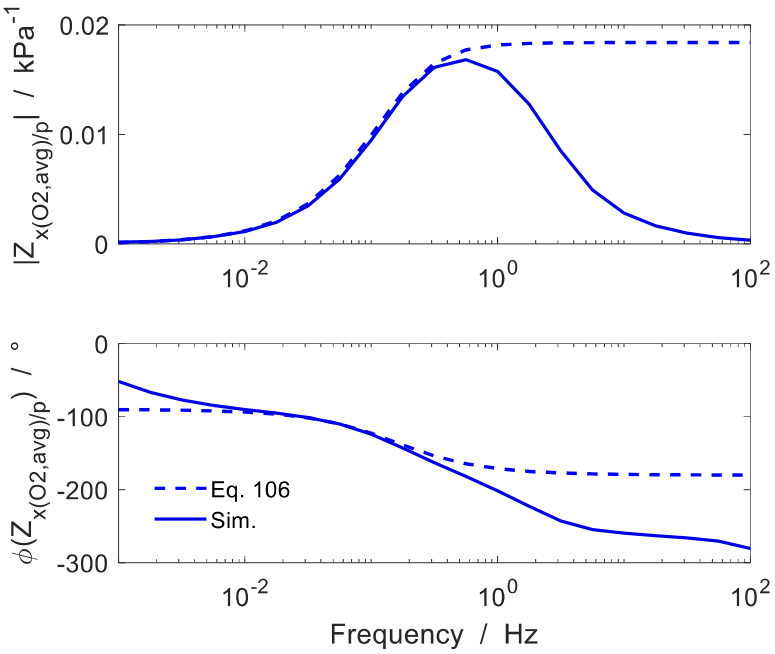

Figure 30: Bode plot of the spectra of the transfer function $Z_{x(\mathrm{O_2,avg})/p}$ between the average molar fraction oscillation of oxygen along the gas channel and the outlet pressure excitation for a current density of 0.2 A cm^{-2}. The molar fraction of oxygen was calculated with the simplified approximation of Eq. 106 (dashed line). The required oscillating inlet flow rate was calculated by the use of Eq. 95. The results of the simulated transfer function (solid line) are also shown in Figure 27.

The magnitude of the dashed line shows an increase from zero at the lowest frequency up to 1 Hz. Above 1 Hz, the magnitude remains constant. Comparing this progression of magnitude with simulated magnitude of the same transfer function shows their striking similarity below 1 Hz. This proves that the increase of oxygen molar fraction oscillation with frequency can be traced back to the inlet flow rate oscillation. Above 1 Hz, the simulation shows a decrease of the magnitude towards zero at 100 Hz, which cannot be seen in the approximation through Eq. 106.

Taking a look at the phase shift of the dashed line reveals a decrease from −90° at 1 mHz to -180° around 1 Hz. Above 1 Hz, the phase shift remains −180°. The comparison with the simulated phase shift of the same transfer function, again, reveals a good agreement below 1 Hz, but diverges for frequencies above.

To conclude, the surprising increase of molar fraction oscillation along the gas channel observed in the simulations can be traced back to the oscillating inlet flow rate. Furthermore, the phase shift of the molar fraction oscillation of −180° around 1 Hz can also be traced back to the inlet flow rate oscillations. The observed phenomena of the simulations of $Z_{x(\mathrm{O_2,avg})/p}$ above 1 Hz cannot be explained with the simplified relationship between the molar fraction and the inlet flow rate. One possible reason may be that towards higher

frequencies, the duration of the gas transport through the gas channel is having an effect on the local molar fraction, which is neglected in the described approach of the simple model.

5.1.3 Partial pressure

In this section, the partial pressure oscillation of oxygen and water is analyzed in the frequency domain, by means of the transfer function $Z_{p(i,\mathrm{avg})/p}$ between the average partial pressure oscillation of species i along the channel and the outlet pressure excitation (see. Eq. 74). To work out the contribution of the previously analyzed total pressure oscillation and molar fraction oscillation to the partial pressure oscillation, the following relationship will be used. According to the derivative of the partial pressure in Eq. 94, the transfer function $Z_{p(i,\mathrm{avg})/p}$ can be expressed as the sum of the previously analyzed transfer functions of the total pressure $Z_{p(\mathrm{avg})/p}$ and the molar fraction $Z_{x(i,\mathrm{avg})/p}$ according to

$$Z_{p(i,\mathrm{avg})/p} = \bar{x}_i Z_{p(\mathrm{avg})/p} + \bar{p} Z_{x(i,\mathrm{avg})/p} \ . \tag{107}$$

For the two species oxygen and water, a comparison of the sum on the left side together with the summands on the right side of the equation above is shown in Chapters 5.1.3.1 and 5.1.3.2, respectively. Furthermore, for both species the partial pressure oscillation is analyzed at different current densities.

5.1.3.1 Oxygen

Figure 31 shows the composition of the transfer function of the average partial pressure oscillation of oxygen along the channel according to Eq. 107. At the lowest frequency, the transfer function $Z_{p(\mathrm{O_2,avg})/p}$ equals the transfer function $Z_{p(\mathrm{avg})/p}$ multiplied by the average oxygen molar fraction, in both magnitude and phase. This means that the partial pressure oscillation is equal to the total pressure oscillation reduced by the molar fraction, which has already been observed in the analysis of the partial pressure oscillations in the time domain (cf. Figure 21).

With increasing frequency, the molar fraction of oxygen starts to oscillate due to the oscillation of the inlet flow rate and contributes to the partial pressure oscillation of oxygen. Above 10 mHz, the partial pressure oscillation of oxygen gets increasingly dominated by the oscillation of the molar fraction, which leads to the characteristic increase up to the maximum around 0.5 Hz.

The transition of the partial pressure oscillation from being dominated by the total pressure oscillation to being dominated by the molar fraction oscillation can also be seen by the phase shift. At the lowest frequency, the phase shift of the partial pressure oscillation corresponds to the phase shift of the total pressure oscillation. With increasing frequency, the phase shift of the partial pressure oscillation decreases and approaches the phase shift of the molar fraction oscillation.

Around 0.5 Hz, the oscillation of the molar fraction and the total pressure are nearly in antiphase, which agrees with the observation in the analysis of the partial pressure oscillations in the time domain (cf. Figure 22). The antiphase is the reason why the maximum magnitude of the partial pressure oscillation is slightly below the maximum of the molar fraction oscillation multiplied by the average total pressure.

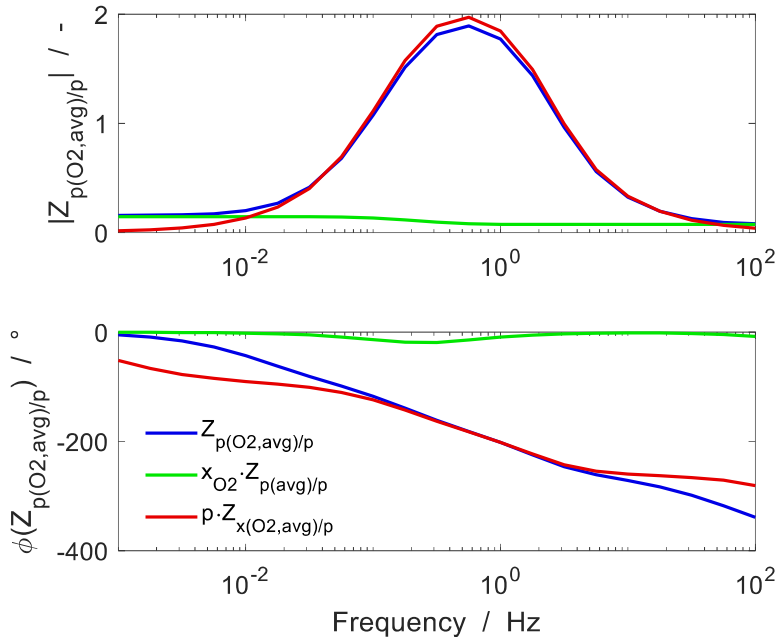

Figure 31: Bode plot of the simulated spectra of the transfer function $Z_{p(\mathrm{O_2,avg})/p}$ between the average partial pressure oscillation of oxygen along the channel and the outlet pressure excitation at 0.2 A cm^{-2} (blue line). Additionally, the two summands of Eq. 107 are shown for the species oxygen. The first summand (green line) contains the transfer function $Z_{p(\mathrm{avg})/p}$ between the average total pressure oscillation along the channel and the outlet pressure excitation (cf. Figure 26). The second summand (red line) contains the transfer function $Z_{x(\mathrm{O_2,avg})/p}$ between the average molar fraction oscillation of oxygen along the channel and the outlet pressure excitation (cf. Figure 27).

Above 0.5 Hz, the magnitude of the partial pressure oscillation is decreasing due to the decrease of the magnitude of the molar fraction oscillation. As the amplitude of the molar fraction oscillation tends to zero at 100 Hz, the influence of the total pressure oscillation on the partial pressure oscillation becomes visible again.

Comparing the transfer function for the simulated average oxygen pressure response with the transfer function of the experimental cell voltage response (cf. Figure 5) in the common frequency range between 1 mHz – 1 Hz reveals a qualitative agreement in case of the magnitude and a quantitative agreement in case of the phase shift. From this observation, one can deduce that the cell voltage response is dominated by the oxygen pressure response. To further prove this assumption, the simulated cell voltage response is analyzed afterwards in Chapter 5.2.

Figure 32 shows the transfer function $Z_{p(O_2,avg)/p}$ at different current densities. The progressions of magnitude and phase shift have already been discussed in detail for a current density of 0.2 A cm^{-2} in the context of Figure 31 above.
With increasing current density, the increase of magnitude gets less pronounced. The reason for this observation is the decrease of the molar fraction oscillation with current density (cf. Figure 27).

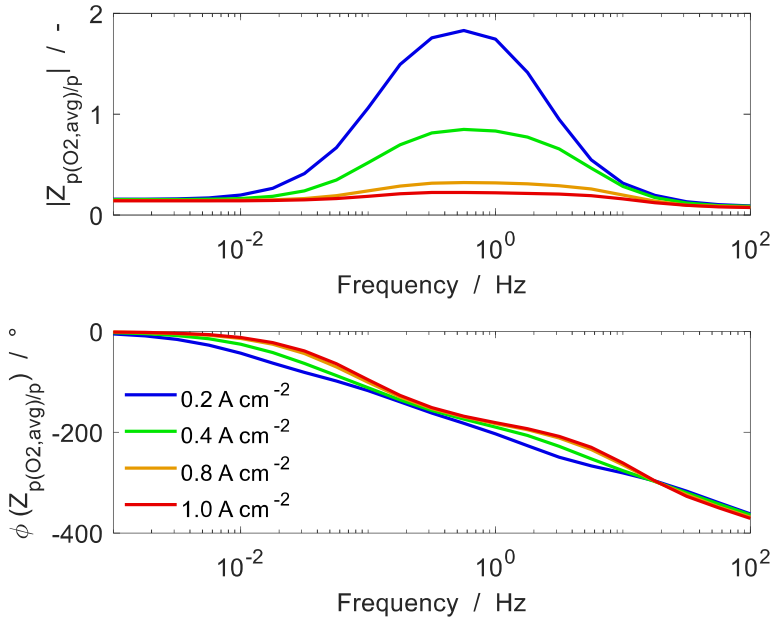

Figure 32: Bode plot of the simulated spectra of the transfer function $Z_{p(O_2,avg)/p}$ between the average partial pressure oscillation of oxygen along the channel and the outlet pressure excitation at different current densities.

In case of the phase shift, this means that the transition of the partial pressure oscillation from being dominated by the total pressure oscillation to being dominated by the molar fraction oscillation is shifted towards higher frequencies. Therefore, the decrease in phase shift below 0.1 Hz is less for higher current densities.
The spectra shown in Figure 32 are similar to the published spectra of a similar transfer function in Schiffer et al. [28]. The difference is that in the publication, the average of the partial pressure oscillation was calculated along the CL compared to the average along the gas channel here. The similarity reveals that the pressure response is rather dominated by the gas channel than by the GDL or CL.

5.1.3.2 Water

Figure 33 shows the composition of the transfer function of the average partial pressure oscillation of water along the channel according to Eq. 107. At the lowest frequency, the partial pressure oscillation of water mainly follows the oscillation of the total pressure, which can be seen by the common phase shift of 0°.

The oscillation of the molar fraction of water is in antiphase with the total pressure oscillation and other than the oscillation of the molar fraction of oxygen already present at 1 mHz (cf. Figure 31). The reason is explained in Chapter 5.1.2.2.
With increasing frequency, the increase of the oscillating inlet flow rate causes an increase of the molar fraction oscillation of water, similar to oxygen. The phase shift of the molar fraction oscillation of water is different to oxygen, which seems to be shifted by 180° (cf. Figure 31).

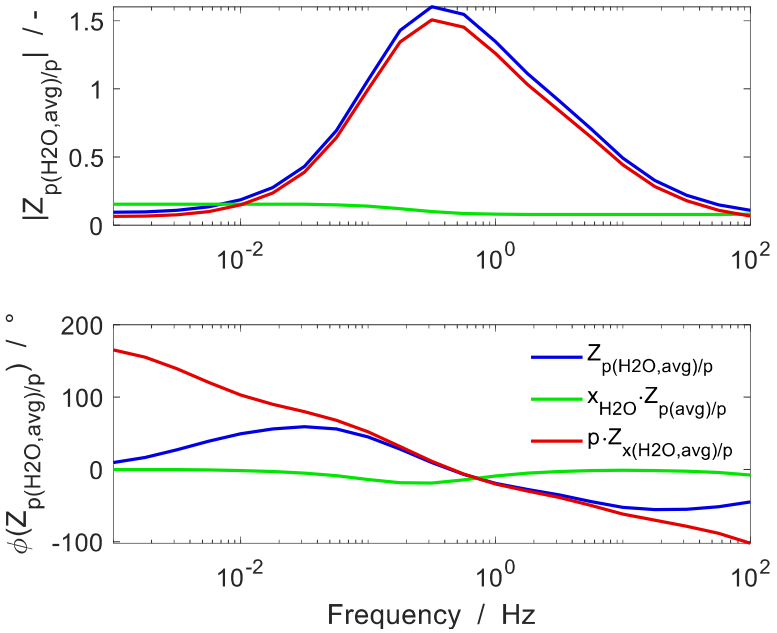

Figure 33: Bode plot of the simulated spectra of the transfer function $Z_{p(\mathrm{H_2O,avg})/p}$ between the average partial pressure oscillation of water along the channel and the outlet pressure excitation at 0.2 A cm^{-2} (blue line). Additionally, the two summands of Eq. 107 are shown for the species water. The first summand (green line) contains the transfer function $Z_{p(\mathrm{avg})/p}$ between the average total pressure oscillation along the channel and the outlet pressure excitation (cf. Figure 26). The second summand (red line) contains the transfer function $Z_{x(\mathrm{H_2O,avg})/p}$ between the average molar fraction oscillation of water along the channel and the outlet pressure excitation (cf. Figure 28).

Similar to oxygen, above 10 mHz, the partial pressure oscillation is dominated by the molar fraction oscillation. The transition of the partial pressure oscillation from being dominated by the total pressure oscillation at low frequency to being dominated by the molar fraction oscillation above 10 mHz can be seen by the phase shift.
The magnitude of $Z_{p(\mathrm{H_2O,avg})/p}$ reaches a maximum slightly before 0.5 Hz and shows a subsequent decrease. The decrease of magnitude seems to be qualitatively different to the decrease of magnitude of $Z_{p(\mathrm{O_2,avg})/p}$. The reason is not understood.
Comparing the transfer function for the simulated average water pressure response with the transfer function of the experimental cell voltage response in the common frequency range between 1 mHz – 1 Hz reveals a qualitative agreement in case of the magnitude but

a discrepancy in case of the phase shift. From this observation, it can be deduced that the dynamic cell voltage response above 10 mHz is rather dominated by the oxygen pressure response than by the water pressure response. This assumption is supported by the argument that the change of electrolyte conductivity with water pressure is relatively slow due to the finite velocity of the water uptake by the PEM (see Chapter 7.2). Therefore, the influence of water pressure on the cell voltage becomes less visible towards higher frequencies.

Figure 34 shows the transfer function $Z_{p(\mathrm{H_2O,avg})/p}$ for different current densities. The progressions of magnitude and phase for a current density of 0.2 A cm^{-2} have already been discussed in detail in the context of Figure 33 above. With increasing current density, the increase of magnitude is less pronounced. The reason for this observation is due to a decrease of the molar fraction oscillation with current density.

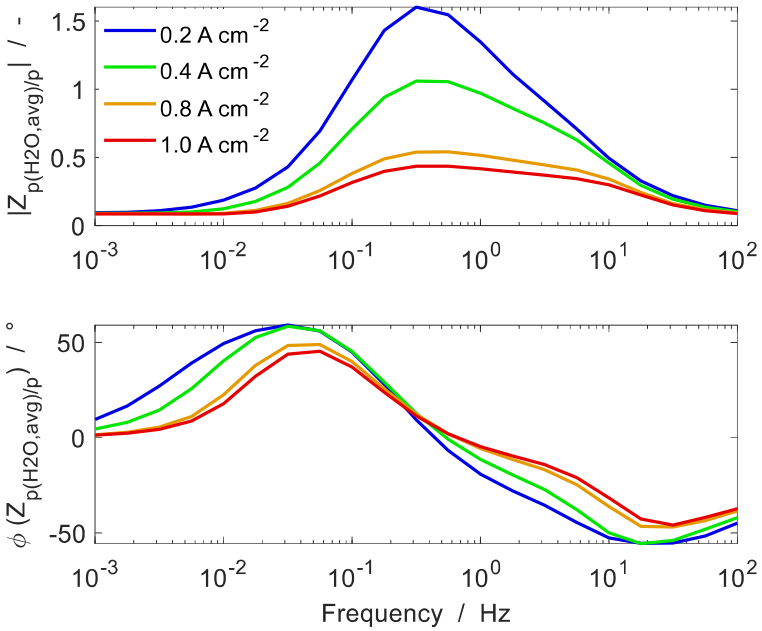

Figure 34: Bode plot of the simulated spectra of the transfer function $Z_{p(\mathrm{H_2O,avg})/p}$ between the average partial pressure oscillation of water along the channel and the outlet pressure excitation at different current densities.

5.2 Voltage response

After the extensive analysis of the pressure response of the fuel cell to the pressure excitation in the preceding chapter, the actual EPIS signal, which is the cell voltage response, is analyzed in the following. The appropriate transfer function describing the relationship between the cell voltage oscillation and the pressure excitation is $Z_{V/p}$ (see Eq. 2).

Figure 35 shows a comparison of simulated and experimental EPIS spectra operated with air as the cathode gas feed at 0.2 A cm^{-2}. The dedicated current density study is presented

in Chapter 6.1.1. The experiment was conducted up to a frequency of 1 Hz, while the simulation was extended up to 100 Hz.

The magnitude of $Z_{V/p}$ for the experiment shows a nearly constant value below 10 mHz, followed by an increase with frequency up to a maximum around 0.5 Hz. The phase shift of the experiment shows a continuous decrease from 0° at 1 mHz down to −200° at 1 Hz. These two features are typically observed if the fuel cell is operated with air as the cathode gas feed (see Chapter 2.2).

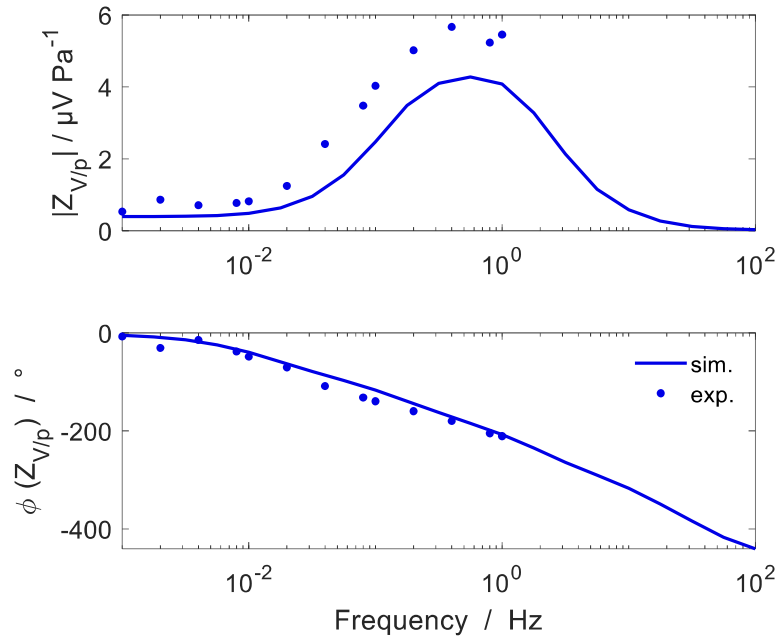

Figure 35: Bode plot of typical spectra of the transfer function $Z_{V/p}$ between the cell voltage response and the outlet pressure excitation for operation with air. Comparison of simulated (solid lines) and experimental (circles) spectra at 0.2 A cm^{-2}. The figure is adapted from Schiffer et al. [28].

The comparison of the simulated spectra with the experimental spectra reveals that the quasi-static magnitude and the two features are well captured by the simulation, which shows the ability of the model to reproduce the experimentally observed EPIS results at the analyzed current density.

The simulated quasi-static magnitude approaches the value of the static cell voltage response for a change of the outlet pressure (cf. Figure 20). Based on the similarity of the magnitude and phase shift at 1 mHz, the experiments are expected to approach the static response as well. Furthermore, the static analysis in Chapter 4.5 has shown that the cell voltage is affected by a change of the partial pressure of oxygen, through the equilibrium potential and through the reaction kinetics at the cathode and by a change of the partial pressure of water through the membrane conductivity.

To see how the dynamic cell voltage response is related to the partial pressure of oxygen and water, subsequently the quantities are compared in the frequency domain. The

comparison of the spectra of the cell voltage response in Figure 35 with the spectra of the partial pressure response of oxygen in Figure 31 reveals the strong similarity of the magnitude and the phase shift. This observation shows that the dynamic cell voltage response is closely related to the average oxygen pressure response.

Comparing the spectra of the cell voltage response with the spectra of the partial pressure response of water in Figure 33 reveals a similarity for the magnitude but a discrepancy for the phase shift. Because the change of the electrolyte conductivity with water pressure is relatively slow (see Chapter 7.2), the water pressure is expected to influence the cell voltage therefore only at low frequencies.

Based on the finding that the dynamic cell voltage response is dominated by the partial pressure response of oxygen, the relationship between both quantities is discussed quantitatively in the following. The relationship between the change of the cell voltage and the change of oxygen pressure is described by means of the cathode equilibrium potential in Eq. 77 and by means of the cathode overpotential in Eq. 81. These two equations can be converted to the sum of the derivative of both quantities with respect to the partial pressure of oxygen according to

$$\frac{\partial \Delta\phi_{\mathrm{C}}^{\mathrm{eq}}(x)}{\partial p_{\mathrm{O_2,CCL}}(x)} + \frac{\partial \eta_{\mathrm{C}}(x)}{\partial p_{\mathrm{O_2,CCL}}(x)} = \frac{RT}{F}\frac{1}{p_{\mathrm{O_2,CCL}}(x)}\left(\frac{1}{4} + \frac{0.54}{\alpha_{\mathrm{C}}}\right) \quad . \tag{108}$$

From this equation one can see that the change of the equilibrium potential and the overpotential at the cathode with the oxygen pressure are proportional to the reciprocal of the oxygen pressure. The average value of both quantities can be calculated with the simulated average oxygen pressure in the CL of $\bar{p}_{\mathrm{O_2,CCL}}$ = 17 311 Pa at 0.2 A cm^{-2} according to

$$\frac{\partial \Delta\bar{\phi}_{\mathrm{C}}^{\mathrm{eq}}}{\partial \bar{p}_{\mathrm{O_2,CCL}}} + \frac{\partial \bar{\eta}_{\mathrm{C}}}{\partial \bar{p}_{\mathrm{O_2,CCL}}} = \frac{RT}{F}\frac{1}{\bar{p}_{\mathrm{O_2,CCL}}}\left(\frac{1}{4} + \frac{0.54}{\alpha_{\mathrm{C}}}\right) = 1.97\ \mu\mathrm{V\ Pa^{-1}} \quad . \tag{109}$$

As a comparison to this value the ratio between the maximum magnitude of $Z_{V/p}$ (cf. Figure 35) and the maximum magnitude of $Z_{p(\mathrm{O_2,avg})/p}$ (cf. Figure 31) at 0.56 Hz is

$$\frac{|Z_{V/p}(0.56\ \mathrm{Hz})|}{|Z_{p(\mathrm{O_2,avg})/p}(0.56\ \mathrm{Hz})|} = \frac{4.28\ \mu\mathrm{V\ Pa^{-1}}}{1.83} = 2.34\ \mu\mathrm{V\ Pa^{-1}} \quad . \tag{110}$$

The similarity of the values in Eq. 109 and Eq. 110 proves that the dynamic cell voltage response is mainly influenced by the oxygen pressure response.

With the dominant influence of the oxygen pressure on the dynamic cell voltage response, the typical feature of the transfer function $Z_{V/p}$ can be explained with the same reasons given for the feature of the transfer function $Z_{p(\mathrm{O_2,avg})/p}$. Therefore, the increase of magnitude and the continuous decrease of phase shift with the excitation frequency can be stated to be caused by the oscillating inlet flow rate.

Above 1 Hz, the simulations reveal a further decrease of magnitude towards 0 µV Pa^{-1} at 100 Hz, which is only indicated by the present experiments. In the same frequency range, the simulated phase shift decreases further below –400° at 100 Hz. The same trend in magnitude and phase shift above 1 Hz was observed by Engebretsen et al [19].

Unfortunately, the similar decrease in magnitude and phase shift of $Z_{p(O_2,avg)/p}$ cannot be explained with the oscillating inlet flow rate. The reason for this phenomenon is not understood and remains unknown.

5.3 Conclusion

The present PEMFC model can accurately reproduce the EPIS experiments at the analyzed current density of 0.2 A cm^{-2} for an operation with air. The origin of typically observed EPIS features can be traced back to the partial pressure response of oxygen and water.
At the quasi-static frequency, the cell voltage is in phase with the pressure excitation and the magnitude approaches the static pressure-voltage response. Thus, the information of the quasi-static magnitude can also be obtained by simply analyzing the static pressure-voltage response. The static analysis in Chapter 4.5 has demonstrated that the cathode equilibrium potential and the reaction kinetics increase with oxygen pressure, while the conductivity of the membrane increases with water pressure.
With increasing frequency, the amplitude of the cell voltage oscillation increases, while its phase gets shifted in relation to the phase of the pressure excitation towards −200° at 1 Hz. The cell voltage oscillation strongly correlates with the oxygen pressure oscillation, which reveals a similar increase of amplitude and decrease of phase shift with frequency. The relationship between the cell voltage and oxygen pressure response can be approximated mathematically based on the model equations. The influence of the water pressure on the cell voltage response disappears towards higher frequencies, due to the limited speed of water uptake by the membrane. Thus, at the frequency of the maximum magnitude of about 1 Hz, the influence of the oxygen pressure on the cell voltage is separated from the influence of the water pressure.
The increase of the amplitude and the decrease of phase shift of the partial pressure oscillation are caused by the oscillation of the inlet flow rate. The partial pressure and the inlet flow rate are related to each other by the molar fraction. The molar fraction can be approximated as a function of the inlet flow rate with a simple model that considers the consumption and production of species along the gas channel. The oscillating inlet flow rate is an effect of the pressure changes in the gas phase of the humidifier, which is amplified with increasing frequency.
Therefore, the reason for the increase of the cell voltage oscillation with frequency can be traced back to the increase of the inlet flow rate oscillation. Furthermore, the phase shift of the cell voltage oscillation approaches the phase shift of the inlet flow rate oscillation with increasing frequency.
The decrease of the cell voltage oscillation visible in the extended frequency range of the simulations above 1 Hz cannot be explained with the previous argument, because the inlet

flow rate oscillation does not decrease above 1 Hz. The reason for this behavior remains unknown.

6 EPIS (2): Influence of parameters

In this chapter, the second part of the EPIS study is described, which is the analysis of the influence of operational and structural fuel cell parameters on the transfer function $Z_{V/p}$. The goal is to deepen the understanding of the dependence of the EPIS results on the respective parameters, using the findings obtained in the previous chapter.
The simulated results are compared to the experiments directly where available, or indirectly by referring to experimentally observed trends of relevant publications. The experimental data used for a direct comparison was provided by the project partner. The parameters are changed on the base of their default value, which corresponds to the spectra shown and discussed in Chapter 5.2.

6.1 Operational parameters

The changed operational parameters comprise the cell current density, the oxygen stoichiometry and the cathode gas feed composition.

6.1.1 Current density

Figure 36 shows simulated and experimental EPIS results at four different current densities between 0.2–1.0 A cm^{-2}. The results at 0.2 A cm^{-2} correspond to the default value of the current density. In the present experiments and simulations, the increase of current density is accompanied by an increase of the inlet flow rate, so that the stoichiometry remains constant. The experimental data is available up to a frequency of 1 Hz, while the simulations were extended up to 100 Hz.
First, the dependence of the quasi-static magnitude on the current density is discussed. The experiments reveal an increase of the quasi-static magnitude with current density, from 0.5 µV Pa^{-1} at 0.2 A cm^{-2} up to 1.8 µV Pa^{-1} at 1.0 A cm^{-2}. Qualitatively, this trend of increasing quasi-static magnitude with current density was also observed in the experiments of Zhang et al. [18] and Engebretsen et al. [19].
Comparing the quasi-static magnitude of the experiments with the simulation reveals a good agreement at a current density of 0.2 A cm^{-2}. The trend of increasing magnitude with current density can be captured by the simulation, but the increase is less pronounced with an increase from 0.4 µV Pa^{-1} at 0.2 A cm^{-2} up to 1.0 µV Pa^{-1} at 1.0 A cm^{-2}.
Reviewing the results of the static pressure-voltage response (cf. Figure 19) shows the similarity with the quasi-static cell voltage response at the same current densities. This observation confirms the previous hypothesis that the quasi-static magnitude approaches the static pressure-voltage response.

Based on the analysis of the composition of the static pressure-voltage response (see Figure 20), it is hypothesized that the increase of quasi-static magnitude with current density is related to the increased change of the potential difference across the electrolyte with pressure. The increased change of the potential difference across the electrolyte is caused by its proportionality to the current density (cf. Eq. 86).

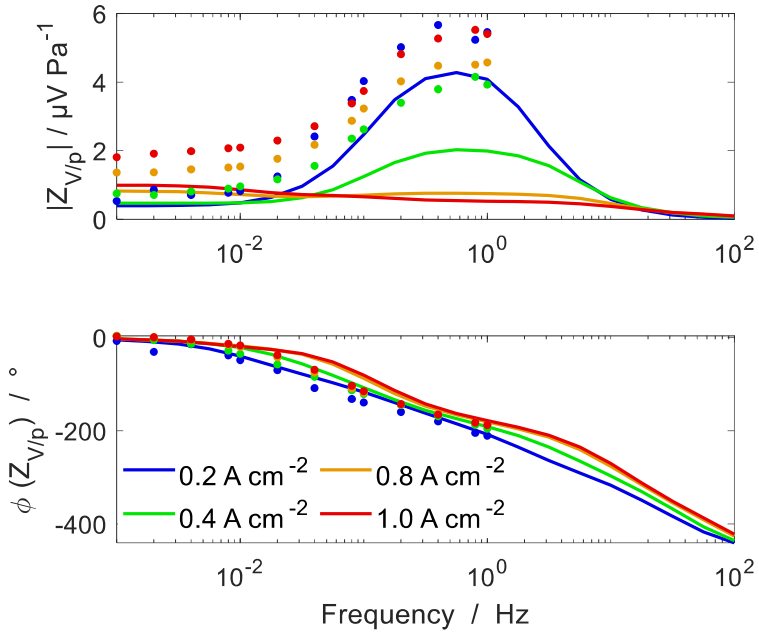

Figure 36: Bode plot of simulated (solid lines) and experimental (circles) spectra of the transfer function $Z_{V/p}$ between the cell voltage oscillation and the outlet pressure excitation at different current densities. The figure is adopted from Schiffer et al. [28].

Furthermore, the static analysis showed that the simulated change of the cathode potential with pressure, which comprises the change of the equilibrium potential and the overpotential, is relatively independent of the current density. A reason for the difference between the quasi-static magnitude of the simulation and the experiments towards higher current densities may be that in the experiments, the change of the overpotential with pressure is actually more sensitive to a change in current density.

Subsequently, the dependence of the progression of magnitude on the current density is analyzed. In the experiments, the characteristic increase of magnitude with frequency is visible for all current densities. The increase of magnitude with frequency is most distinct for the lowest analyzed current density of 0.2 A cm^{-2} and less pronounced towards higher current densities.

For the simulated spectra, the increase of magnitude with frequency is also most pronounced at the lowest current density, where it shows a good agreement with the experiments. However, with increasing current density, the increase of magnitude with frequency shrinks and is already vanished for a current density of 0.8 A cm^{-2}, where it shows a qualitative different progression than the experiments.

In Chapter 5, the characteristic increase of magnitude with frequency has been related to the increase of the partial pressure oscillation of oxygen. The dependence of the oxygen pressure oscillation on the current density (see Figure 32) has revealed that the increase of amplitude is less pronounced for higher current densities and nearly vanishes at 1.0 A cm^{-2}. This is the reason why the simulated maximum magnitude of $Z_{V/p}$ decreases dramatically with current density.

At 1.0 A cm^{-2}, the simulated magnitude of $Z_{V/p}$ even decreases in the frequency range below 1 Hz. This is probably due to the fact that change of the potential difference across the electrolyte with pressure, which dominates the change of the cell voltage at 1 mHz, is expected to decrease with frequency, because the change of the electrolyte conductivity with water pressure is relatively slow (see Chapter 7.2).

Taking a look at the phase shift at the different current densities shows in case of the experiments a slight trend of less decrease with increasing current density. This trend is similar for the simulations, but more distinct.

In Chapter 5, the phase shift of $Z_{V/p}$ was related to the phase shift of $Z_{p(\mathrm{O_2,avg})/p}$, which shows quite the same progression and hence the same dependence on the current density (see Figure 32). The explanation for this trend can be found in the corresponding interpretation of Figure 32.

6.1.2 Stoichiometry

In the following section, the influence of the oxygen stoichiometry on the EPIS results is analyzed. Figure 37 shows experimental EPIS results of Shirsath et al. [16] for three different stoichiometries obtained at 0.2 A cm^{-2}.

The quasi-static magnitude can be stated as independent of the stoichiometry. The increase of the magnitude with frequency is strongly amplified for a reduction of the oxygen stoichiometry from the default value of 2.5 down to 1.5, which leads to a maximum magnitude of 27 µV Pa^{-1}. According to this trend, the increase of the stoichiometry leads to a decrease of the maximum magnitude. The influence of the stoichiometry on the phase shift is more distinct below 0.1 Hz. In this frequency range, the decrease of stoichiometry has the effect that the phase shift is offset towards more negative values. Inversely, the increase of the stoichiometry leads to a delay of the phase shift towards higher frequencies.

The authors relate these trends of magnitude and phase shift to diffusion phenomena. Subsequently, a different explanation for the observed trends is given.

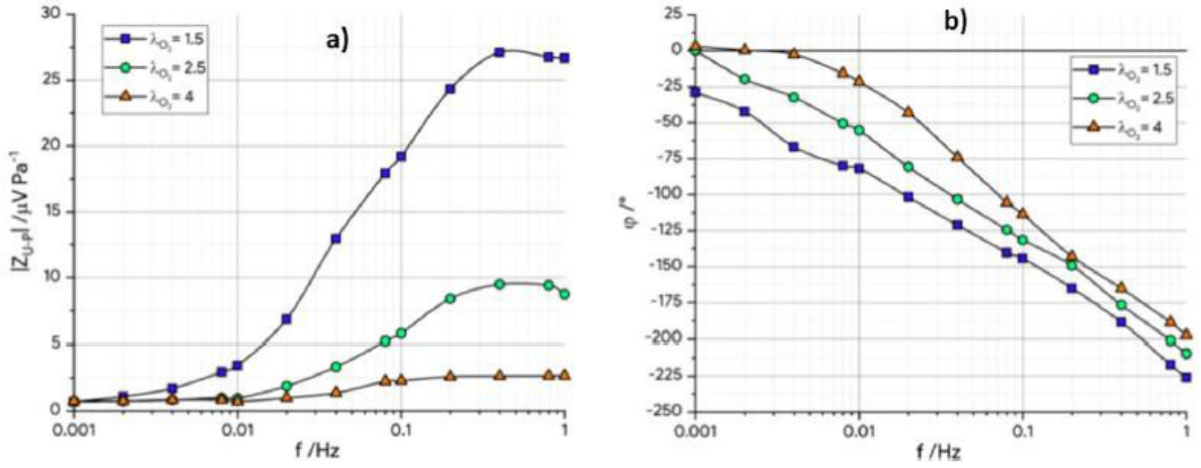

Figure 37: Bode plot of experimental spectra of the transfer function $Z_{V/p}$ between the cell voltage response and the outlet pressure excitation at different oxygen stoichiometries. The fuel cell was operated at 0.2 A cm^{-2} with humidified air at the cathode of φ_C = 20%. The figure is extracted from Shirsath et al. [16].

Figure 38 shows simulated EPIS spectra, for the same variation of oxygen stoichiometry. The simulations are extended to a maximum frequency of 100 Hz, compared to the maximum frequency of 1 Hz in the experiments.

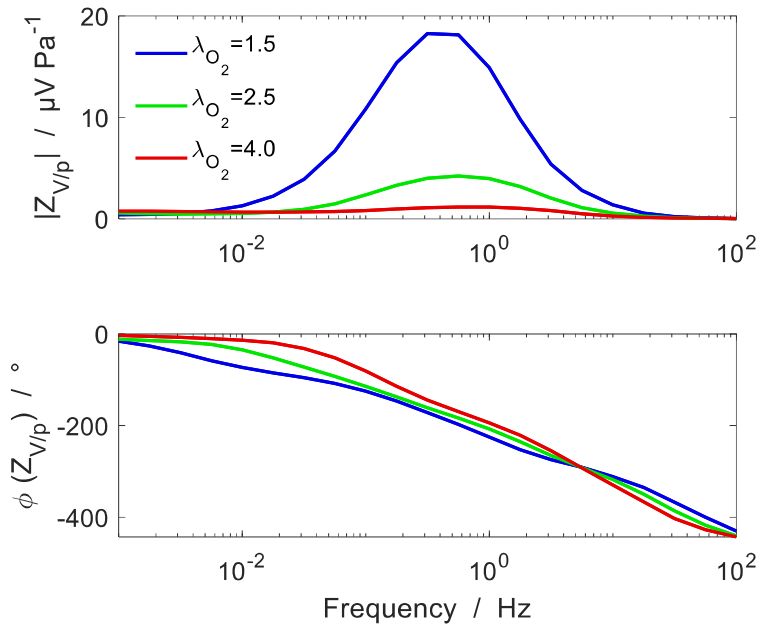

Figure 38: Bode plot of simulated spectra of the transfer function $Z_{V/p}$ between the cell voltage response and the outlet pressure excitation at different oxygen stoichiometries (default value: λ_{O_2} = 2.5). The fuel cell was operated at 0.2 A cm^{-2} with humidified air at the cathode of φ_C = 20%. The spectra of the default value were published in [28].

The magnitude of $Z_{V/p}$ shows a strong increase of the maximum magnitude from 4 µV Pa^{-1} to 18 µV Pa^{-1} for a decrease in stoichiometry from 2.5 to 1.5. For an increase in

stoichiometry up to 4, the maximum nearly vanishes with a remaining maximum of 1 µV Pa^{-1}.

The change in maximum magnitude with stoichiometry of the simulations matches quite well with the trend of the experiments (cf. Figure 37), although the magnitude of the simulations is slightly below the experiments for all analyzed stoichiometries.

Taking a look at the phase shift reveals a stronger decrease in phase shift for a decrease in stoichiometry, especially in the frequency range below 0.1 Hz. Comparing this trend again with the experimental results shows the similar dependence of the phase shift on the oxygen stoichiometry.

As the cell voltage response was previously observed to be closely related to the oxygen pressure oscillation, the corresponding results of the transfer function $Z_{p(\mathrm{O_2,avg})/p}$ are shown in Figure 39. The magnitude shows a qualitative similar progression to the magnitude of transfer function $Z_{V/p}$ (cf. Figure 38) and therefore, an alike dependence on the oxygen stoichiometry. The same holds for the phase shift which is quantitatively similar for both transfer functions.

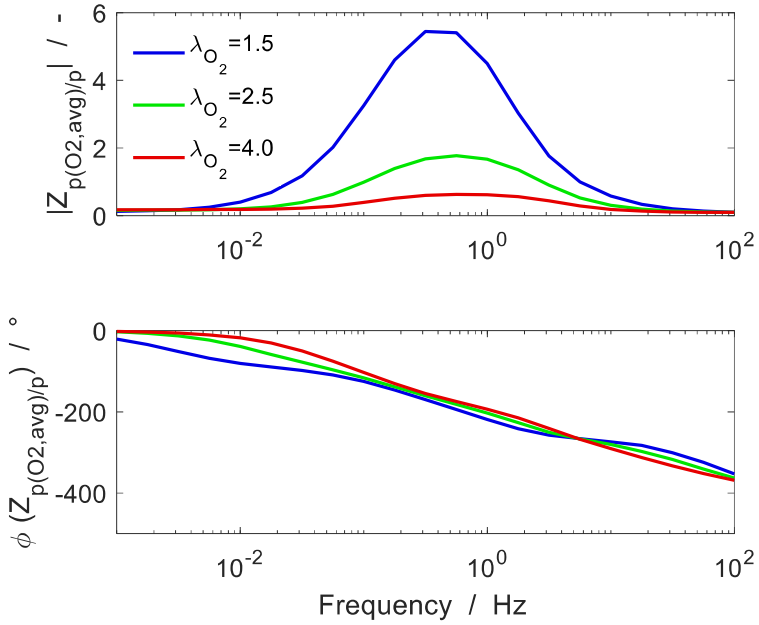

Figure 39: Bode plot of simulated spectra of the transfer function $Z_{p(\mathrm{O_2,avg})/p}$ between the average oxygen pressure oscillation along the CCL and the outlet pressure excitation at different oxygen stoichiometries (default value: $\lambda_{\mathrm{O_2}}$ = 2.5). The fuel cell was operated at 0.2 A cm^{-2} with humidified air at the cathode of φ_{C} = 20%. The spectra of the default value were published in [28].

It was previously deduced that the oxygen pressure oscillation becomes increasingly dominated by the oscillating inlet flow rate with increasing frequency through the linkage of the molar fraction (see Chapter 5.1). To see how the stoichiometry affects this dependence, Eq. 106 should be recalled, which describes a simplified relationship between the

oxygen molar fraction and the oscillating inlet flow rate. The oscillating term in the enumerator is relatively independent of the oxygen stoichiometry, whereas the gas feed in the denominator is proportional to the stoichiometry (cf. Eq. 32). A decrease in stoichiometry thus leads to an increase in oxygen molar fraction oscillation, and hence, increase in cell voltage oscillation.

The trend of the phase shift of $Z_{p(\mathrm{O_2,avg})/p}$ for a variation in stoichiometry can be explained by looking again at the contribution of the total pressure oscillation and the molar fraction oscillation to the partial pressure oscillation in Figure 31. As described above, a decrease of stoichiometry leads to an increase of the molar fraction oscillation of oxygen. In this case, the phase shift of $Z_{p(\mathrm{O_2,avg})/p}$ (blue line) more closely approaches the phase shift of the molar fraction oscillation (red line). Reversely, for an increase of the oxygen stoichiometry, the oxygen molar fraction oscillation decreases and hence the phase shift of $Z_{p(\mathrm{O_2,avg})/p}$ is shifted more towards the phase shift of the total pressure oscillation (green line).

To conclude, the experimentally observed trend for a variation of the oxygen stoichiometry can be explained with the changing influence of the inlet flow rate oscillation, without referring to the phenomenon of diffusion.

6.1.3 Gas composition

In this section, the influence of the composition of the cathode gas feed on the EPIS results is studied. Figure 40 shows experimental EPIS results of Shirsath et al. [17] for a variation of the gas feed composition at a cell current density of 0.2 A cm^{-2}. The molar fraction of the gas feed was increased stepwise from the oxygen molar fraction of air of 0.21 up to pure oxygen. The flow rate of the gas feed was kept constant so that the stoichiometry changed accordingly. The spectra are only presented in the frequency range between 0.01–1 Hz.

At the lowest presented frequency of 10 mHz, the constant quasi-static magnitude seems not to be reached, and hence cannot be examined. The magnitude reveals the following trend for an increase of the oxygen molar fraction. The characteristic increase of magnitude with frequency for the operation with air as the gas feed is less pronounced for an increase of the molar fraction of oxygen to 0.5. For a further increase of molar fraction, the characteristic increase vanishes and turns into a decrease of magnitude with frequency.

The phase shift reveals the following trend for an increase of the oxygen molar fraction. For an increase of oxygen molar fraction to 0.5, the phase shift still resembles the phase shift for the operation with air, which is a constant decrease with frequency to ca. –200° at 1 Hz. For a further increase of oxygen fraction to 0.8 the decrease of phase shift is no more constant. Below 0.1 Hz the phase shift is small, but drops rapidly above 0.1 Hz

leading to a phase shift of nearly –300° at 1 Hz. For pure oxygen, the phase shift is comparatively small in absolute terms over the whole frequency range with a minimum of ca. –20° around 0.2 Hz.
Again, the authors relate the observations to the phenomenon of diffusion, especially the dependence of the phase shift on the oxygen molar fraction.

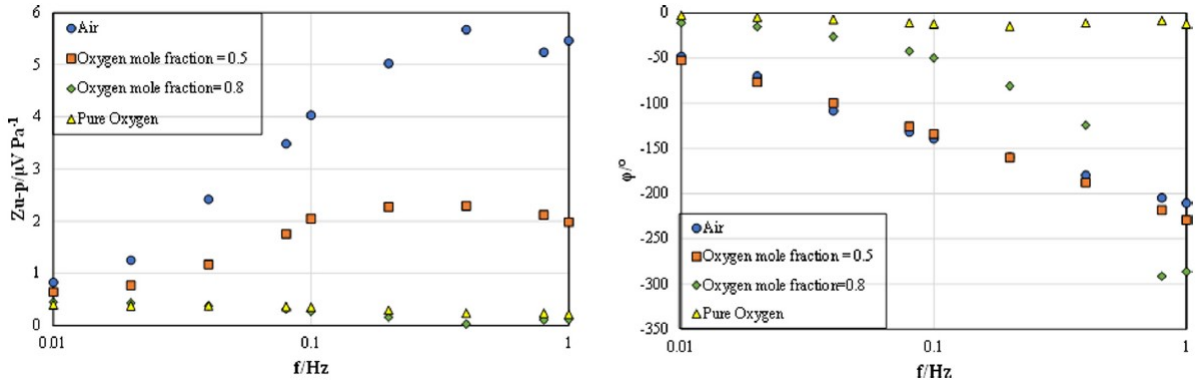

Figure 40: Bode plot of experimental spectra of the transfer function $Z_{V/p}$ between the cell voltage oscillation and the outlet pressure excitation at different gas compositions of the cathode gas feed. The flow rate of the cathode gas feed is constant and humidified with a relative humidity of φ_C = 20%. The fuel cell was operated at 0.2 A cm^{-2}. The figure is extracted from Shirsath et al. [17].

To find another possible explanation for the observed trends, it is revealing to look at the spectra of the average partial pressure oscillation of oxygen in Figure 31. As has been demonstrated in Chapter 5 for the operation with air, the cell voltage response towards higher frequencies is closely connected to the response of the oxygen pressure. The increase of oxygen pressure oscillation with frequency has been related to the increase of molar fraction oscillation, which is caused by the increase of the inlet flow rate oscillation. In case of pure oxygen, the spectra are not showing the increase of magnitude and continuous decrease of phase shift. Moreover, they seem to resemble the spectra of the oxygen pressure oscillation due to the total pressure oscillation, with the decrease in magnitude and a similar minimum of phase shift (see Figure 31, green line). Based on this similarity, it seems that for pure oxygen, the inlet flow rate oscillation does not cause the strong oscillation of the molar fraction of oxygen along the channel. The observed phase shift for an oxygen molar fraction of 0.8 in the figure above, can be interpreted as a transition between the spectrum of air and pure oxygen. Below 0.1 Hz, the oxygen pressure oscillation may be dominated by the total pressure oscillation, whereas above 0.1 Hz, the oscillation of molar fraction is dominating the oxygen pressure oscillation.
The corresponding simulations of EPIS for the different gas compositions are shown in Figure 41. For an increase of the molar fraction of oxygen, the characteristic increase of the magnitude with frequency observed for air gets less pronounced. The maximum magnitude for a molar fraction of 0.5 is already clearly reduced down to 1 µV Pa^{-1} compared

to 4 µV Pa^{-1} for air. A further increase of the oxygen molar fraction leads to a further decrease of the still visible maximum magnitude.

Although the general trend is similar to the experiments, the extent is different. In the experiments the magnitude qualitatively changes for a molar fraction of 0.8 and 1.0 to a monotonous decrease of magnitude with frequency, which cannot be seen in the simulations.

The phase shift of the simulated spectra shows the trend of less decrease for an increase in oxygen molar fraction in the frequency range below 0.1 Hz. Compared to the experiments, this trend is different, especially for the oxygen molar fraction of 0.8 and 1.0, for which the experiment shows a qualitative change, which cannot be reproduced by the simulation. The reason for this difference is not understood.

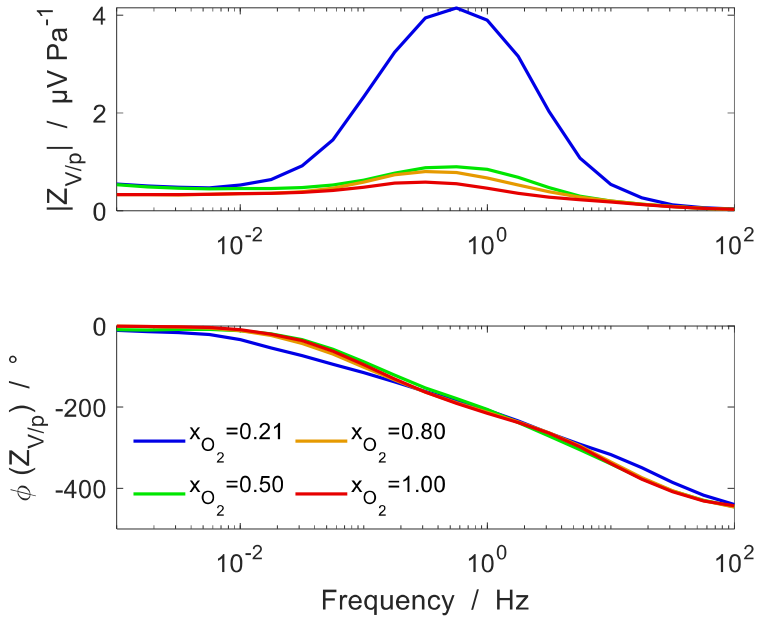

Figure 41: Bode plot of simulated spectra of the transfer function $Z_{V/p}$ between the cell voltage response and the outlet pressure excitation at different gas compositions of the cathode gas feed. The flow rate of the cathode gas feed is constant and humidified with a relative humidity of φ_C = 20%. The fuel cell was operated at 0.2 A cm^{-2}. The spectra of the default value were published in [28].

As the oxygen pressure oscillation has been used for the interpretation of the trend of the experimental spectra, the corresponding transfer function $Z_{p(O_2,avg)/p}$ of the simulation is analyzed subsequently. The spectra of $Z_{p(O_2,avg)/p}$ for the variation of the gas composition are shown in Figure 42.

The quasi-static magnitude shows an increase with oxygen molar fraction and approaches nearly one for pure oxygen. The reason is that the partial pressure oscillation is proportional to its molar fraction at this frequency (see Figure 31).

With increasing frequency, the magnitude for all gas compositions increases, and in case of an oxygen molar fraction of 0.8 and 1.0 even to a comparable maximum as for air. At first, this is surprising, as the magnitude of $Z_{V/p}$ (see Figure 41) shows a distinctively smaller maximum for the oxygen contents of 0.8 and 1.0. A hypothesis explaining this observation is that the ratio between the change of the cell voltage and the change of the average oxygen pressure is changing for the different gas compositions. In fact, the approximation in Eq. 108 and Eq. 109 shows that the ratio is determined by the reciprocal of the oxygen pressure. With increasing the oxygen content of the gas feed, the average oxygen pressure increases and the aforesaid relationship changes accordingly.

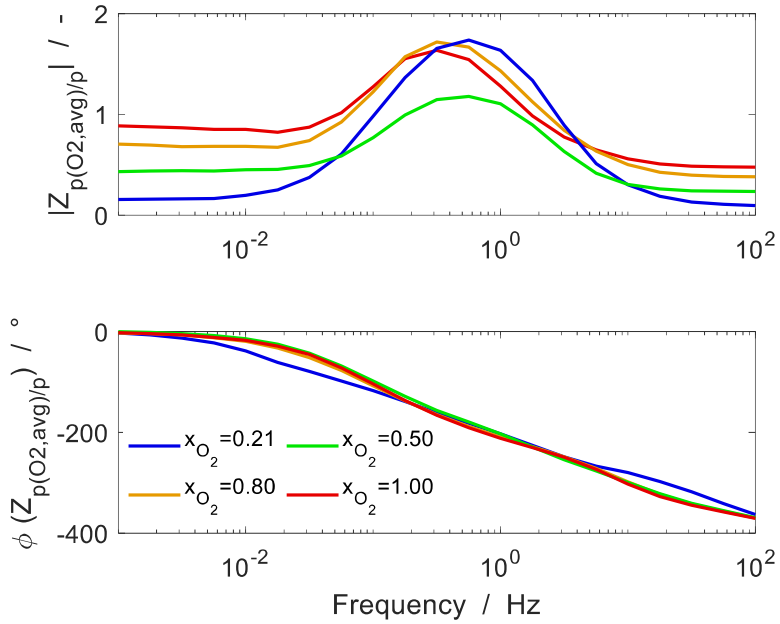

Figure 42: Bode plot of simulated spectra of the transfer function $Z_{p(\mathrm{O_2,avg})/p}$ between the average oxygen pressure oscillation along the CCL and the outlet pressure excitation at different gas compositions of the cathode gas feed. The flow rate of the cathode gas feed is constant and humidified with a relative humidity of φ_C = 20%. The fuel cell was operated at 0.2 A cm^{-2}. The spectra of the default value were published in [28].

Looking at the phase shift shows the strong similarity to the phase shift of the transfer function $Z_{V/p}$ and hence, revealing again that the cell voltage response is following the response of the average oxygen pressure.

Furthermore, the strong decrease in phase shift shows that the partial pressure is dominated by the oscillation of the molar fraction (cf. Figure 31) at all gas compositions. This seems to be different to what was observed in the experiments at an oxygen molar fraction of 0.8 and 1.0. The reason for this difference is not understood.

At the end of this section, some remarks are made on the insightful observation of the change of the relationship between the oxygen pressure oscillation and the cell voltage oscillation based on the change of oxygen concentration in the CL. This correlation is

insightful as it may allow the indirect measurement of the oxygen concentration in the CL and could be used for the detection of reactant starvation due to limited diffusion.
A suitable point of comparison would be the frequency at which the maximum amplitude occurs, for two reasons. First, at this frequency, the influence of the water uptake by the PEM is expected to be negligible and therefore not interfering. Second, towards the quasi-static frequency, the derivative of the equilibrium potential and the overpotential at the cathode with respect to the excitation pressure become independent of the oxygen pressure, and rather dependent on the total pressure (cf. Eq. 89 – 92).
In this context, it is worth mentioning the experiment of Shirsath et al. [16] in which they measured a doubling of the maximum amplitude of the cell voltage oscillation for changing the GDL from a product with MPL to one without (cf. Figure 5). They supposed that the increase of the amplitude is caused by the poor water management of the GDL without MPL, which cannot be reproduced with the present model due to the model limitations. Nevertheless, a hypothesis is that this strong increase of the maximum amplitude is caused by a reduced oxygen concentration in the CL due to the hindrance of accumulated liquid water.
Furthermore, providing the relationship between the maximum oxygen pressure amplitude and the maximum cell voltage amplitude changes with oxygen concentration in the CL (cf. Eq. 109), this has to also influence the results in the previous chapter. An interesting further analysis could be hence the comparison of this relationship for the different stoichiometries. In the context of the current density study, the deviation between the experiments and the simulations towards higher current densities could be argued with the mentioned relationship, to be caused by an inadequate concentration gradient of oxygen through the GDL. Hence, the analysis of the simulated concentration gradient could also be a next step.

6.2 Structural parameters

The changed structural parameters comprise the channel length and the gas humidifier volume.

6.2.1 Gas channel length

In this section, the influence of the gas channel length on the EPIS results is analyzed. In this study, the simulated results are compared to the experimental results of Zhang et al. [18], who measured EPIS for two different fuel cells with different gas channel lengths. As the PEMFC model is not parametrized to their experimental setup, the simulation can only be used for a qualitative comparison with the experiments.
Zhang et al. analyzed two different fuel cells with the same structure of the MEA. One cell had an active area of 50 cm^2 with a serpentine flow field and the other an active area of

12 cm² with a parallel flow field. For the operation with air and a cell load of 1.0 A cm⁻², they obtained the characteristic increase of the magnitude with frequency for both cells. The maximum magnitude of the smaller cell was measured with 40 µV Pa⁻¹ for an oxygen stoichiometry of 3 and the magnitude for the bigger cell with 2 µV Pa⁻¹ for an oxygen stoichiometry of 2. Therefore, it can be stated that the fuel cell area and thus the channel length has a strong influence on the EPIS results. Furthermore, the maximum is shifted towards higher frequencies in case of the smaller cell. The difference of the phase shift between the two cells is less distinct, but shows the trend of a stronger phase shift in the frequency range below 10 mHz for the smaller cell.

After the description of the experimentally observed trend of EPIS for a variation in the channel length, the simulative analysis is discussed subsequently. The simulated variation of channel length comprises three different lengths. Next to the default channel length of 0.304 m twice and half the length are simulated. The cell current density was fixed at 0.2 A cm⁻² with an oxygen stoichiometry of 2.5 and a relative humidity at the cathode inlet of 55%. The results are shown in Figure 43.

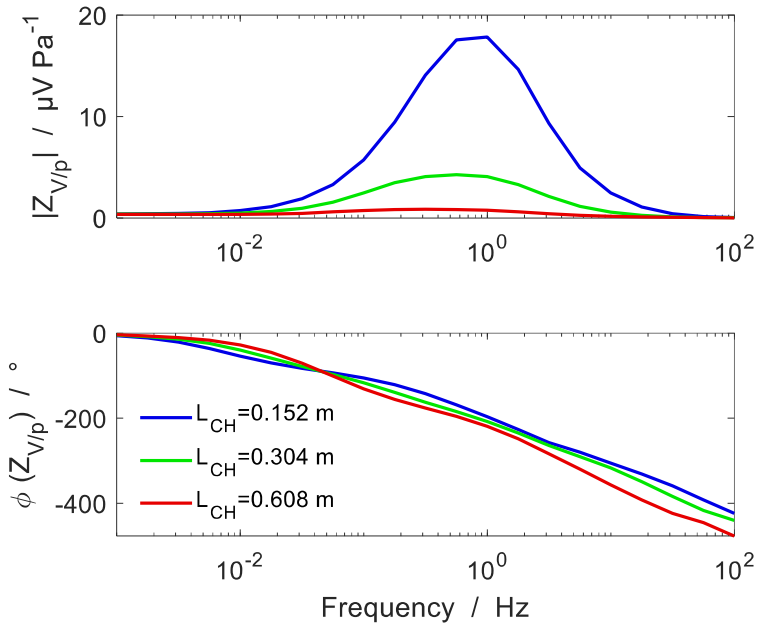

Figure 43: Bode plot of simulated spectra of the transfer function $Z_{V/p}$ between the cell voltage response and the outlet pressure excitation for different channel lengths. The fuel cell was operated at 0.2 A cm⁻² with humidified air at the cathode of φ_C = 55%. The spectra of the default value were published in [28].

The maximum magnitude shows a strong increase from 4 µV Pa⁻¹ to 18 µV Pa⁻¹ for a reduction of the channel length from 0.304 m to half its length of 0.152 m. On the other hand, doubling the channel length leads to a decrease of the maximum magnitude down to 1 µV Pa⁻¹. This trend agrees with the observation of Zhang et al. who measured a higher maximum for the smaller cell with the shorter channel length. Similar to the experiments,

the maximum magnitude is shifted towards higher frequencies for a decrease in channel length.

The phase shift of $Z_{V/p}$ below 50 mHz is stronger for the fuel cell with the shorter channel. Above 50 mHz the trend gets reversed. The trend of a stronger phase shift for the shorter channel configuration in the lower frequency region is also indicated in the experiments.

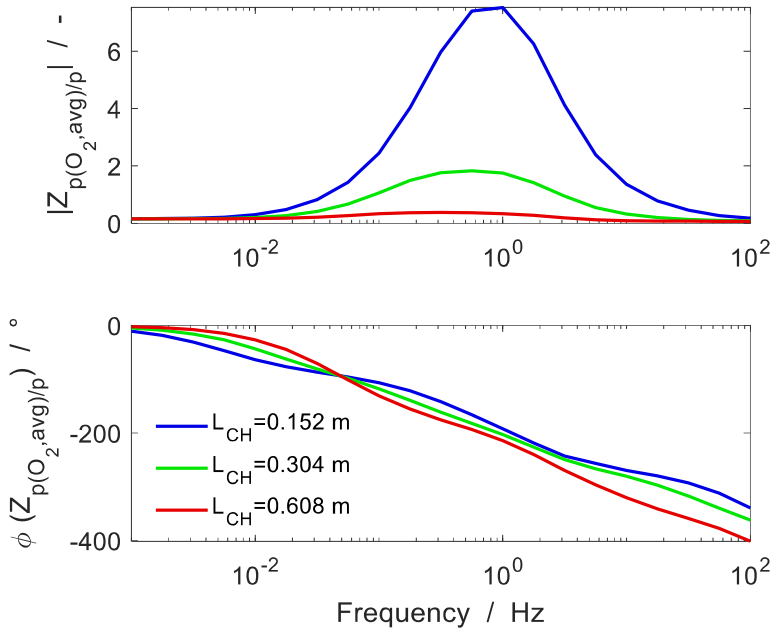

Figure 44: Bode plot of simulated spectra of the transfer function $Z_{p(\mathrm{O_2,avg})/p}$ between the average oxygen pressure oscillation along the CCL and the outlet pressure excitation for different channel lengths. The fuel cell was operated at 0.2 A cm^{-2} with humidified air at the cathode of φ_C = 55%. The spectra of the default value were published in [28].

Taking a look at the simulated spectra of the transfer function $Z_{p(\mathrm{O_2,avg})/p}$ in Figure 44 and comparing them with the spectra of $Z_{V/p}$ reveals a strong similarity. In case of the magnitude, the spectra show a qualitative similar progression, indicating that the cell voltage response is dominated by the oxygen pressure response. The relationship between the change of the cell voltage and the change of oxygen pressure can be approximated at the channel center through Eq. 109. To work out a reason for the stronger increase of the partial pressure oscillation for a reduction of the channel length, the simplified expression of the molar fraction of oxygen in Eq. 106 is considered again. A decrease in the channel length, and thus fuel cell area, leads to a decrease of the inlet flow rate, for a constant stoichiometry. As a consequence, the denominator decreases and thus the oscillation of the oxygen molar fraction increase. This again leads to a stronger increase of the oxygen pressure oscillation and hence cell voltage oscillation.

In case of the phase shift, below 1 Hz, the spectra of the transfer function $Z_{p(\mathrm{O_2,avg})/p}$ and $Z_{V/p}$ are quantitatively similar. The stronger phase shift below 50 mHz for a reduction in channel length can again be explained by the fact that the partial pressure oscillation of

oxygen is more dominated by the oscillation of the molar fraction and hence is closer to its phase shift (cf. red line, Figure 31). Above 50 mHz the trend may change for the following reason. The phase shift of the oscillation of the molar fraction, which dominates the partial pressure oscillation above 50 mHz, has been stated to follow the phase shift $Z_{p/p}$ of the inlet pressure oscillation with an offset of −90° (see Chapter 5.1.2.3). From Figure 25 it can be seen that the decrease of phase shift of $Z_{p/p}$ is shifted towards higher frequencies in case of a reduced channel length.

6.2.2 Gas humidifier volume

In the following section, the influence of the gas volume of the cathode humidifier on the EPIS results is analyzed. Although Shirsath et al. made studies about the influence of the humidifier on the total pressure response of the fuel cell, there exist no results of the corresponding cell voltage response. Therefore, the analysis in this section remains purely simulative; note that the experimentally-observed total pressure response has been reproduced successfully by the simulations (see Figure 23).

The total pressure response of the fuel cell to the outlet pressure excitation is substantially influenced by the gas volume of the humidifier (see Figure 24). The pressure excitation gets damped and delayed towards the channel inlet by the capacitive effect of the gas volume. With increasing the volume, this effect gets shifted towards lower frequencies.

As previously explained, the total pressure oscillation in the gas humidifier causes an oscillation of the inlet flow rate. This has a strong influence on the partial pressure oscillation and hence the cell voltage. The dependence of the two quantities on the gas volume of the humidifier is shown subsequently.

In Figure 45 the simulated cell voltage response, described by the spectra of the transfer function $Z_{V/p}$, is shown for a variation of the gas volume of the humidifier between 0–1000 ml. The default value of the gas volume was 850 ml. The characteristic maximum magnitude of $Z_{V/p}$ is decreasing with decreasing the gas volume inside the humidifier. Furthermore, the decrease leads to a shift of the maximum towards higher frequencies. For small volumes of 10 ml and less, the characteristic maximum disappears and the spectra change qualitatively.

The frequency of the magnitude increase is dependent on the gas humidifier volume while the decrease is not. This information can be helpful by finding the unknown cause for the decrease in magnitude with frequency after reaching its maximum.

The phase shift of $Z_{V/p}$ shows the trend of a delay of the characteristic decrease towards higher frequencies for decreasing the gas humidifier volume. Above 10 Hz the phase shift for the different volumes merge, except for small volumes of 10 ml and less. For those volumes the phase shift seems to qualitatively change and remains on a smaller level.

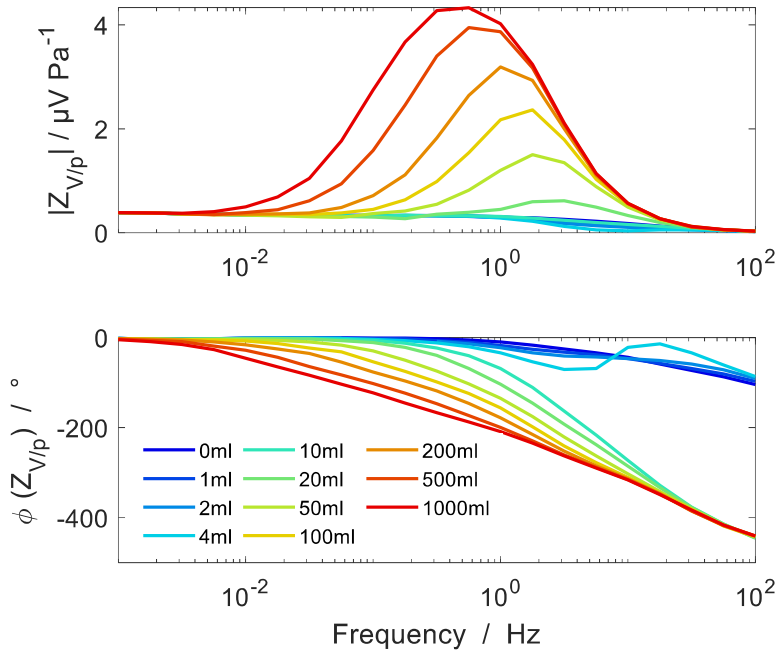

Figure 45: Bode plot of simulated spectra of the transfer function $Z_{V/p}$ between the cell voltage response and the outlet pressure excitation for different gas volumes of the cathode humidifier. The fuel cell was operated at 0.2 A cm^{-2} with humidified air at the cathode of φ_C = 55%. The figure is extracted from Schiffer et al. [28].

Looking at the magnitude of the transfer function $Z_{p(O_2,avg)/p}$ in Figure 46 reveals a qualitatively similar dependence on the gas volume of the humidifier as the magnitude of $Z_{V/p}$. The decrease of the maximum magnitude for decreasing volumes can be explained as follows. The increase of the oxygen pressure oscillation is caused by the increase of the inlet flow rate oscillations. From Eq. 54 it can be seen that the oscillating inlet flow rate is directly proportional to the gas volume inside the humidifier. Hence a decrease leads to a decrease of the maximum oxygen pressure oscillation.

The phase shift of $Z_{p(O_2,avg)/p}$ below 1 Hz is similar to the phase shift of $Z_{V/p}$. The trend that the decrease of phase shift is shifted towards higher frequencies for low volumes can be explained as follows. For lower volumes, the molar fraction oscillation is less due to a decrease of the inlet flow rate oscillation. Hence, the partial pressure oscillation of oxygen is dominated by the total pressure oscillation until higher frequencies (cf. Figure 31). Furthermore, the phase of the inlet flow rate oscillation corresponds to the phase of the inlet pressure oscillation shifted by –90°. The phase shift of the inlet pressure is also shifted towards higher frequencies for lower gas volumes of the humidifier (cf. Figure 24).

For volumes below 4 ml the phase shift shows a qualitatively different progression compared to the phase shift of the bigger volumes. This is probably due to the fact that for these small volumes, the partial pressure oscillation is dominated by the total pressure oscillation throughout the whole frequency range. This transition resembles, although in

another frequency range due to the different gas volume, the transition which was observed in the EPIS experiments for varying gas compositions (cf. Figure 40).

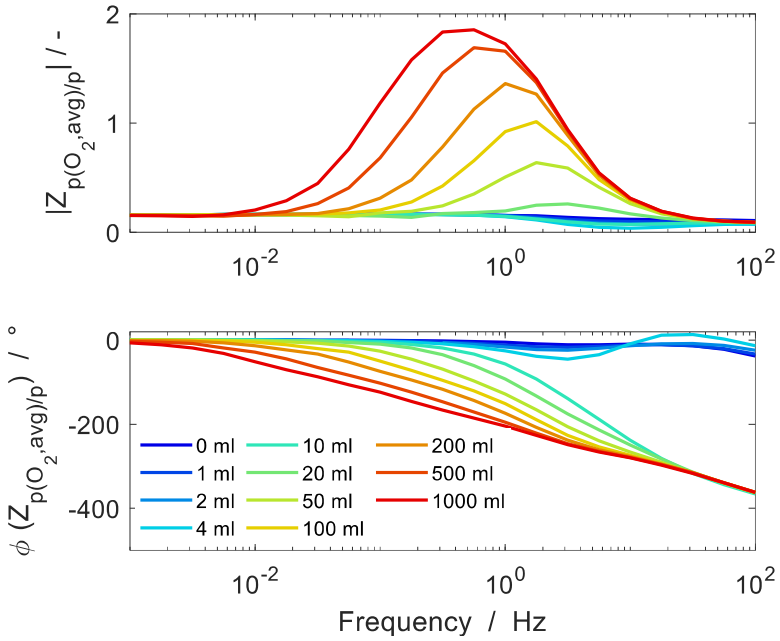

Figure 46: Bode plot of simulated spectra of the transfer function $Z_{p(O_2,avg)/p}$ between the average oxygen pressure oscillation along the CCL and the outlet pressure excitation for different gas volumes of the cathode humidifier. The fuel cell was operated at 0.2 A cm^{-2} with humidified air at the cathode of φ_C = 55%.

Above 1 Hz the phase shift of $Z_{V/p}$ shows a stronger decrease than $Z_{p(O_2,avg)/p}$, which is also the case in the previous chapters but especially visible in the figure below at volumes below 4 ml. It is hypothesized that this is due to the influence of the DL, which causes a delay of the cell voltage oscillation compared to the partial pressure oscillation in this frequency range (see Chapter 7.1).

6.3 Conclusion

The simulation of the influence of operational and structural parameters on EPIS has shown that most experimental trends could be captured by the simulation. With the help of the finding in the previous chapter, which is the strong correlation between the oxygen pressure oscillation and the cell voltage oscillation, it has been possible to interpret the influence of the parameters on EPIS.

For increasing current densities, the characteristic increase of magnitude with frequency is less pronounced. The reason for this trend may be the reduced influence of the inlet flow rate oscillation on the oxygen pressure oscillation towards high current densities. The trend is much more distinct in the simulations than in the experiments, which leads to a deviation of the EPIS results towards high current densities.

The experimentally observed trend for a variation of oxygen stoichiometry can be well captured by the simulation. The amplified increase of magnitude with frequency for a decrease of the oxygen stoichiometry was related to the oscillating inlet flow rate, which causes a stronger oscillation of the molar fraction of oxygen for a decrease of the oxygen stoichiometry. The same effect leads to the observed trend of phase shift. This shows that the experimentally observed trend can be explained without referring to the phenomenon of diffusion.

With changing the gas composition of the cathode gas feed from air towards pure oxygen, the experimental EPIS results reveal a qualitative change. For pure oxygen the spectra do not show the increase of magnitude and continuous decrease of phase shift with frequency observed for air. It is hypothesized that this qualitative change is due the diminishing influence of the inlet flow rate oscillation. The hypothesis is supported by the fact that the cell voltage response seems to be dominated by the average total pressure response along the gas channel. Although the simulations show a decrease in magnitude and a less strong phase shift towards pure oxygen, the qualitative change of the experiments cannot be reproduced by the simulations.

The experimentally-observed trend for a variation of the gas channel length can be reproduced with the simulations. The stronger increase of the magnitude with frequency for a shorter gas channel is related to the stronger influence of the inlet flow rate oscillation. The trend of the phase shift is also related to the same phenomenon.

The variation of the gas volume of the humidifier shows the dominant influence of this parameter on EPIS. Without considering the humidifier, the signal changes drastically and reveals qualitatively different spectra.

An interesting finding was made in the context of the study of the different gas compositions. The relationship between the cell voltage oscillation and the oxygen pressure oscillation was observed to change with the oxygen concentration in the CL. Based on this relationship, the maximum magnitude of $Z_{V/p}$ could be used to indirectly measure the oxygen concentration and thus detect reactant starvation due to limited diffusion.

7 EPIS (3): Influence of time-dependent processes

In the following chapter, the third and last part of the EPIS study is presented. It contains a pure simulative study about the influence of the time-dependent processes of the PEMFC model on EPIS. The chapter comprises one subchapter for each time-dependent process, in which the individual influence on the EPIS result is analyzed separately. The results shown in this chapter were partially submitted to the Journal of the Electrochemical Society [109].

The time-dependent processes of the PEMFC model are the charge and discharge of the electric DL, the water uptake by the PEM, the gas transport through the GDL and the gas transport through the gas channel with and without consideration of the humidifier. The separation of the individual processes was realized by simulating different model configurations, in which the time-dependent process of interest was switched on, while the other processes were switched off. The respective parameter variation for each process is shown in Table 5. The CL was not resolved in this study.

Table 5: Parameter variation to switch individual time-dependent processes on and off

Time-dependent process	Parameter	on	off
DL charge/ discharge	$C_{\mathrm{DL}}^{\mathrm{A}}$	410 F m^{-2}	0 F m^{-2}
Water uptake PEM	σ_{elyt}	$f(\lambda)$	3.4 S m^{-1}
Gas transport GDL	L_{GDL}	212.5 µm	0 µm
Gas transport gas channel	L_{CH}	0.304 m	0 m
Humidifier	V_{hum}	850 ml	0 ml

The EPIS simulation of the respective model configuration is compared to a reference model configuration, in which all time-dependent processes are switched off. Hereinafter, this configuration is called the time-independent model. Additionally, the spectra are interpreted by the use of the cell voltage derivative with respect to the excitation pressure of Chapter 3.3, simplified for the respective model configuration.

The simulations were conducted for a cell current density of 0.2 A cm^{-2}, at which the best agreement between the simulations and the experiments was observed.

The simulated transfer function $Z_{V/p}$ of the time-independent model is a scalar with the value of 0.32 µV Pa^{-1}. This value can also be derived analytically by inserting Eq. 77, 81, 83 in Eq. 76 with the following simplifications being valid for the time-independent model:

- $f \neq f(x, y)$
- $C_{\mathrm{DL}}^{\mathrm{A}} = 0$

- $\partial i_{\mathrm{elyt}}^{\mathrm{CL|PEM}}/\partial p = 0$
- $\partial \sigma_{\mathrm{elyt}}/\partial p = 0$

With all processes switched off, the PEMFC model becomes a 0D model. Additionally, the ionic current through the PEM is constant for a 0D model under galvanostatic operation. With the simplifications above, the derivative of the cell voltage with respect to the excitation pressure is

$$\frac{\partial V_{\mathrm{cell}}}{\partial p} = \frac{RT}{F}\left(\frac{1}{4}+\frac{0.54}{\alpha_{\mathrm{C}}}\right)\frac{1}{p_{\mathrm{O_2}}}\frac{\partial p_{\mathrm{O_2}}}{\partial p} = \frac{RT}{F}\left(\frac{1}{4}+\frac{0.54}{\alpha_{\mathrm{C}}}\right)\frac{1}{p-p_{\mathrm{H_2O}}} = 0.32\ \mu\mathrm{V\ Pa^{-1}}\ , \qquad (111)$$

with $p_{\mathrm{O_2}} = x_{\mathrm{O_2}}(p-p_{\mathrm{H_2O}})$, $x_{\mathrm{O_2}} = 0.21$, $p = 116\,325$ Pa and $p_{\mathrm{H_2O}} = \varphi_{\mathrm{C}} p_{\mathrm{sat}}(T)$ $= 0.55 \cdot 15\,760$ Pa $= 8668$ Pa.

7.1 DL charge and discharge

In this subchapter the influence of the DL charge and discharge on the transfer function $Z_{V/p}$ is analyzed. By switching on the DL charge and discharge through the parameter of the capacity, the model is still nondimensional. But next to the faradaic current, now the DL current is flowing proportional to the change of the cathode Galvani potential per time (see Eq. 13).

Figure 47 shows the comparison of the simulated EPIS results between the time-independent model and the model considering the charge and discharge of the DL. The frequency range was extended up to a maximum frequency of 10 kHz.

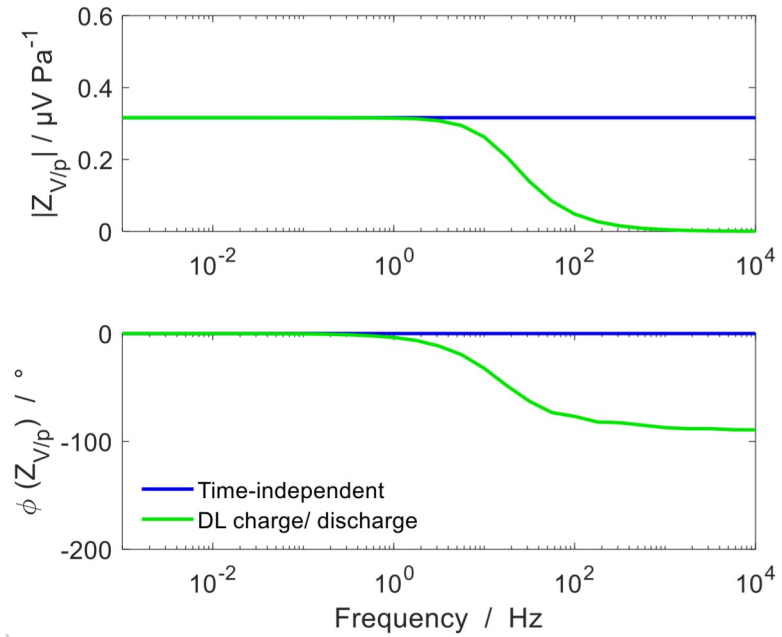

Figure 47: Bode plot of the simulated spectra of the transfer function $Z_{V/p}$ between the cell voltage oscillation and the outlet pressure excitation for a comparison of the model configuration considering the DL charge and discharge and the time-independent model at 0.2 A cm^{-2}.

In the frequency region below 1 Hz, the magnitude of both model configurations is nearly identical with a constant value of 0.32 µV Pa^{-1}. The influence of the DL charge and discharge becomes visible above 1 Hz. Here, the magnitude drops mainly between 1–100 Hz and approaches zero for frequencies beyond. The DL charge and discharge leads to a decrease of the phase shift also mainly between 1–100 Hz and approaches a value of –90° for frequencies above.

The comparison between the characteristic frequency (minimum of imaginary part) of the transfer function $Z_{V/p}$ (EPIS) and $Z_{V/i}$ (EIS) reveals similar values of 18 Hz and 16 Hz, respectively. Therefore, it can be concluded that the DL charge and discharge causes features for EPIS and EIS at the same frequency.

To interpret the observed features caused by the DL charge and discharge, the derivative of the cell voltage with respect to the pressure excitation (Eq. 77, 81, 83 in Eq. 76) is considered again. For the given model configuration, the following simplifications can be made:

- $f \neq f(x, y)$
- $\partial i_{\mathrm{elyt}}^{\mathrm{CL|PEM}} / \partial p = 0$
- $\partial \sigma_{\mathrm{elyt}} / \partial p = 0$

The derivative of the cell voltage with respect to the pressure excitation is then

$$\frac{\partial V_{\mathrm{cell}}}{\partial p} = \frac{RT}{F}\left(\frac{1}{4} + \frac{0.54}{\alpha_{\mathrm{C}}}\right)\frac{1}{p - p_{\mathrm{H_2O}}} - \frac{RT}{\alpha_{\mathrm{C}} F} C_{\mathrm{DL}}^{\mathrm{A}} \frac{\frac{\partial}{\partial p}\left(\frac{\partial(\Delta\phi_{\mathrm{C}})}{\partial t}\right)}{-i_{\mathrm{elyt}}^{\mathrm{CL|PEM}} + C_{\mathrm{DL}}^{\mathrm{A}} \frac{\partial(\Delta\phi_{\mathrm{C}})}{\partial t}} \,. \tag{112}$$

From this equation, it can be seen that for slow changes of the cathode Galvani potential, the equation is approaching the derivative of the time-independent model (cf. Eq. 111), which is the case in the frequency range below 1 Hz. Here, the change of the cell voltage with pressure is equal to the change of the equilibrium potential and the change of the overpotential at the cathode, due to the change of oxygen pressure (cf. Eq. 77, 81).

With increasing frequency, the change of the Galvani potential per time increases, which leads to an increase of the subtrahend in the equation above. Towards high frequencies the subtrahend approaches the minuend and as a consequence the magnitude of $Z_{V/p}$ approaches zero.

More practically spoken, the increase of the Galvani potential change per time leads to an increase of the DL charge and discharge current. To keep the cell current constant at galvanostatic control, the faradaic current has to change accordingly. This in turn leads to a change of the overpotential and hence cell voltage with an opposite sign compared to the cell voltage change caused by the oxygen pressure change.

7.2 Water uptake of the PEM

In this subchapter, the influence of the PEM on the transfer function $Z_{V/p}$ is analyzed. Therefore, the time-independent model is extended by the discretization of the PEM layer and the water uptake through absorption plus the water transport through the electrolyte via electro-osmotic drag and diffusion is enabled. The conductivity of the PEM is no more constant, but depends on the water content of the electrolyte λ. The water content of the electrolyte in the CL depends on the water pressure of the adjacent gas phase. An increase of the cathode water pressure, for example, leads to an increase of the water content in the electrolyte of the cathode. The increase of the water content gets then distributed through the PEM by the finite transport of water. This again leads to an increase of the electrolyte conductivity and hence a decrease of the potential difference across the electrolyte and thus increase in cell voltage.

In the previous simulations, the water pressure at the cathode inlet has been a boundary condition. This boundary condition stems from the gas humidifier upstream the fuel cell, which ensures that the gas entering the fuel cell contains a certain relative humidity. For the present model configuration, without the gas channel or the GDL, the water pressure is therefore not changing during the pressure excitation. To still work out the influence of water pressure for the present model configuration, the boundary condition is changed from constant water pressure to constant molar fraction of water.

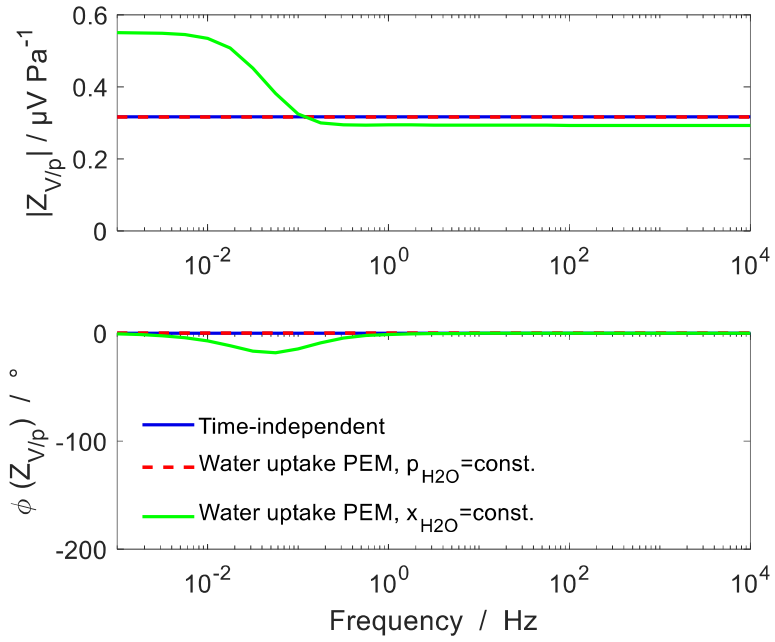

Figure 48: Bode plot of the simulated spectra of the transfer function $Z_{V/p}$ between the cell voltage oscillation and the outlet pressure excitation for a comparison of the model configuration considering the PEM water uptake and the time-independent model at 0.2 A cm^{-2}. The model configuration considering the PEM water uptake is shown for the boundary condition of constant water pressure and constant molar fraction of water.

Figure 48 shows the comparison of the simulated EPIS results between the time-independent model and the model considering the water uptake by the PEM. For the boundary condition of constant water pressure, the transfer function is the same compared to the time-independent model. In case of the boundary condition of constant molar fraction of water, the water pressure is oscillating and the influence of the water uptake of the PEM on the EPIS results becomes visible.

At a frequency of 1 mHz, the magnitude of the transfer function is nearly twice the value of the time-independent model. This means at the quasi-static frequency, the change of the potential difference across the electrolyte, due to the change of water pressure, is about the same as the change of the cathode Galvani potential, due to the change of oxygen pressure.

A comparison of these values with the static pressure-voltage response of the full model setup at 0.2 A cm^{-2} (cf. Figure 20) shows that the change of the potential difference across the electrolyte with pressure for the present model is clearly larger. This observation is supposed to originate from the dryer gas phase for the present model compared to the gas phase of the full fuel cell model, which gets enriched with product water of the ORR throughout the cell. The increase of water pressure may have a stronger influence on the electrolyte conductivity in dryer conditions.

The influence of the time dependence of the water uptake by the PEM becomes mainly visible in the frequency range between 10–100 mHz. In this range, the magnitude decreases and approaches a constant value slightly below the time-independent model. The decrease of magnitude is accompanied by a minimum phase shift of –20° around 50 mHz.

To further interpret the observed feature caused by the water uptake of the PEM, the derivative of the cell voltage with respect to the pressure excitation (Eq. 77, 81, 83 in Eq. 76) is considered again. For the given model configuration, the following simplifications can be made:

- $f \neq f(x)$
- $C_{\mathrm{DL}}^{\mathrm{A}} = 0$
- $\partial i_{\mathrm{elyt}}^{\mathrm{CL|PEM}} / \partial p = 0$

With consideration of the boundary conditions of a constant molar fraction of water the derivative can be simplified to

$$\frac{\partial V_{\mathrm{cell}}}{\partial p} = \frac{RT}{F}\left(\frac{1}{4} + \frac{0.54}{\alpha_{\mathrm{C}}}\right)\frac{1}{p} + \int_{y=\mathrm{CCL}}^{y=\mathrm{ACL}} i_{\mathrm{elyt}}(y)\,\frac{\partial}{\partial p}\left(\frac{1}{\sigma_{\mathrm{elyt}}(y)}\right)\mathrm{d}y \ . \tag{113}$$

From this equation it can be seen that the change of the potential difference across the electrolyte is caused by a change of the electrolyte conductivity. The time dependence of the change of the electrolyte conductivity to change with the cathode gas phase pressure is caused by the finite rate of water diffusion inside the electrolyte.

The constant magnitude in the frequency range above 1 Hz corresponds to the change of Galvani potential caused by the oxygen pressure. The magnitude is slightly below the magnitude of the time-independent model because of the change of the boundary condition. The difference can be seen by comparing Eq. 111 with the first summand of Eq. 113.

7.3 Gas transport in the GDL

In this subchapter the influence of the gas transport through the GDL on the transfer function $Z_{V/p}$ is analyzed. Therefore, the time-independent model is extended by the GDL, which means the gas composition in the CL is no more a boundary condition, but the gas entering the GDL. The gas in the CL is now influenced by the time-dependent process of transport trough the GDL with a finite velocity. The two considered transport mechanisms are diffusion of species due to a concentration gradient, and convection of the gas mixture due to a pressure gradient.

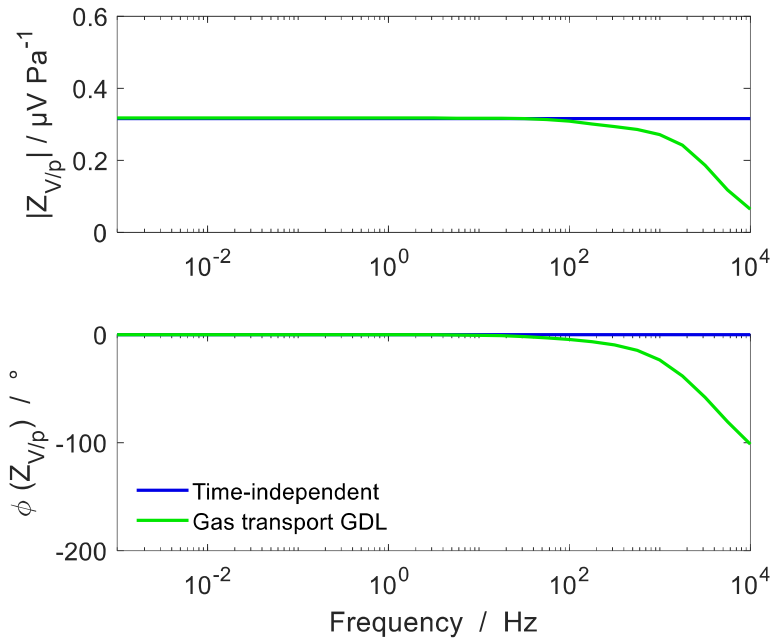

Figure 49: Bode plot of the simulated spectra of the transfer function $Z_{V/p}$ between the cell voltage oscillation and the outlet pressure excitation for a comparison of the model configuration considering the gas transport through the GDL and the time-independent model at 0.2 A cm^{-2}.

Figure 49 shows the comparison of the simulated EPIS results between the time-independent model and the model considering the transport through the GDL. In the frequency range below 100 Hz the cell voltage response is nearly the same for both model configurations, visible as the conformity in magnitude and phase shift.
Only above 100 Hz the influence of the gas transport through the GDL becomes visible, which is due to the short distance in transport direction of 212.5 µm. The magnitude shows a continuous decrease towards zero and has a remaining magnitude of 20 % at

10 kHz. The phase shift shows a qualitatively similar decrease above 100 Hz leading to a phase shift of –100° at 10 kHz. It should be stressed here that these features are above the frequency range of the experimental studies and above the maximum frequency of the simulations in the previous chapters.

The derivative of the cell voltage with respect to the excitation pressure (Eq. 77, 81, 83 in Eq. 76) can be simplified for the given model setup similarly to the time-independent model with consideration of the discretization in y-direction. This results in the following assumptions:

- $f \neq f(x)$
- $C_{\mathrm{DL}}^{\mathrm{A}} = 0$
- $\partial i_{\mathrm{elyt}}^{\mathrm{CL|PEM}} / \partial p = 0$
- $\partial \sigma_{\mathrm{elyt}} / \partial p = 0$

With these simplifications, the pressure derivative of the cell voltage can be written as

$$\frac{\partial V_{\mathrm{cell}}}{\partial p_{\mathrm{GDL}}^{\mathrm{y=0}}} = \frac{RT}{F}\left(\frac{1}{4} + \frac{0.54}{\alpha_{\mathrm{C}}}\right)\frac{1}{p_{\mathrm{O_2,CL}}}\frac{\partial p_{\mathrm{O_2,CL}}}{\partial p_{\mathrm{GDL}}^{\mathrm{y=0}}} \,, \tag{114}$$

where the pressure excitation is at the exterior of the GDL which is indicated by the superscript $y = 0$.

From the equation above it can be seen that the cell voltage oscillation follows the oxygen pressure oscillation. Therefore, the decrease in magnitude and phase shift above 100 Hz has to be caused by a decrease and delay of the average oxygen pressure oscillation in the CL. The reason for the decrease in magnitude and phase shift of the oxygen pressure oscillations is unclear.

The frequency range of the feature indicates that it is not related to the phenomenon of diffusion but rather related to the convective transport. Ziegler et al. [110] report that oxygen gradients through the GDL reach equilibrium within 0.05 s, which corresponds to a characteristic frequency of 20 Hz. Furthermore, the process of diffusion is not expected to be affected by a change of the total pressure, because the concentration gradients do not change. Hence, the process of diffusion cannot be characterized directly with the given approach.

7.4 Gas transport in the gas channel

In this subchapter the influence of the gas transport through the gas channel on the transfer function $Z_{V/p}$ is analyzed. The modeling of the gas channel transport leads to a discretization of the model in x-direction. The gas is transported through the gas channel via convection and diffusion.

As previously observed, the gas humidifier has a strong influence on the pressure response along the channel. To solely study the influence of the gas channel first, the present subchapter is divided into an analysis with and without the humidifier.

To interpret the features caused by the gas transport through the gas channel, the derivative of the cell voltage with respect to the pressure excitation (Eq. 77, 81, 83 in Eq. 76) is again considered. For the given model configuration, the following simplifications can be made:

- $f \neq f(y)$
- $C_{\mathrm{DL}}^{\mathrm{A}} = 0$
- $\partial\sigma_{\mathrm{elyt}}/\partial p = 0$

Previously, without discretization of the model in x-direction, the ionic current trough the electrolyte has been equal to the cell current and hence, constant due to the galvanostatic operation. In case of the present model configuration, locally the ionic current can change during pressure excitation, and rather the sum of all ionic currents along the channel are constant. Therefore, the derivative of the ionic current with respect to the outlet pressure excitation has to be included. With the other simplifications above, the derivative of the cell voltage with respect to the cathode outlet pressure is

$$\frac{\partial V_{\mathrm{cell}}}{\partial p_{\mathrm{CCH}}^{\mathrm{out}}} = \frac{RT}{F}\left(\frac{1}{4} + \frac{0.54}{\alpha_{\mathrm{C}}}\right)\frac{1}{p_{\mathrm{O_2,CL}}(x)}\frac{\partial p_{\mathrm{O_2,CL}}(x)}{\partial p_{\mathrm{CCH}}^{\mathrm{out}}} + \frac{RT}{\alpha_{\mathrm{C}}F}\frac{1}{-i_{\mathrm{elyt}}^{\mathrm{CL|PEM}}(x)}\frac{\partial i_{\mathrm{elyt}}^{\mathrm{CL|PEM}}(x)}{\partial p_{\mathrm{CCH}}^{\mathrm{out}}} + \frac{L_{\mathrm{PEM}}}{\sigma_{\mathrm{elyt}}}\frac{\partial i_{\mathrm{elyt}}^{\mathrm{CL|PEM}}(x)}{\partial p_{\mathrm{CCH}}^{\mathrm{out}}} \quad . \tag{115}$$

7.4.1 Without humidifier

The present section analyses the influence of the gas transport through the gas channel without considering the gas volume in the humidifier. Figure 50 shows the comparison of the simulated EPIS results between the time-independent model and the model considering the gas transport in the gas channels.

In the frequency range below 1 Hz the magnitude and phase shift are quite similar for both models. Based on this similarity the change of the cell voltage with the outlet pressure is expected to correspond to the first summand on the right-hand side of Eq. 115 (cf. Eq. 111). The two remaining summands therefore have to cancel each other out. This hypothesis agrees with the previous observation in Chapter 4.5.

The influence of the gas channel becomes visible in the frequency range above 1 Hz and shows features in two different frequency ranges. In the frequency range between 1–10 Hz the first feature can be observed. The magnitude decreases which is accompanied by a local minimum in the phase shift of –10°. The reason for this feature remains unclear. It should be stated here that the decrease in magnitude is occurring in the same range as the decrease in magnitude observed with consideration of the gas volume in the humidifier, shown in the next section. This indicates that it might be caused by the same phenomenon.

The magnitude of the gas channel model shows a constant value between 10–100 Hz, followed by a second feature in the frequency range above. The magnitude shows a decrease

down to zero with a superimposed oscillation. In the same range, the phase shift shows a decrease down towards –180°, also accompanied by a superimposed oscillation.
The second feature above 100 Hz is explained by the following hypothesis. Above 100 Hz, the total pressure oscillation is supposed to oscillate with a similar amplitude but different phase along the channel due to the finite velocity of pressure propagation. The oscillations along the channel cancel each other out in their effect on the cell voltage. It should be stressed here that this feature is above the frequency range studied experimentally and also above the maximum frequency of the simulations in the previous chapters.

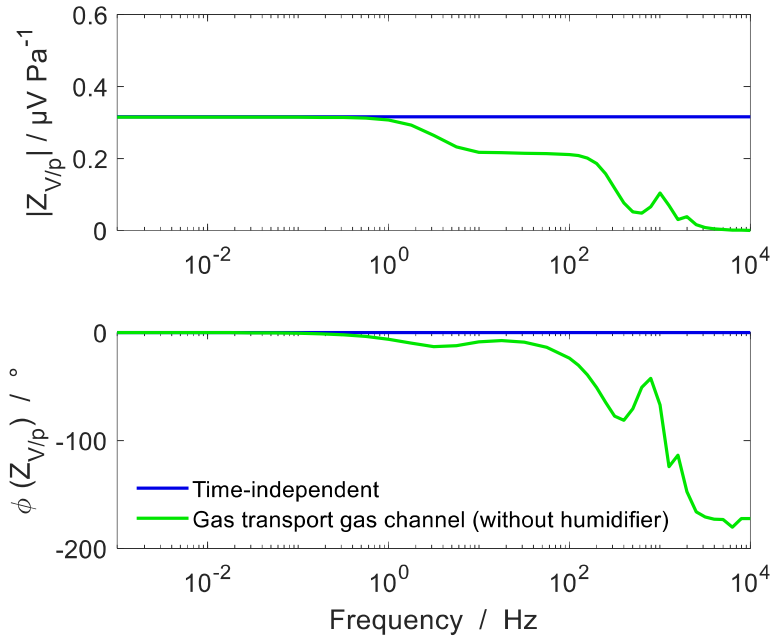

Figure 50: Bode plot of the simulated spectra of the transfer function $Z_{V/p}$ between the cell voltage oscillation and the outlet pressure excitation for a comparison of the model configuration considering the gas transport through the gas channel (without gas volume of the humidifier) and the time-independent model at 0.2 A cm^{-2}.

7.4.2 With humidifier

Figure 51 shows the comparison of the simulated EPIS results between the time-independent model and the model considering the gas transport in the gas channels, now with consideration of the gas volume of the humidifier upstream the cathode gas channel. At the quasi-static frequency of 1 mHz, both model configurations show a similar magnitude and phase shift.
With increasing frequency, the influence of the gas channel transport becomes directly visible by showing an increase of the magnitude up to a maximum close to 1 Hz followed by a decrease between 1–100 Hz. The phase shift shows a constant decrease from 0° at 1 mHz down to nearly –400° at 100 Hz.

Comparing the spectra in the same frequency range with the spectra of the same model without the humidifier (cf. Figure 50) shows again the dominating influence of the humidifier on the EPIS results.
A comparison between the spectra of the reduced model configuration in this section with the spectra of the full model and the experiments (cf. Figure 35) reveals a strong similarity. The most prominent feature of EPIS, the increase of magnitude with frequency, can therefore be reproduced by simply modeling the gas channel in combination with the gas humidifier connected upstream the fuel cell. For the explanation of the observed increase of magnitude with frequency and the corresponding phase shift the reader is referred to Chapter 5.

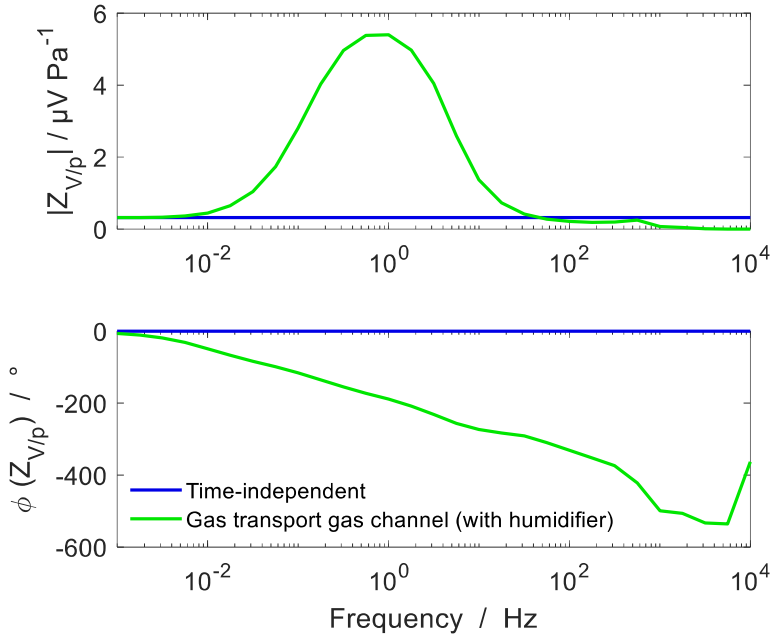

Figure 51: Bode plot of the simulated spectra of the transfer function $Z_{V/p}$ between the cell voltage oscillation and the outlet pressure excitation for a comparison of the model configuration considering the gas transport through the gas channel (with gas volume of the humidifier) and the time-independent model at 0.2 A cm^{-2}.

It should be stressed here that the diffusion of reactants through the GDL to the reactive sites was not included in the simple gas channel model. Therefore, the interpretation of Shirsath et al. (see Chapter 2.2.2), who attributed the strong decrease in phase shift to the phenomenon of diffusion can be at least questioned.
Based on the finding that the EPIS results seem to be mainly dominated by the combined influence of the gas channel and the gas humidifier, the initial hypothesis of EPIS as a useful tool to detect diffusion phenomena is weakened. However, in this context, a promising finding is the relationship between the cell voltage oscillation and the oxygen pressure oscillation, which was observed to be dependent on the oxygen concentration in the CL (see 6.1.3).

7.5 Conclusion

The separate simulation of time-dependent processes has demonstrated their individual influence on EPIS. The simulated influence of the DL appears for frequencies above 1 Hz, which is above the maximum frequency of the EPIS setups using a pressure controller for the pressure excitation. The water uptake of the PEM is visible in the spectra in the frequency range between 10–100 mHz. However, in the experiments this feature is expected to be masked by the influence of the humidifier. The gas transport through the GDL becomes visible at frequencies beyond 100 Hz, which is above the analyzed frequency range of the experiments. The phenomenon of diffusion in the GDL cannot be characterized directly.

The analysis of the gas channel transport with consideration of the humidifier shows that the EPIS signal of the full model setup is dominated by this process, which makes the direct measurement of other processes difficult.

However, in the context of diffusion in the GDL, a promising finding may be the observed relationship between the cell voltage oscillation and the oxygen pressure oscillation, which is dependent on the oxygen concentration in the CL (see Chapter 5.2 and 6.1.3). This may enable measuring the oxygen concentration in the CL and thus, indirectly, the diffusion of oxygen.

8 Summary and outlook

The present dissertation showed the first model-based analysis of the characterization method EPIS applied to a PEMFC. In EPIS, the cell voltage response for a harmonic excitation of the gas phase pressure is analyzed in the frequency domain by means of the transfer function between both quantities. Recently, three different working groups have used EPIS to experimentally investigate mass transport processes in single-cell PEMFCs. The measured spectra in the frequency range between 1 mHz–100 Hz showed different features, depending on the fuel cell structure and the operating conditions. To further benefit from the observed features, it is essential to understand their origin that was heretofore unknown. The main goal of the present study therefore was to increase the understanding of EPIS by finding out causal links between specific processes and the resulting cell voltage response.

To this end, a simulative investigation was conducted by the use of a pseudo-2D model, considering the major transport mechanisms in the gas channel direction and in through-plane direction. Both dimensions are relevant for the reproduction of EPIS. A modeling novelty was the implementation of the gas volume inside the humidifier upstream the cathode gas channel. With this extension of the state-of-the-art PEMFC modeling the EPIS experiments could be reproduced successfully at current densities ≤ 0.4 A cm^{-2}, where the model allows a further simulative analysis of the observed EPIS features. For higher current densities, the model is not able to fully reproduce the experiments, which may be due to the limiting model simplification of not considering the formation and transport of liquid water in the electrodes and in the gas channels.

The PEMFC model was parametrized and validated by reproducing experiments other than EPIS, such as the steady-state and dynamic voltage-current relations and the pressure drop along the gas channel. The simulations showed a good agreement with the experiments at lower current densities, whereas towards higher current densities the experiments and the simulations differed. The comparison of the transferred amount of water through the PEM revealed that the model is not able to reproduce the experimental behavior. However, this was not critical for the reproduction of EPIS.

The simulative investigation of EPIS was subdivided into three parts. The aim of the first part was to determine the origin of typically observed EPIS features, by tracing back the cell voltage response to the partial pressure response of oxygen and water. The cell voltage of the model is influenced by the oxygen pressure through the equilibrium potential and the reaction kinetics at the cathode and influenced by the water pressure through the electrolyte conductivity. The cell voltage oscillation was observed to strongly correlate with the oscillation of the oxygen pressure throughout the whole frequency range, whereas the influence of the water pressure oscillation on the cell voltage was only visible

at low frequencies. The ratio between the cell voltage and the oxygen pressure oscillation was approximated by the use of the model equations. Operated with air, the cell voltage oscillation is increasingly amplified towards higher frequencies, which is accompanied by a continuous increase of the phase shift between the pressure excitation and the voltage response. Further analysis showed that the similar amplification of the partial pressure oscillation of oxygen is caused by an amplification of the inlet flow rate oscillation towards higher frequencies. The oscillation of the inlet flow rate was observed to arise from the pressure changes in the gas reservoir of the humidifier, which is in accordance with previous studies [17]. Therefore, the observed frequency dependence of the cell voltage oscillation could be finally traced back to the oscillation of the inlet flow rate.

This finding enabled the possibility to interpret the experimentally observed influence of operational and structural parameters on the EPIS results in the second part of the EPIS study. The observed enlargement of the maximum amplitude of the cell voltage oscillation by decreasing the oxygen stoichiometry could be attributed to the stronger influence of the oscillating inlet flow rate on the cell voltage oscillation. The purely simulative study of the variation of the gas volume of the humidifier showed the dominating influence of this parameter on the EPIS results.

The variation of the gas feed composition led to a qualitative change of the spectra of the transfer function between the cell voltage response and the pressure excitation, in case of the experiments [17]. Towards higher oxygen contents, the influence of the oscillating inlet flow rate on the cell voltage oscillation seems to be faded and the cell voltage response is rather following the average total pressure oscillation along the channel. In the context of the corresponding simulation, a notable finding was the change of the relationship between the cell voltage oscillation and the oxygen pressure oscillation with the oxygen concentration in the CL. This dependence might enable the indirect measurement of the oxygen concentration in the CL, which would allow the detection of reactant starvation due to limited diffusion. To achieve this, one needs to derive a model (cf. Chapter 5.1.2.3) which allows the prediction of the oxygen pressure oscillation in the CL based on the known outlet pressure excitation. Next, the cell voltage oscillation needs to be measured in a frequency range in which it is dominated by the oxygen pressure oscillation. The analysis of the amplitude ratio between the cell voltage and oxygen pressure oscillation could then allow the approximation of the oxygen pressure or concentration in the CL.

The aim of the third part of the EPIS study was to expose the direct influence of time-dependent processes on the spectra separately. This was achieved by simulating different model configurations in which only the process of interest was switched on. The DL charge and discharge became visible in the frequency range above 1 Hz and led to a decrease of the amplitude of the cell voltage oscillation towards zero. The water uptake of the PEM was visible below 0.1 Hz and led to an increase of the amplitude of the cell voltage

oscillations, due to the change in proton conductivity. The gas transport through the GDL was only visible above 100 Hz, which is beyond the experimentally analyzed frequency range [14–22,28,81]. The frequency range indicates that the feature is not related to the phenomenon of diffusion. Without consideration of the gas volume of the humidifier, the gas transport through the gas channel led to a reduction of the amplitude of the cell voltage oscillation above 1 Hz. The gas channel transport with consideration of the humidifier showed that the EPIS signal of the full model setup is dominated by this process, which makes the direct measurement of other processes difficult.

A possible next step resulting from the present study would be the analysis of the relationship between the cell voltage oscillation and the oxygen pressure oscillation, with the focus on their maximum amplitudes. To finally prove the dominating influence of the humidifier on EPIS, an experiment with a gas mixture containing already humidified air could be conducted with bypassing the humidifier. Another useful experiment could be the recording of another polarization curve with an increased gauge pressure. The static pressure-voltage response could help to further parametrize the PEMFC model. In terms of the modeling approach, further steps could be the integration of liquid water, which may enable the reproduction of EPIS at high current densities. Additionally, the simulation of the related methodology CFRA could be performed to investigate the origin of its features.

To conclude, a model-based analysis was used for the first time to study the characterization method EPIS applied to a PEMFC. By extending the state-of-the-art in PEMFC modeling the EPIS experiments could be reproduced successfully. The interpretation of the results increased the understanding of EPIS significantly and revealed a promising correlation which needs to be further investigated.

References

1. “Framing and Context,” in *Global Warming of 1.5°C*, IPCC, ed. (Cambridge University Press, 2022), pp. 49–92.
2. United Nations / Framework Convention on Climate Change, *Adoption of the Paris Agreement*. 21st Conference of the Parties, Paris: United Nations, 2015.
3. “Mitigation Pathways Compatible with 1.5°C in the Context of Sustainable Development,” in *Global Warming of 1.5°C*, IPCC, ed. (Cambridge University Press, 2022), pp. 93–174.
4. E4tech, “The Fuel Cell Industry Review 2020.” 24.06.2021, https://fuelcellindustryreview.com/.
5. J. Larminie and A. Dicks, *Fuel cell systems explained*, 2nd ed (J. Wiley, 2003).
6. A. Sorrentino, K. Sundmacher, and T. Vidakovic-Koch, “Polymer Electrolyte Fuel Cell Degradation Mechanisms and Their Diagnosis by Frequency Response Analysis Methods: A Review,” Energies **13**, 5825 (2020).
7. S. M. Rezaei Niya and M. Hoorfar, “Study of proton exchange membrane fuel cells using electrochemical impedance spectroscopy technique – A review,” J. Power Sources **240**, 281–293 (2013).
8. T. E. Springer, T. A. Zawodzinski, M. S. Wilson, and S. Gottesfeld, “Characterization of Polymer Electrolyte Fuel Cells Using AC Impedance Spectroscopy,” J. Electrochem. Soc. **143**, 587–599 (1996).
9. J. Zhang, Y. Tang, C. Song, and J. Zhang, “Polybenzimidazole-membrane-based PEM fuel cell in the temperature range of 120–200°C,” J. Power Sources **172**, 163–171 (2007).
10. N. H. Jalani, M. Ramani, K. Ohlsson, S. Buelte, G. Pacifico, R. Pollard, R. Staudt, and R. Datta, “Performance analysis and impedance spectral signatures of high temperature PBI–phosphoric acid gel membrane fuel cells,” J. Power Sources **160**, 1096–1103 (2006).
11. S. Cruz-Manzo and R. Chen, “Electrochemical impedance study on estimating the mass transport resistance in the polymer electrolyte fuel cell cathode catalyst layer,” J. Electroanal. Chem. **702**, 45–48 (2013).
12. X. Yuan, H. Wang, J. Colin Sun, and J. Zhang, “AC impedance technique in PEM fuel cell diagnosis—A review,” Int. J. Hydrogen Energy **32**, 4365–4380 (2007).
13. S. J. Andreasen, J. R. Vang, and S. K. Kær, “High temperature PEM fuel cell performance characterisation with CO and CO_2 using electrochemical impedance spectroscopy,” Int. J. Hydrogen Energy **36**, 9815–9830 (2011).
14. A. V. Shirsath, S. Raël, C. Bonnet, L. Schiffer, W. G. Bessler, and F. Lapicque, “Electrochemical pressure impedance spectroscopy for investigation of mass transfer in polymer electrolyte membrane fuel cells,” Curr. Opin. Electrochem. **20**, 82–87 (2020).

15. A. V. Shirsath, C. Bonnet, D. Arora, S. Raël, and F. Lapicque, “Characterization of water transport and flooding conditions in polymer electrolyte membrane fuel cells by electrochemical pressure impedance spectroscopy (EPIS),” Int. J. Heat Mass Transf. **190**, 122767 (2022).
16. A. V. Shirsath, C. Bonnet, S. Raël, and F. Lapicque, “Analysis of gas transport phenomena in a polymer electrolyte fuel cell by electrochemical pressure impedance spectroscopy,” J. Power Sources **531**, 231341 (2022).
17. A. V. Shirsath, S. Raël, C. Bonnet, and F. Lapicque, “Electrochemical pressure impedance spectroscopy applied to polymer electrolyte membrane fuel cells for investigation of transport phenomena,” Electrochim. Acta **363**, 137157 (2020).
18. Q. Zhang, H. Homayouni, B. D. Gates, M. H. Eikerling, and A. M. Niroumand, “Electrochemical Pressure Impedance Spectroscopy for Polymer Electrolyte Fuel Cells via Back-Pressure Control,” J. Electrochem. Soc. **169**, 44510 (2022).
19. E. Engebretsen, T. J. Mason, P. R. Shearing, G. Hinds, and D. J. L. Brett, “Electrochemical pressure impedance spectroscopy applied to the study of polymer electrolyte fuel cells,” Electrochem. Commun. **75**, 60–63 (2017).
20. A. Sorrentino, T. Vidakovic-Koch, and K. Sundmacher, “Studying mass transport dynamics in polymer electrolyte membrane fuel cells using concentration-alternating frequency response analysis,” J. Power Sources **412**, 331–335 (2019).
21. A. Sorrentino, K. Sundmacher, and T. Vidakovic-Koch, “Decoupling oxygen and water transport dynamics in polymer electrolyte membrane fuel cells through frequency response methods based on partial pressure perturbations,” Electrochim. Acta **390**, 138788 (2021).
22. A. Sorrentino, T. Vidakovic-Koch, R. Hanke-Rauschenbach, and K. Sundmacher, “Concentration-alternating frequency response: A new method for studying polymer electrolyte membrane fuel cell dynamics,” Electrochim. Acta **243**, 53–64 (2017).
23. M. Eschenbach, R. Coulon, A. A. Franco, J. Kallo, and W. G. Bessler, “Multi-scale modelling of fuel cells: From the cell to the system,” Solid State Ion. **192**, 615–618 (2011).
24. J. P. Neidhardt, D. N. Fronczek, T. Jahnke, T. Danner, B. Horstmann, and W. G. Bessler, “A Flexible Framework for Modeling Multiple Solid, Liquid and Gaseous Phases in Batteries and Fuel Cells,” J. Electrochem. Soc. **159**, A1528-A1542 (2012).
25. V. Gurau, H. Liu, and S. Kakaç, “Two-dimensional model for proton exchange membrane fuel cells,” AIChE J. **44**, 2410–2422 (1998).
26. A. Z. Weber and J. Newman, “Transport in Polymer-Electrolyte Membranes,” J. Electrochem. Soc. **151**, A326 (2004).
27. C. Bao and W. G. Bessler, “Two-Dimensional Modeling of a Polymer Electrolyte Membrane Fuel Cell with Long Flow Channel. Part I. Model development,” J. Power Sources **275**, 922–934 (2015).

28. L. Schiffer, A. V. Shirsath, S. Raël, C. Bonnet, F. Lapicque, and W. G. Bessler, "Electrochemical Pressure Impedance Spectroscopy for Polymer Electrolyte Membrane Fuel Cells: A Combined Modeling and Experimental Analysis," J. Electrochem. Soc. **169**, 34503 (2022).
29. C. Gabrielli and B. Tribollet, "A Transfer Function Approach for a Generalized Electrochemical Impedance Spectroscopy," J. Electrochem. Soc. **141**, 1147–1157 (1994).
30. A. M. Niroumand, W. Mérida, M. Eikerling, and M. Saif, "Pressure–voltage oscillations as a diagnostic tool for PEFC cathodes," Electrochem. Commun. **12**, 122–124 (2010).
31. D. Grübl, J. Janek, and W. G. Bessler, "Electrochemical Pressure Impedance Spectroscopy (EPIS) as Diagnostic Method for Electrochemical Cells with Gaseous Reactants: A Model-Based Analysis," J. Electrochem. Soc. **163**, A599-A610 (2016).
32. P. Hartmann, D. Grübl, H. Sommer, J. Janek, W. G. Bessler, and P. Adelhelm, "Pressure Dynamics in Metal–Oxygen (Metal–Air) Batteries: A Case Study on Sodium Superoxide Cells," J. Phys. Chem. C **118**, 1461–1471 (2014).
33. A. Z. Weber, R. L. Borup, R. M. Darling, P. K. Das, T. J. Dursch, W. Gu, D. Harvey, A. Kusoglu, S. Litster, M. M. Mench, R. Mukundan, J. P. Owejan, J. G. Pharoah, M. Secanell, and I. V. Zenyuk, "A Critical Review of Modeling Transport Phenomena in Polymer-Electrolyte Fuel Cells," J. Electrochem. Soc. **161**, F1254–F1299 (2014).
34. A. Z. Weber and J. Newman, "Modeling Transport in Polymer-Electrolyte Fuel Cells," Chem. Rev. **104**, 4679–4726 (2004).
35. M. A. Khan, B. Sundén, and J. Yuan, "Analysis of multi-phase transport phenomena with catalyst reactions in polymer electrolyte membrane fuel cells – A review," J. Power Sources **196**, 7899–7916 (2011).
36. G. Zhang and K. Jiao, "Multi-phase models for water and thermal management of proton exchange membrane fuel cell: A review," J. Power Sources **391**, 120–133 (2018).
37. K. C. Neyerlin, W. Gu, J. Jorne, and H. A. Gasteiger, "Determination of Catalyst Unique Parameters for the Oxygen Reduction Reaction in a PEMFC," J. Electrochem. Soc. **153**, A1955 (2006).
38. K. C. Neyerlin, W. Gu, J. Jorne, and H. A. Gasteiger, "Study of the Exchange Current Density for the Hydrogen Oxidation and Evolution Reactions," J. Mol. Catal. A Chem. **154**, B631 (2007).
39. J. Durst, C. Simon, F. Hasché, and H. A. Gasteiger, "Hydrogen Oxidation and Evolution Reaction Kinetics on Carbon Supported Pt, Ir, Rh, and Pd Electrocatalysts in Acidic Media," J. Electrochem. Soc. **162**, F190-F203 (2015).
40. A. Parthasarathy, S. Srinivasan, A. J. Appleby, and C. R. Martin, "Pressure Dependence of the Oxygen Reduction Reaction at the Platinum Microelectrode/Nafion Interface: Electrode Kinetics and Mass Transport," J. Electrochem. Soc. **139**, 2856–2862 (1992).

41. A. Parthasarathy, S. Srinivasan, A. J. Appleby, and C. R. Martin, “Temperature Dependence of the Electrode Kinetics of Oxygen Reduction at the Platinum/Nafion® Interface—A Microelectrode Investigation,” J. Electrochem. Soc. **139**, 2530–2537 (1992).
42. J. C. Amphlett, R. M. Baumert, R. F. Mann, B. A. Peppley, P. R. Roberge, and T. J. Harris, “Performance Modeling of the Ballard Mark IV Solid Polymer Electrolyte Fuel Cell: II . Empirical Model Development,” J. Electrochem. Soc. **142**, 9–15 (1995).
43. D.R. Sena, E.A. Ticianelli, V.A. Paganin, and E.R. Gonzalez, “Effect of water transport in a PEFC at low temperatures operating with dry hydrogen,” J. Electroanal. Chem. **477**, 164–170 (1999).
44. S. J. Lee, S. Mukerjee, J. McBreen, Y. W. Rho, Y. T. Kho, and T. H. Lee, “Effects of Nafion impregnation on performances of PEMFC electrodes,” Electrochim. Acta **43**, 3693–3701 (1998).
45. T. E. Springer, T. A. Zawodzinski, and S. Gottesfeld, “Polymer Electrolyte Fuel Cell Model,” J. Electrochem. Soc. **138**, 2334 (1991).
46. D. M. Bernardi and M. W. Verbrugge, “A Mathematical Model of the Solid-Polymer-Electrolyte Fuel Cell,” J. Electrochem. Soc. **139**, 2477–2491 (1992).
47. T. E. Springer, M. S. Wilson, and S. Gottesfeld, “Modeling and Experimental Diagnostics in Polymer Electrolyte Fuel Cells,” J. Electrochem. Soc. **140**, 3513–3526 (1993).
48. T. E. Springer, T. Rockward, T. A. Zawodzinski, and S. Gottesfeld, “Model for Polymer Electrolyte Fuel Cell Operation on Reformate Feed: Effects of CO, H2 Dilution, and High Fuel Utilization,” J. Vac. Sci. Technol. A **148**, A11 (2001).
49. J. J. Baschuk and X. Li, “Modelling CO poisoning and O2 bleeding in a PEM fuel cell anode,” Int. J. Energy Res. **27**, 1095–1116 (2003).
50. J.J. Baschuk and X. Li, “Modelling of polymer electrolyte membrane fuel cells with variable degrees of water flooding,” J. Power Sources **86**, 181–196 (2000).
51. J. J. Baschuk, A. M. Rowe, and X. Li, “Modeling and Simulation of PEM Fuel Cells With CO Poisoning,” J. Energy Resour. Technol. **125**, 94–100 (2003).
52. S. H. Chan, S. K. Goh, and S. P. Jiang, “A mathematical model of polymer electrolyte fuel cell with anode CO kinetics,” Electrochim. Acta **48**, 1905–1919 (2003).
53. C. Marr and X. Li, “Composition and performance modelling of catalyst layer in a proton exchange membrane fuel cell,” J. Power Sources **77**, 17–27 (1999).
54. A. Rowe and X. Li, “Mathematical modeling of proton exchange membrane fuel cells,” J. Power Sources **102**, 82–96 (2001).
55. R. Vetter and J. O. Schumacher, “Free open reference implementation of a two-phase PEM fuel cell model,” Comput. Phys. Commun. **234**, 223–234 (2019).
56. K. T. Jeng, S. F. Lee, G. F. Tsai, and C. H. Wang, “Oxygen mass transfer in PEM fuel cell gas diffusion layers,” J. Power Sources **138**, 41–50 (2004).

57. A. C. West and T. F. Fuller, “Influence of rib spacing in proton-exchange membrane electrode assemblies,” J. Appl. Electrochem. **26**, 557–565 (1996).
58. J. Kleemann, F. Finsterwalder, and W. Tillmetz, “Characterisation of mechanical behaviour and coupled electrical properties of polymer electrolyte membrane fuel cell gas diffusion layers,” J. Power Sources **190**, 92–102 (2009).
59. S. Chevalier, D. Trichet, B. Auvity, J. C. Olivier, C. Josset, and M. Machmoum, “Multiphysics DC and AC models of a PEMFC for the detection of degraded cell parameters,” Int. J. Hydrogen. Energy **38**, 11609–11618 (2013).
60. G. A. Futter, P. Gazdzicki, K. A. Friedrich, A. Latz, and T. Jahnke, “Physical modeling of polymer-electrolyte membrane fuel cells: Understanding water management and impedance spectra,” J. Power Sources **391**, 148–161 (2018).
61. M. Mayur, S. Strahl, A. Husar, and W. G. Bessler, “A Multi-Timescale Modeling Methodology for PEMFC Performance and Durability in a Virtual Fuel Cell Car,” Int. J. Hydrogen Energy **40**, 16466–16476 (2015).
62. J. H. Ohs, U. Sauter, S. Maass, and D. Stolten, “Modeling hydrogen starvation conditions in proton-exchange membrane fuel cells,” J. Power Sources **196**, 255–263 (2011).
63. N. P. Siegel, M. W. Ellis, D. J. Nelson, and M. R. von Spakovsky, “Single domain PEMFC model based on agglomerate catalyst geometry,” J. Power Sources **115**, 81–89 (2003).
64. R. M. Rao, D. Bhattacharyya, R. Rengaswamy, and S. R. Choudhury, “A two-dimensional steady state model including the effect of liquid water for a PEM fuel cell cathode,” J. Power Sources **173**, 375–393 (2007).
65. K. P. Adzakpa, K. Agbossou, Y. Dube, M. Dostie, M. Fournier, and A. Poulin, “PEM Fuel Cells Modeling and Analysis Through Current and Voltage Transient Behaviors,” IEEE Trans. Energy Convers. **23**, 581–591 (2008).
66. I. Tolj, D. Bezmalinovic, and F. Barbir, “Maintaining desired level of relative humidity throughout a fuel cell with spatially variable heat removal rates,” Int. J. Hydrogen. Energy **36**, 13105–13113 (2011).
67. T. F. Fuller and J. Newman, “Water and Thermal Management in Solid-Polymer-Electrolyte Fuel Cells,” J. Electrochem. Soc. **140**, 1218–1225 (1993).
68. V. P. Schulz, J. Becker, A. Wiegmann, P. P. Mukherjee, and C.-Y. Wang, “Modeling of Two-Phase Behavior in the Gas Diffusion Medium of PEFCs via Full Morphology Approach,” J. Electrochem. Soc. **154**, B419 (2007).
69. G. Zhang and K. Jiao, “Three-dimensional multi-phase simulation of PEMFC at high current density utilizing Eulerian-Eulerian model and two-fluid model,” Energy Convers. Manag. **176**, 409–421 (2018).
70. H. Wu, X. Li, and P. Berg, “On the modeling of water transport in polymer electrolyte membrane fuel cells,” Electrochim. Acta **54**, 6913–6927 (2009).

71. G. Zhang, L. Fan, J. Sun, and K. Jiao, "A 3D model of PEMFC considering detailed multi-phase flow and anisotropic transport properties," Int. J. Heat Mass Transf. **115**, 714–724 (2017).
72. E. Hontañón, M. J. Escudero, C. Bautista, P. L. García-Ybarra, and L. Daza, "Optimisation of flow-field in polymer electrolyte membrane fuel cells using computational fluid dynamics techniques," J. Power Sources **86**, 363–368 (2000).
73. H. Heidary, M. J. Kermani, and B. Dabir, "Influences of bipolar plate channel blockages on PEM fuel cell performances," Energy Convers. Manag. **124**, 51–60 (2016).
74. S. Gößling, N. Nickig, and M. Bahr, "2-D + 1-D PEM fuel cell model for fuel cell system simulations," Int. J. Hydrogen. Energy **46**, 34874–34882 (2021).
75. J. Liang, Y. Li, R. Wang, and J. Jiang, "Cross-dimensional model of the oxygen transport behavior in low-Pt proton exchange membrane fuel cells," Chem. Eng. J. **400**, 125796 (2020).
76. L. M. Pant, M. R. Gerhardt, N. Macauley, R. Mukundan, R. L. Borup, and A. Z. Weber, "Along-the-channel modeling and analysis of PEFCs at low stoichiometry: Development of a 1+2D model," Electrochim. Acta **326**, 134963 (2019).
77. W. G. Bessler, S. Gewies, and M. Vogler, "A New Framework for Physically Based Modeling of Solid Oxide Fuel Cells," Electrochim. Acta **53**, 1782–1800 (2007).
78. R. B. Bird, W. E. Stewart, and E. N. Lightfoot, *Transport phenomena*, Rev. 2. ed. (John Wiley & Sons, 2007), p. 80, 148, 537, 538, 583, 794.
79. S. Ge, X. Li, B. Yi, and I.-M. Hsing, "Absorption, Desorption, and Transport of Water in Polymer Electrolyte Membranes for Fuel Cells," J. Electrochem. Soc. **152**, A1149 (2005).
80. H. Wu, *Mathematical Modeling of Transient Transport Phenomena in PEM Fuel Cells*, PhD Thesis, University of Waterloo, 2009.
81. A. V. Shirsath, *Mise au point expérimentale de la spectroscopie d'impédance électrochimique par modulation de pression pour la caractérisation des phénomènes de transport dans une pile à combustible à membrane*, Thèse de Doctorat, Université de Lorraine, 2021.
82. Malcolm W. Chase, JR., *NIST-JANAF thermochemical tables*, 4th Ed. (American Institute of Physics, 1998).
83. M. J. Lampinen and Marina Fomino, "Analysis of Free Energy and Entropy Changes for Half-Cell Reactions," J. Electrochem. Soc. **140**, 3537 (1993).
84. J. Dujc, A. Forner-Cuenca, P. Marmet, M. Cochet, R. Vetter, J. O. Schumacher, and P. Boillat, "Modeling the Effects of Using Gas Diffusion Layers With Patterned Wettability for Advanced Water Management in Proton Exchange Membrane Fuel Cells," J. Electrochem. Energy Convers. Storage **15** (2018).

85. E. N. Fuller, P. D. Schettler, and J. C. Giddings, “New Method for Prediction of Binary Gas-Phase Diffusion Coefficients,” Ind. Eng. Chem. **58**, 18–27 (1966).
86. H. Zhu, R. J. Kee, V. M. Janardhanan, O. Deutschmann, and D. G. Goodwin, “Modeling elementary heterogeneous chemistry and electrochemistry in solid-oxide fuel cells,” J. Electrochem. Soc. **152**, A2427-A2440 (2005).
87. S. Motupally, A. J. Becker, and J. W. Weidner, “Diffusion of Water in Nafion 115 Membranes,” J. Electrochem. Soc. **147**, 3171 (2000).
88. T. A. Zawodzinski, M. Neeman, L. O. Sillerud, and S. Gottesfeld, “Determination of water diffusion coefficients in perfluorosulfonate ionomeric membranes,” J. Phys. Chem. **95**, 6040–6044 (1991).
89. S. C. Yeo and A. Eisenberg, “Physical properties and supermolecular structure of perfluorinated ion-containing (nafion) polymers,” J. Appl. Polym. Sci. **21**, 875–898 (1977).
90. A. L. Buck, “New Equations for Computing Vapor Pressure and Enhancement Factor,” J. Appl. Meteor. **20**, 1527–1532 (1981).
91. R. Ehrig, U. Nowak, L. Oeverdieck, and P. Deuflhard, “Advanced Extrapolation Methods for Large Scale Differential Algebraic Problems,” in *High performance scientific and engineering computing. Lecture notes in computational science and engineering*, Vol. 8, H.-J. Bungartz, F. Durst, and C. Zenger, eds. (Springer, 1999), pp. 233–244.
92. P. Deuflhard, E. Hairer, and J. Zugck, “One-step and extrapolation methods for differential-algebraic systems,” Numer. Math. **51**, 501–516 (1987).
93. A. Lasia, *Electrochemical Impedance Spectroscopy and its Applications* (Springer New York, 2014).
94. W. G. Bessler, “Rapid Impedance Modeling via Potential Step and Current Relaxation Simulations,” J. Electrochem. Soc. **154**, B1186-B1191 (2007).
95. U. Bossel, “Open circuit voltage mystery solved for proton-conducting fuel cells?,” Int. J. Hydrogen. Energy **47**, 9372–9381 (2022).
96. S. A. Vilekar and R. Datta, “The effect of hydrogen crossover on open-circuit voltage in polymer electrolyte membrane fuel cells,” J. Power Sources **195**, 2241–2247 (2010).
97. F. Liu, B. Yi, D. Xing, J. Yu, Z. Hou, and Y. Fu, “Development of novel self-humidifying composite membranes for fuel cells,” J. Power Sources **124**, 81–89 (2003).
98. Z. Xie and S. Holdcroft, “Polarization-dependent mass transport parameters for orr in perfluorosulfonic acid ionomer membranes: an EIS study using microelectrodes,” J. Electroanal. Chem. **568**, 247–260 (2004).
99. Z. Tang, Q.-A. Huang, Y.-J. Wang, F. Zhang, W. Li, A. Li, L. Zhang, and J. Zhang, “Recent progress in the use of electrochemical impedance spectroscopy for the measurement, monitoring, diagnosis and optimization of proton exchange membrane fuel cell performance,” J. Power Sources **468**, 228361 (2020).

100. Y. Bultel, K. Wiezell, F. Jaouen, P. Ozil, and G. Lindbergh, “Investigation of mass transport in gas diffusion layer at the air cathode of a PEMFC,” Electrochim. Acta **51**, 474–488 (2005).
101. I. A. Schneider, S. A. Freunberger, D. Kramer, A. Wokaun, and G. G. Scherer, “Oscillations in Gas Channels,” J. Electrochem. Soc. **154**, B383 (2007).
102. I. A. Schneider, D. Kramer, A. Wokaun, and G. G. Scherer, “Oscillations in Gas Channels,” Electrochem. Commun. **154**, B770 (2007).
103. R. Makharia, M. F. Mathias, and D. R. Baker, “Measurement of Catalyst Layer Electrolyte Resistance in PEFCs Using Electrochemical Impedance Spectroscopy,” J. Electrochem. Soc. **152**, A970 (2005).
104. M. Mathias, D. Baker, J. Zhang, Y. Liu, and W. Gu, “Frontiers in Application of Impedance Diagnostics to H2-Fed Polymer Electrolyte Fuel Cells,” ECS Trans. **13**, 129–152 (2008).
105. M. Chandesris, C. Robin, M. Gerard, and Y. Bultel, “Investigation of the difference between the low frequency limit of the impedance spectrum and the slope of the polarization curve,” Electrochim. Acta **180**, 581–590 (2015).
106. G. Maranzana, J. Mainka, O. Lottin, J. Dillet, A. Lamibrac, A. Thomas, and S. Didierjean, “A proton exchange membrane fuel cell impedance model taking into account convection along the air channel: On the bias between the low frequency limit of the impedance and the slope of the polarization curve,” Electrochim. Acta **83**, 13–27 (2012).
107. J. Zhang, C. Song, J. Zhang, R. Baker, and L. Zhang, “Understanding the effects of backpressure on PEM fuel cell reactions and performance,” J. Electroanal. Chem. **688**, 130–136 (2013).
108. J. Zhang, H. Li, and J. Zhang, “Effect of Operating Backpressure on PEM Fuel Cell Performance,” ECS Trans. **19**, 65–76 (2009).
109. L. Schiffer and W. G. Bessler, “Electrochemical Pressure Impedance Spectroscopy for Polymer Electrolyte Membrane Fuel Cells: Signal Interpretation,” J. Electrochem. Soc; Submitted on 27 January 2023.
110. C. Ziegler, T. Heilmann, and D. Gerteisen, “Experimental Study of Two-Phase Transients in PEMFCs,” Electrochem. Commun. **155**, B349 (2008).

Acknowledgements

At the end of this dissertation I would like to acknowledge the generous help and support I received which gave me the possibility to produce the present work in the context of a German-French research collaboration at the Offenburg University of Applied Sciences.
I especially want to thank Prof. Dr. Wolfgang G. Bessler for recruiting me into his working group and supervising my doctoral studies;
Prof. Dr. Francois Lapicque for reviewing this work and his working group, including Prof. Stéphane Raël, Dr. Caroline Bonnet and Dr. Anantrao V. Shirsath, for providing the experimental data I could use in my work.
All the aforementioned were part of the French-German partner project in which the present work was prepared. In this context I want to acknowledge the funding of the German share of the partner project from the German Research Foundation (Deutsche Forschungsgemeinschaft, DFG) and my former colleague Daniel Grübl for his preliminary EPIS work.
Finally, I want to thank Simone Schede and Björn Weißhar for their proofreading of this dissertation.